Development of Ultra Low Pt Electrochemical Catalysts of Oxygen Reduction Reaction for Fuel Cells

燃料電池用酸素還元反応の白金触媒量低減化に関する研究

Graduate School of Life Science
and System Engineering
Kyushu Institute of Technology

Dissertation for the Degree of Doctor of Engineering

Nannan Wang
August 2018

Supervisor
Professor Tingli Ma

Abstract

Polymer electrolyte membrane fuel cell (PEMFC) is recognized as one of the most effective, environmental-friendly, and futuristic technologies for clean energy. However, the low conversion efficiency of the oxygen reduction reaction (ORR) catalysts hindered its further practical application. Because a commercial and efficient ORR catalyst, Pt nanoparticles loaded on the carbon (XC-72) cannot meet the demand for widespread application due to its excessive cost, poor durability, and fast poisoning during the reaction. Identifying plausible solutions to these problems is still a challenge. In this thesis, we focused on the development of the novel efficient catalysts for ORR with ultra-low Pt loading amount and Pt-free materials. In order to further improve catalytic activity, we also synthesized a new 2-D material Nb_2C to replace the carbon support of the catalyst.

In chapter 1, the fundamental theory and the structure of fuel cells were briefly described. The theoretical analyses of the ORR process were also introduced. Furthermore, the recent development of the ORR catalysts was summarized. Finally, we exhibited the issues of ORR catalysts and the purposes in this thesis.

In chapter 2, the reagents and instruments used in this work were summarized. We also introduced the preparation methods of the working electrode and the characterizations. Finally, the electrochemical measurements and analyses, such as the cyclic voltammetry (CV) and the linear sweep voltammetry (LSV) were presented.

In chapter 3, the synthesis procedure for PtM (M: Fe, Co, Ni) alloy samples through a simple method under the mild conditions was described. In detail, the transition metals were doped into the Pt nanoplate crystals to form PtM (M: Fe, Co, Ni) alloys. The physical characterizations proved that the PtFe alloy has a well-defined, homogeneous, and ultra-small particle size morphology. We found that the morphology contributes the higher catalytic activity. Finally, the PtM (M: Fe, Co, Ni) alloys are used as the ORR catalyst, and they show the excellent catalytic activity and stability both in the acidic and alkaline medium.

In chapter 4, 3 kinds of Pt-free catalysts were successfully designed and synthesized. A metal-organic framework (MOF) was used as a precursor. The influences of the carbonization temperature and the ratios of the two transition metals were studied in terms of the ORR performance. Meanwhile, the synergistic effect of the dual transition metals was

considered to have a positive impact on improving the electrocatalytic activity. The electrochemistry analyses displayed that FCPA-900 shows the best ORR catalytic activities, because of the larger specific surface area and the better-defined amorphous carbon structure.

In chapter 5, firstly, in order to obtain a 2-D MAX Nb_2AlC under a mild condition, we studied on the influence of target materials under the different conditions, such as reaction method, type of molten salts flux, reaction temperature, and reaction time. The synthesis temperature of the MAX Nb_2AlC was successfully decreased from 1600°C to 1000°C by using the molten salt assisted solid-state reaction. The reaction mechanism of the Nb_2AlC was also investigated, and the effect of the NaCl flux on Nb_2AlC synthesis was confirmed. Secondly, the multilayer 2-D MXene Nb_2C material was obtained by etching the MAX Nb_2AlC. Finally, the ORR catalytic activity of the Pt nanoparticles loaded on the multilayer 2-D MXene Nb_2C was studied. The results of the electrochemical measurements show that the 2-D MXene Nb_2C is an excellent support material to replace carbon for the Pt loading catalyst.

In chapter 6, the general conclusions and prospects were presented. The electrochemical performance of the obtained Pt-based and Pt-free catalysts for the ORR was summarized. Further studies need to focus on improving the stability, promoting the efficiency, and developing new high-performance ORR catalysts.

Contents

Chapter 1 Background

1.1 Introduction

It is a key problem to balance the relationship of the environment protection and energy crisis in the future decades with the development of society. The fossil fuels such as coal and oil are low efficiency and highly polluted. All the fossil fuel transfer to useful work need to obey the Carnot Cycle, which is only 15-40 % energy conversion efficiency. At the same time, extensive use of fossil fuels would generate much greenhouse gas harmful or toxic to the environment, such as CO_2 and poison NO_x gas. Therefore, searching for a new energy resource becomes the development strategy for every country. Fuel cell is a device of renewable clean energy, due to that H_2O is the only product. In addition, the energy conversion efficiency of the fuel cell device is up to 60-80% without through the Carnot-cycle. Therefore, there is no doubt that fuel cell is recognized as the most effective and environmental technology in the world.

The diverse types of fuel cells are summarized in Table 1.1 [1-2]. Based on the working temperature, there are three kinds of fuel cells: high temperature, intermediate temperature, and low-temperature fuel cells. Molten carbonate fuel cells (MCFCs), solid oxide fuel cells (SOFCs) are the high-temperature fuel cells, used for large-scale power generation. Phosphate fuel cells (PAFCs) are the intermediate temperature fuel cells, used for large facilities or power plants. Proton exchange membrane fuel cells (PEMFCs), as known as polymer electrolyte fuel cells (PEFCs) or solid polymer electrolyte fuel cells (SPEFCs), and alkaline fuel cells (AFCs) belong to the low-temperature fuel cells, for which the working temperature is less than 100ºC. In some reports, AFCs are acted as the intermediate temperature fuel cells, since their working temperature is not stable. The exchange current density of AFCs is much lower than PEMFCs. Therefore, PEMFCs have more potential to commercialize, such as fuel cell bus.

PEMFCs acquire the advantages both of the fuel cells and themselves [3-5], such as low working temperature, high stability, and high-power generation efficiency. Due to these advantages and their potential application, PEMFCs are becoming the key point for every country to change the energy system.

Table 1.1 Introduction of different types of fuel cells

Type	Low temperature		Intermediate temperature	High temperature	
	PEMFCs	AFCs	PAFCs	SOFCs	MCFCs
Electrode or catalyst (anode)	Precious metal loading on carbon	Precious metal loading on carbon	Precious metal loading on carbon	Perovskite oxides or Ni-$ZrO_2(Y_2O_3)$ metal ceramic	Ni-Cr alloy or Ni-Al alloy
Fuel	H_2	H_2	H_2, CH_3OH, CH_4	H_2, CH_4	Hydrocarbons
Electrolyte	Proton exchange membrane	KOH solution	High concentration HPO_3	ZrO_2-Y_2O_3 membrane	Molten carbonate (Li_2CO_3-KCO_3)
Electrode or catalyst (cathode)	Precious metal loading on carbon	Precious metal loading on carbon	Precious metal loading on carbon	La (Sr, Ca) MnO_3	Porous NiO
Ions	H^+/H_3^+	OH^-	H^+	O^{2-}	CO_3^{2-}
Oxide	O_2/Air	O_2/Air	Air	Air	Air+CO_2
Working temperature	RT~80 °C	~100 °C	~200 °C	800~1000 °C	~650 °C
Power generation efficiency	~60%	~70%	36~45%	50~60%	45~60%
Limited of CO in fuel	<10 ppm	<10 ppm	<1%	OK	OK
Application	Automotive, Portable-equipment.	Cosmos, Military, Large ship.	Large CHP* systems (200 kW)	Vehicle auxiliary power, all sizes of CHP systems (2 kW to MW)	Medium to large scale CHP systems (up to MW)

*Combined Heat and Power

1.2 The history and development of PEMFCs

PEMFCs were introduced by Professor Grove in 1839, and developed by Professor L. Mond and C. Langer with the 3.5 mA cm^{-2} current density and the 0.73 V onset-potential. The great progress is acquired, such as the oxygen reduction reaction, Nafion membrane, sandwich structure of electrodes and remarkable efficiency. In 1993, a PEMFC's bus was brought into the market, which is zero pollution and high speed (75 km h^{-1}), promoting the application of the fuel cells. The market-oriented power station of the fuel cell was developed, such as the 250 kW power stations in Germany in 2000.

Anyway, Japan is the best country in the world to improve PEMFCs. In 1997, the first fuel cell civil vehicle FCHV-1 was discovered by Toyota in Japan. Then the first production version FCHV-4 came out in 2001. In 2015, the first hydrogen fuel cell vehicle in the world was official production. Then Honda, Ford also founded different serials fuel cells vehicle project, such as FCX, Hydrogen, and Freedom Car Project.

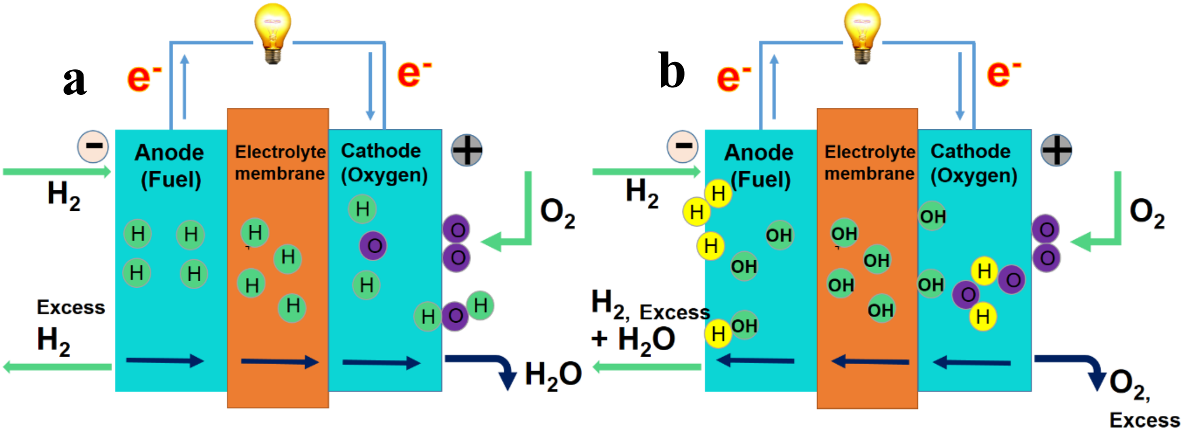

Figure 1.1 Structure illustration of a single PEFMC in acidic (a) and alkaline (b) media.

1.3 The structure and working mechanism of PEMFCs

Figure 1.1 shows the structure of PEMFCs with the different electrolytes. It is clear that there are three main parts: the anode where is oxide the fuel, the polymer membrane where let the protons go through but prevent the electrons moving, and the cathode where can reduce the oxygen. The catalyst is loading on the cathode or anode to promote the reaction [2, 6-9]. Figure1.1a is the mechanism schematic of PEMFCs in acid solution. In detail, H_2 decompose into two free protons H^+ and two electrons e^- with the help of anode catalyst. The active H^+ is formed from the free protons H^+ to react with the nearby H_2O, and then move to the cathode through the polymer membrane. In other words, the electrons are in the anode making a negative electrode. While, the active O_2 atoms absorb the electrons, which are from the anode through the external circuit, and the protons form H_2O with the help of the catalyst. The cathode becomes the positive electrode due to the accumulation of protons. Therefore, the protons transfer from the anode to the cathode through the internal circuit, and the electrons move from the negative electrode to positive electrode through the external circuit, forming a full circle current with the potential difference.

In general, the fuel cells would keep working forever with the adequate supply of H_2 and O_2. The reaction equation as follows:

Full reaction: $2H_2 + O_2 = 2H_2O \quad E^{\ominus} = 1.229\ V - 0\ V = 1.229\ V$

(*vs.* RHE at 100kPa, 298.15 K)

Anode: $2H_2 = 4H^+ + 4e^- \quad E^{\ominus} = 0\ V$

(*vs.* RHE at 100kPa, 298.15 K)

Cathode: $O_2 + 4H^+ + 4e^- = 2H_2O \quad E^{\ominus} = 1.229\ V$

(*vs.* RHE at 100kPa, 298.15 K)

Figure1.1 b shows another mechanism schematic of PEMFCs in alkaline solution. Similar to the PEMFCs in acid solution, the detailed mechanism shows in the following: the rich OH^- ions react with the fuel H_2 to become H_2O and electrons on the surface of the catalyst loaded on the anode. In addition, the electrons through external circle move to the cathode react with O_2. Under the effect of the catalyst loaded on the cathode, the O_2 transfer into OH^- to finish the whole reaction. The relevant reaction equation as follows:

Full reaction: $2H_2 + O_2 = 2H_2O \quad E^{\ominus} = 0.401\ V - (-0.828)\ V = 1.229\ V$

(*vs.* RHE at 100kPa, 298.15 K)

Anode: $2H_2 + 4OH^- = 4H_2O + 4e^- \quad E^{\ominus} = -0.828\ V$

(*vs.* RHE at 100kPa, 298.15 K)

Cathode: $O_2 + 2H_2O + 4e^- = 4OH^- \quad E^{\ominus} = 0.401\ V$

(*vs.* RHE at 100kPa, 298.15 K)

1.4 The ORR mechanism of PEMFCs

Most of the investigations are the cathode catalyst, because of that only about 0.05 mg $_{\text{Pt}}$ /cm^{-2} is enough in the anode. The anode reaction is called HOR, showing a high exchange current density (ECD) about J=1×10^{-2}~10^{2} mA cm^{-2}. Nevertheless, the cathode used to oxygen reduction reaction (ORR) shows a lower ECD about J=1×10^{-6}~10^{-7} mA cm^{-2} than that of the anode. In order to keep the reaction ongoing, the ORR needs to improve ECD by overcoming the high over-potential of the fuel cell.

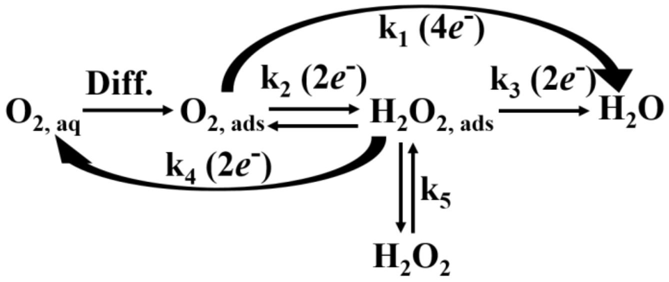

Figure 1.2 Two- or four-electrons pathway for oxygen reduction reaction in the acidic solution (aq means dissolved process in the water, ads means absorbed process by the active sites).

The route schematic [10, 11] of ORR in acidic and alkaline solution is shown in Figure 1.2 and 1.3. The different electrolytes or catalysts lead to the complicated ORR process, such as the different intermediate compounds, the pathways, the reaction process, and the reaction products. Herein, Pt/C catalyst is used as a representative to introduce the ORR mechanism.

Figure 1.2 shows the reaction processes in acidic solution [10]. The $O_{2,\,aq}$ is adsorbed by the active sites when O_2 is dissolved in water and diffused nearby the catalyst, forming $O_{2,\,ads}$. At this time, $O_{2,\,ads}$ has two ways to be reduced: the direct way or the four-electron pathway and the indirectly way or the two-electron pathway. The four-electron pathway can directly transfer O_2 into the H_2O (k_1 route in Figure 1.2), the full reaction equation is in the following.

Directly reaction: $O_2 + 4H^+ + 4e^- = 2H_2O \quad E^{\Theta}= 1.229\ V$

Step by step reaction: $O_2 + 2H^+ + 2e^- = H_2O_2 \quad E^{\Theta}= 0.695\ V$

$H_2O_2 + 2H^+ + 2e^- = 2H_2O \quad E^{\Theta}= 1.763\ V$

In the two-electron pathway, $O_{2,\ ads}$ is first reduced by two electrons forming the unstable intermediate product $H_2O_{2,\ ads}$ (k_2 route in Figure 1.2). Then the $H_2O_{2,\ ads}$ continuously obtains two electrons to generate H_2O along with the k_3 way. However, $H_2O_{2,\ ads}$ also can diffuse into the water (k_5 route), or decompose H_2O and $O_{2,\ ads}$ or $O_{2,\ aq}$ (k_4 route). The full reaction equation is in the following.

Directly reaction: $O_2 + 2H_2O + 4e^- = 4OH^-$ $E^{\Theta} = 0.401\ V$

Step by step reaction: $O_2 + H_2O + 2e^- = HO_2^- + OH^-$ $E^{\Theta} = -0.065\ V$

$HO_2^- + H_2O + 2e^- = 3OH^-$ $E^{\Theta} = 0.867\ V$

Now there is a critical problem coming out, that the high concentration of H_2O_2 erodes the proton exchange membrane. In addition, the H_2O_2 is sensitive for thermodynamic, the concentration of H_2O_2 is decided by the thermodynamic reaction not the kinetic process, suggesting that H_2O_2 is easy concentrating. That is the reason of the complicated reaction process.

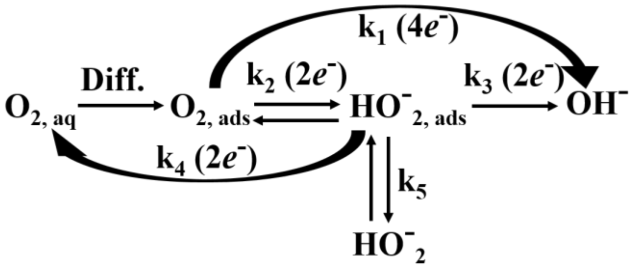

Figure 1.3 The two- or four-electrons pathway for ORR in the alkaline solution (aq means dissolved in the water, ads means absorbed by the active sites).

Similar to the reaction process of oxygen in the acid solution, Figure 1.3 is the ORR process in the alkaline solution. The adsorbed O_2 can transfer into OH^- through directly (k_1 route) path or two steps (k_2 and k_3 routes) path.

The unstable intermediate product HO_2^- have three paths to decompose: the k_3 route to finish the ORR, k_5 route to diffusion the electrolyte, and k_4 route to back to $O_{2,\ aq}$, suggesting that the two-electron pathway is lower energy transfer efficiency.

So according to the introduction, the intermediate product is a judgment criterion for the two-electron pathway or the four-electron pathway. In fact, we hope the ORR along with the highest efficiency four-electron pathway to increase the reduced current. However, there are too many influences to decide the reaction path, such as the structure of air electrode, the interaction ways between the oxygen and electrode, and the catalyst. Among them, the adsorbed way of the oxygen atoms is critical for the reaction paths. It is complicated to define the adsorbed way, because that the oxygen can be adsorbed as molecular or push into the crystalline of metal as atoms. Professor Yeager developed three adsorbed ways of oxygen in 1984: Griffiths, Pauling, and Bridge (Figure 1.4) [12].

(1) Griffiths: In detail, in the reaction, the bonds of oxygen are parallel to the surface of the catalyst. Two oxygen atoms each react with the one catalytic active site, leading to that the p orbit of oxygen reacts with the empty orbit of the catalytic active site each other. The decreasing or the stretching of the O-O bonds energy lead to the dissociated of the oxygen molecular, suggesting this is a high-energy reaction. Therefore, this way is beneficial to the four-electron pathway. The catalytic surface of the precious metal (Pt, Ru, Pd) and metal phthalocyanine show the Griffiths way, suggesting the high electrocatalytic activity.

(2) Pauling: One atom of oxygen molecules reacts with the active site, adsorbed by the surface of the catalyst. Only one atom adsorbs the energy, disadvantage for the broken of the O-O bonds. Most materials are proved to belong to the two-electron pathway.

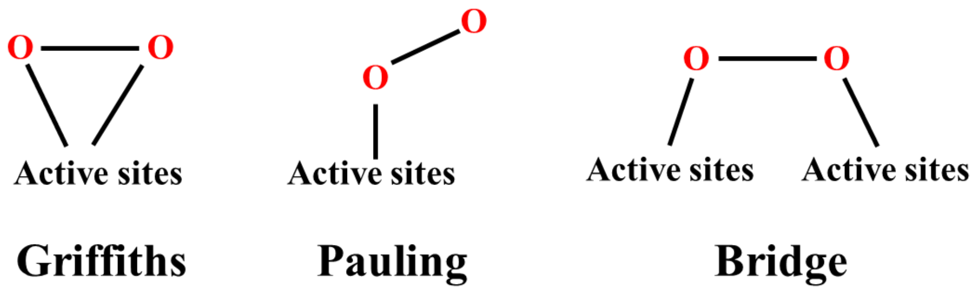

Figure 1.4 The adsorption ways of the O_2 on the surface of the catalyst.

3) Bridge: This behavior is similar to the Griffiths way, except for that the O-O bond is activation by two active sites. This way happens only when the distance of the O-O bond is similar to the two active sites, displaying the four-electron pathway due to the absorbed energy.

However, there is no consensus for the oxygen adsorbed pathways. Recently, Professor Norskov founded a new theory to explain ORR according to the d-band theory and thermodynamics, which is the two steps protonation: dissociative and associative [13].

The dissociative theory is that: the O-O bonds are broken by forming the free O^* atoms; then the O^* adsorb the proton and electron to produce the intermediate product HO^*; the HO^* react with the other proton and electron to finish ORR, the * means the active sites on the surface of the electrode. The detailed reaction equation is:

$$\frac{1}{2}O_2 + * \rightarrow O*$$

$$O* + H^+ + e^- \rightarrow HO*$$

$$HO* + H^+ + e^- \rightarrow H_2O + *$$

The associative theory is similar to the dissociative theory: the O_2 diffuses into the active sites to react with the proton and electron forming intermediate product HO_2*, then continue to adsorb another proton and electron to complete the reaction. The following is the reaction equation:

$$O_2 + * \rightarrow O_2*$$

$$O_2* + H^+ + e^- \rightarrow HO_2*$$

$$HO_2* + H^+ + e^- \rightarrow H_2O + O_2*$$

More information also obtained from the same group, such as that the density functional theory calculation shows that it equates to two dissociative and associative theories from the thermodynamic view. However, there is a controversy for which way is real in different groups, because they are lack of the powerful evidence. They analyzed the model of dissociative and associative molecular on the surface of the metal through the density functional theory, discovered that it is the linear relationship between the activation energy of the molecule dissociation and the binding energy of the atom on the metal surface. The Bronated-Evans-Polanyi (BEP) theory belonging to the linear free energy theory shows that the intermediate products are similar for molecule absorbed by the surface of the different metals, acted as a bridge of the thermodynamics and the kinetics.

Meanwhile, the onset-potential is up to 1.23 V when the ORR goes along with the four-electron pathway. However, the ORR is an irreversible reaction with the complicated products. For example, the over-potential is up to 0.2 V to maintain the reaction when Pt as the ORR catalyst. It needs to higher over-potential for other materials as the ORR catalyst with the more complicated products. In fact, about 80% loss of the whole fuel cell efficiency comes from ORR in the PEMFCs.

Therefore, it is urgent to develop free-precious metal ORR catalyst with the high activity, in order to improve the efficiency of PEMFCs, to promote the development of basic research, and to accelerate the practical application [14-17].

1.5 Recent advancements of catalyst for ORR

Searching for the high catalytic activity with low cost is the final target for researchers. After investigated for decades, scientist gradually confirmed the necessary properties for ORR catalyst, such as high catalytic activity, high stability, high conductivity, high surface area, resistance to oxidation and reduction, preservative, rich source, and cheap price. By now, different types of catalysts are developed: precious metals and their alloys, metal chelating agent, conducting polymer, transition metal oxides, chalcogenides, nitrides, and metal-free materials.

1.5.1 Precious metals as ORR catalysts

Due to the complicated products, Pt and Pt-based materials [3-7, 17-23] are the only commercial catalyst with precious metal the by now. The reason is that; the d-band orbit of Pt has the empty position to adsorb the O_2 molecular forming the unstable intermediate product, and shows the highest ORR activity in all the precious transition metals. However, the high price, rare reserve, and poor durability limit its application. Most publications suggest that decreasing the diameter of Pt particles, preparation the specific surface orientation or morphology of Pt particles, Pt-based alloy, and searching for the high conductivity and preservative support to loading Pt are the effective methods to optimization the catalytic activity and durability.

(1) The effect of the Pt particle diameter

Pt particles as the ORR catalyst, it is known that the diameter of Pt particles has an important effect on catalytic activity [23, 24]. Decreasing the diameter of Pt particles can promote the dispersion of Pt particles to improve the active surface and reduce the Pt loading. Amra Peles et al. found that the quality activity increase with the decreasing the diameter of Pt particles from 5.5 nm to 2.2 nm [25]. However, the quality activity would be decreased with the decreasing the diameter of Pt particles from 2.2 nm to 1.3 nm due to the negative particle size effect, proved by several groups [26].

(2) The effect of the specific surface orientation or morphology of Pt particles

In the beginning, most scientists believed that the low index planes of Pt crystal have the advantage to promote ORR [27-30]. In 1997, Joelma Perez investigated the cyclic voltammetry (CV) performance for the low index planes of Pt crystal in the 0.1 M $HClO_4$ solution [31]. It is clear that much difference is in the three planes (110), (100), and (111). The detailed data suggest that Pt (110) shows the best ORR performance. They believed that the power of adsorption of O_2 molecular is the main reason.

However, the deeper research showed that the more active sites from the corner and boundary of the high index planes and terraced planes of Pt crystal could improve the catalytic activity [32-35]. In 2012, Professor Nagahiro Hoshi prepared different active planes of Pt crystal. It is clear that the highest electrochemical activity surface orientation is the high index planes of Pt (332) [36]. Yet, another scientist believed that higher index planes Pt (730) and (520) are more active than other index planes [37].

Another important useful method to improve the active sites is to discover different morphology of Pt particles, such as Pt tetra-hexahedron, core-shell structure, and hexagonal nanoplates.

(3) Pt-based alloy

Pt-based alloy obtains not only the excellent properties of Pt but also the original metal properties due to the synergistic effect. Generally, transition metals are introduced into the Pt-based alloy, due to their abundance, low price, and excellent ORR properties. Huang et al. synthesized PtPb/Pt core/shell nanoplates showed better electrochemical activity than commercial Pt/C [38, 39]. They found that the edge, top, and bottom of Pt (110) facets undergo large tensile strains, indicating advantages for helping optimize the Pt-O bond strength. Professor Stamenkovic discovered volcano linear relationship between ORR activity and the transition metal properties [40]. The deeper investigation confirmed that they show the weaker adsorption oxygen molecular than Pt nanoparticle, suggesting that the oxide product can detach in time.

(4) Searching for the high conductivity and preservative support for Pt-loading

Now, the commercial ORR catalyst is using XC-72 as support to load Pt nanoparticles [41-47]. That is due to the carbon material's high surface area and good conductivity [48, 49]. However, the carbon materials are easy to corrosion at the high potential and oxygen bumbling, leading to the Pt nanoparticle loss or oxide [50]. Several new structures of carbon materials were discovered, such as carbon fiber, graphene, carbon nanotube, and grade hole carbon, which were the only oxide on the edge of materials with stable π bonds. Otherwise, new carbon-free materials are also developed, such as WC, WO_x, TiC, TiOx, and some nitrides [51-58].

Although, these methods are beneficial to improve the catalytic activity and the durability. It cannot solve the use of precious metal. Therefore, the limited reserve, high price, poison and oxide of Pt-based materials suggest that developing the precious metal-free catalyst is the fundamental method to promote the commercial development of PEMFCs.

1.5.2 Metal-free catalysts

Carbon materials as the traditional ORR catalyst have the advantages of the rich source, cheap price, high conductivity, environmental, and good stability. As we know, pure carbon is low ORR catalytic activity. The heteroatom (N、B、S and P) single- or co-doped carbon show high catalytic activity [59-63], due to increasing asymmetry of the carbon atomic spin density [59].

Recently, Dai's group researched the p-group elements doped in graphene, confirmed that the ORR catalytic activity has a relation to the free energy of heteroatom atoms. They developed the theory to explain why the N, S, and P atoms doping have a better ORR catalytic activity than other elements in adsorption of electrons and electronegativity. In fact, N-doped carbon is the most investigated materials in the ORR catalysts [60, 64].

There are four types of N-doped carbon structure: oxide N, pyridine-like N, graphite-like N and pyrrole-type N [60, 65]. It is generally believed that pyridine-like N and graphite-like N (named quaternary N) have a higher activity than the other two types, due to that the special structure of the pyridine-like N and the graphite-like N would increase the adsorption ability of the oxygen.

After that, B, S, and P also investigated a lot [66-78]. S atom has a similar electronegativity with a higher diameter than N atoms, promoting ORR with the increasing spin density of carbon brings in structure defect sites. However, single S-doped carbon shows weak ORR catalytic activity due to much more intermediate products and lower electrons transfer number. Normally, S atoms are used to co-dope carbon with other heteroatom atoms [67, 69]. B is another usual heteroatom atom in different theories with N and S [66, 70]. The theory calculation discovered that B-doping would break down the neutral of carbon to form B^+ structure. P element, the same group with N, is an effective heteroatom atom. P atom shows a bigger covalent diameter (107 pm) than carbon atom [68]. When introduced the P atoms doped in carbon, the C-plane structure becomes a conical junction of P atoms combined with three C atoms structure. Therefore, the sp_2 hybrid state will transfer into the sp_3 hybrid state, resulting in more distortion and defects to promote ORR.

Altering the synthesized method to control the material structure, surface area, the type of doped heteroatom atoms, and the amount can improve the heteroatom atom doped carbon electrocatalytic activity, and the theoretical calculation and/or experiment investigated a lot. However, the electrocatalytic activity still cannot compete with commercial Pt/C, and there is no consensus on the active sites. In other views, the metal-free catalyst cannot fully avoid the metal in the sample, due to the trace metal in the preparation of carbon as catalyst. So searching for the metal and heteroatom atoms co-dope carbon materials become a research point.

1.5.3 Transition metal-heteroatom atom co-dope carbon materials as catalysts

Transition metal (Co, Fe, Ni)-heteroatom atom (N, P, S, B) co-dope carbon catalyst is also called metal chelates catalyst, which is firstly found by Professor Jastnski in 1964 with phthalocyanine cobalt promoting ORR [71-74]. After decades, too many metal chelates were published, such as metal phthalocyanine chelate, metal porphyrin chelate, and metal tetraazacyclotrope alkene. Among them, MeN/C was the most studied, N is chelate, Me is transition metal (Fe or Co is the most). Nevertheless, there are also too many key points not clear or need to be overcome [75-77]. Firstly, these materials show good catalytic activity in base solution but not in acid solution, and many publications show that their electrochemical activities are related to the high-temperature carbonization. Secondly, we cannot make sure the relationship between the component and catalytic activity. As we known, the material performance is controlled by material component, but a huge controversy is in the component and performance in MeN/C or the active sites. Thirdly, designing the excellent material structure is good to promote the reaction. Generally, the large surface area is good for supporting active sites, and the suitable hole has advantages to transfer reactants and products, which are beneficial to catalytic reaction.

1.5.4 Metal oxides, nitrides, carbides and other metal-based compounds

In addition, there are also other different types of catalysts, such as oxides (MnOx [78], CoO [79], and Co_3O_4 [80]), chalcogenide compounds (M-X, M=Co, Ru, Re, Rh; X=S, Se, Te) [81-86], nitrides (MoN [87], MoN_2 [88]), carbides (WC [89], FeC [90]) and oxynitrides. However, they have the same shortcoming as the free-noble metal materials.

Therefore, developing free precious metal catalyst with the high activity and the excellent performance in the acidic media, and exploring the catalytic mechanism have the far-reaching theoretical and practical significance.

1.6 The challenges of ORR catalysts for PEMFCs

As the previous discussion, ORR catalysts as the most important part of the cathode are developed for decade's years, but they are still facing many challenges, such as efficient and stability [91-93].

The cathode is the place of accepting the electrons, and absorbing the oxygen to form OH^- [94-98]. It controls the ongoing of the reaction. Although, ORR is investigated more than the hydrogen oxide reaction (HOR), the mechanism of ORR is not clear, due to too many the uncertainties such as the electrolyte and reaction surrounding. [91-96] However, there is a consensus that the unstable intermediate products in the reaction are determined by the thermodynamic but not kinetic reaction. Moreover, the poor reversibility of the unstable intermediate products results in the low exchange current density (ECD). For example, the ECD of the popular commercial catalyst Pt-Pd alloy is less than 10^{-10}~10^{-9} mA/cm^2, much lower than that of the anode. It leads to the high over-potential, and that the onset-potential is only 1 V lower than the theoretical 1.23 V. In the commercial devices, the onset-potential is only lower than 0.8 V.

Improving the catalyst performance is the most suitable method for PEMFCs. However, it is difficult to improve, such as poisoning of CO, loss activity, aggregating, and dissolving [97-101]. More important, not only the price but also the reserved of the precious metal in the earth cannot meet the requirement of the practical. In the anode, only about Pt 0.05 wt. % is enough, but it needs about 40 wt. % in the cathode in the commercial fuel cell. In fact, according to the investigation of the U.S. Department of Energy, 46% of the whole fuel cell price is used for the catalyst.

In summary, improving the fuel cell performance can obtain through the engineering practice and technical research, but there is no ideal way for nonrenewable resource Pt [94, 102]. Therefore, decreasing the Pt-based catalyst amount or discovering new Pt-free catalyst are the most useful method to improve the performance of the PEMFCs.

1.7 Research topic

As discussed above, PEMFC shows much more advantages to response to the energy crisis and environmental pollution, which is considered as the most potential power substitute. However, there is still a key point needs to be considering. Firstly, the high effective Pt nanoparticles are introduced in ORR catalyst to promote the PEMFC practical application. At the same time, the poor stability, easy poison, and high price limited the PEMFC large-scale application. So keeping the high efficiency with decreasing Pt loading is a key point. Secondly, as introduced before, the precious metals free catalyst cannot obtain a comparable catalytic activity with Pt, so how to improve their catalytic activity is the main question. Thirdly, in the past decades, we cannot obtain a suitable support to load precious metal to substitute the commercial carbon. In other words, we cannot avoid the corrosion of carbon. Therefore, searching for an excellent support is another promising method.

To meet these three challenges, in this thesis we use an effective catalyst to decrease the price of PEMFC.

1, Hexagonal nanoplates PtFe alloy with facile operating conditions was prepared to enhance electrocatalytic activity and durability. In this part, we synthesized a series of PtM (M: Fe, Co, Ni) alloy as a catalyst by the mild simple method. The electrochemical measurements confirmed that the transition metals controlled the catalytic activity of Pt-based alloys due to their natural properties. The PtFe alloy catalyst showed the highest catalytic activity due to its homogeneous morphology and ultra-small particle size.

2, Fe, Co incorporated in P-doped porous carbon catalysts were prepared to promote the ORR process. Temperature-dependence of electrocatalytic activity for dual transition metals embedded in P-doped porous carbon was synthesized to enhance ORR performance. This thesis explored the relationship between catalytic activity and carbonization temperature, the ratios of the transition metals. It is interesting that this thesis confirmed that the synergistic effect of dual transition metals is controlled by their ratios.

3. 2D MXene Nb_2C was synthesized as support to improve the ORR process. The traditional molten salt assisted solid-state reaction was used to prepare the product MAX Nb_2AlC at low temperature, which decreased the synthesized temperature from 1600°C to 1000°C. This thesis investigated the effect of the different fluxes, reaction times, heating temperatures, and the amount of the fluxes. The results confirmed that the reaction time is the key factor in the synthesis. Then, the multi-layer MXene Nb_2C was obtained by using the HF solution to etch the MAX Nb_2AlC. At last, we compared the ORR catalytic activity of four samples (Pt-loading or free of before and after HF etching), showing that the multi-layer MXene Nb_2C is beneficial for improving the catalytic stability and activity.

1.8 References

[1] Dicks, A. L.; Rand, D. A. *Fuel cell systems explained*, John Wiley & Sons: 2018.

[2] Saji, V. S. *Electrocatalysts for Low Temperature Fuel Cells: Fundamentals and Recent Trends*, John Wiley & Sons: 2017.

[3] Li, M. *Electrocatalysis in Fuel Cells*. **2014**.

[4] Bradley_Ladewig. *Materials for Low-Temperature Fuel Cells*. **2015**.

[5] Wilkinson, D. P.; Zhang, J.; Hui, R.; Fergus, J.; Li, X. *Proton exchange membrane fuel cells: materials properties and performance*, CRC Press: 2009.

[6] Mehta V, C. J. Review and analysis of PEM fuel cell design and manufacturing. *Journal of Power Sources* **2003,** *114* (1), 32-53.

[7] Bing, Y.; Liu, H.; Zhang, L.; Ghosh, D.; Zhang, J. Nanostructured Pt-alloy electrocatalysts for PEM fuel cell oxygen reduction reaction. *Chemical Society Reviews* **2010,** *39* (6), 2184-2202.

[8] Dai, L.; Xue, Y.; Qu, L.; Choi, H. J.; Baek, J. B. Metal-free catalysts for oxygen reduction reaction. *Chemical Reviews* **2015,** *115* (11), 4823-4892 .

[9] Gawande, M. B. Core–shell nanoparticles: synthesis and applications in catalysis and electrocatalysis. *Chemical Society Reviews* **2015,** *44*, 7540-7590.

[10] Wang, B. Recent development of non-platinum catalysts for oxygen reduction reaction. *Journal of Power Sources* **2005,** *152*, 1-15.

[11] Wroblowa, H. S.; Razumney, G. Electroreduction of oxygen: a new mechanistic criterion. *Journal of Electroanalytical Chemistry and Interfacial Electrochemistry* **1976,** *69* (2), 195-201.

[12] Yeager, E. Electrocatalysts for O_2 reduction. *Electrochimica Acta* **1984,** *29* (11), 1527-1537.

[13] Nørskov, J. K.; Rossmeisl, J.; Logadottir, A.; Lindqvist, L.; Kitchin, J. R.; Bligaard, T.; Jonsson, H. Origin of the over-potential for oxygen reduction at a fuel-cell cathode. *The Journal of Physical Chemistry B* **2004,** *108* (46), 17886-17892.

[14] Perivoliotis, D. K.; Tagmatarchis, N. Recent advancements in metal-based hybrid electrocatalysts supported on graphene and related 2D materials for the oxygen reduction reaction. *Carbon* **2017,** *118*, 493-510.

[15] Gawande, M. B.; Goswami, A.; Felpin, F. X.; Asefa, T.; Huang, X.; Silva, R.; Zou, X.; Zboril, R.; Varma, R. S. Cu and Cu-based nanoparticles: synthesis and applications in catalysis. *Chemical Reviews* **2016,** *116* (6), 3722-3811.

[16] Liu, M.; Zhang, R.; Chen, W. Graphene-supported nanoelectrocatalysts for fuel cells: synthesis, properties, and applications. *Chemical Reviews* **2014,** *114* (10), 5117-5160.

[17] Newton, C. G.; Wang, S. G.; Oliveira, C. C.; Cramer, N. Catalytic enantioselective transformations involving C-H bond cleavage by transition-metal complexes. *Chemical Reviews* **2017,** *117* (13), 8908-8976.

[18] Escudero-Escribano, M.; Malacrida, P.; Hansen, M. H.; Vej-Hansen, U. G.; Velázquez-Palenzuela, A.; Tripkovic, V.; Schiøtz, J.; Rossmeisl, J.; Stephens, I. E.; Chorkendorff, I. Tuning the activity of Pt alloy electrocatalysts by means of the lanthanide contraction. *Science* **2016,** *352* (6281), 73-76.

[19] Wu, J.; Zhang, J.; Peng, Z.; Yang, S.; Wagner, F. T.; Yang, H. Truncated octahedral Pt_3Ni oxygen reduction reaction electrocatalysts. *Journal of the American Chemical Society* **2010,** *132* (14), 4984-4985.

[20] Lee, J.-Y.; Han, S.-B.; Kwak, D.-H.; Kim, M.-C.; Lee, S.; Park, J.-Y.; Choi, I.-A.; Park, H.-S.; Park, K.-W. Porous Cu-rich@Cu_3Pt alloy catalyst with a low Pt loading for enhanced electrocatalytic reactions. *Journal of Alloys and Compounds* **2017,** *691*, 26-33.

[21] Toda, T.; Igarashi, H.; Uchida, H.; Watanabe, M. Enhancement of the electroreduction of oxygen on Pt alloys with Fe, Ni, and Co. *Journal of the Electrochemical Society* **1999,** *146* (10), 3750-3756.

[22] Beermann, V.; Gocyla, M.; Willinger, E.; Rudi, S.; Heggen, M.; Dunin-Borkowski, R. E.; Willinger, M. G.; Strasser, P. Rh-Doped Pt-Ni Octahedral Nanoparticles: Understanding the correlation between elemental distribution, oxygen reduction reaction, and shape stability. *Nano Letters* **2016,** *16* (3), 1719-1725.

[23] Baumgärtner, M.; Raub, J. The electrodeposition of platinum and platinum alloys. *Platinum Metals Review* **1988,** *32* (4), 188-197.

[24] Kinoshita, K. Particle size effects for oxygen reduction on highly dispersed platinum in acid electrolytes. *Journal of the Electrochemical Society* **1990,** *137* (3), 845-848.

[25] Shao, M.; Peles, A.; Shoemaker, K. Electrocatalysis on platinum nanoparticles: particle size effect on oxygen reduction reaction activity. *Nano letters* **2011,** *11* (9), 3714-3719.

[26] Cherstiouk, O.; Simonov, P.; Savinova, E. Model approach to evaluate particle size effects in electrocatalysis: preparation and properties of Pt nanoparticles supported on GC and HOPG. *Electrochimica Acta* **2003,** *48* (25-26), 3851-3860.

[27] Tolmachev, Y. V.; Petrii, O. A. Pt–Ru electrocatalysts for fuel cells: developments in the last decade. *Journal of Solid State Electrochemistry* **2016,** *21*(3), 613-639.

[28] Toda, T.; Igarashi, H.; Uchida, H.; Watanabe, M. Enhancement of the Electroreduction of Oxygen on Pt Alloys with Fe, Ni, and Co. *Journal of The Electrochemical Society* **1999,** *146* (10), 3750-3756.

[29] Silva, L. S. R.; López-Suárez, F. E.; Perez-Cadenas, M.; Santos, S. F.; da Costa, L. P.; Eguiluz, K. I. B.; Salazar-Banda, G. R. Synthesis and characterization of highly active Pbx@Pty/C core-shell nanoparticles toward glycerol electrooxidation. *Applied Catalysis B: Environmental* **2016,** *198*, 38-48.

[30] Narayanamoorthy, B.; Linkov, V.; Sita, C.; Pasupathi, S. Pt_3M (M: Co, Ni and Fe) bimetallic alloy nanoclusters as support-free electrocatalysts with improved activity and durability for dioxygen reduction in PEM fuel cells. *Electrocatalysis* **2016,** *7* (5), 400-410.

[31] Perez, J.; Villullas, H.; Gonzalez, E.R. Structure sensitivity of oxygen reduction on platinum single crystal electrodes in acid solutions. *Journal of Electroanalytical Chemistry* **1997,** *435*, 179-187.

[32] Blakely, D.; Somorjai, G. The stability and structure of high miller index platinum crystal surfaces in vacuum and in the presence of adsorbed carbon and oxygen. *Surface Science* **1977,** *65* (2), 419-442.

[33] Chen, C.-H.; Meadows, K. E.; Cuharuc, A.; Lai, S. C.; Unwin, P. R. High resolution mapping of oxygen reduction reaction kinetics at polycrystalline platinum electrodes. *Physical Chemistry Chemical Physics* **2014,** *16* (34), 18545-18552.

[34] Long, N. V.; Ohtaki, M.; Uchida, M.; Jalem, R.; Hirata, H.; Chien, N. D.; Nogami, M. Synthesis and characterization of polyhedral Pt nanoparticles: their catalytic property, surface attachment, self-aggregation and assembly. *Journal of colloid and interface science* **2011,** *359* (2), 339-350.

[35] Wang, X.; Choi, S. I.; Roling, L. T.; Luo, M.; Ma, C.; Zhang, L.; Chi, M.; Liu, J.; Xie, Z.; Herron, J. A.; Mavrikakis, M.; Xia, Y. Palladium-platinum core-shell icosahedra with substantially enhanced activity and durability towards oxygen reduction. *Nature communications* **2015,** *6*, 7594.

[36] Hitotsuyanagi, A.; Nakamura, M.; Hoshi, N. Structural effects on the activity for the oxygen reduction reaction on n (111)–(100) series of Pt: correlation with the oxide film formation. *Electrochimica Acta* **2012,** *82*, 512-516.

[37] Tian, N.; Zhou, Z.-Y.; Sun, S.-G.; Ding, Y.; Wang, Z. L. Synthesis of tetrahexahedral platinum nanocrystals with high-index facets and high electro-oxidation activity. *Science* **2007,** *316* (5825), 732-735.

[38] Bu, L.; Zhang, N.; Guo, S.; Zhang, X.; Li, J.; Yao, J.; Wu, T.; Lu, G.; Ma, J.-Y.; Su, D. Biaxially strained PtPb/Pt core/shell nanoplate boosts oxygen reduction catalysis. *Science* **2016,** *354* (6318), 1410-1414.

[39] Wu, Y.; Wang, D.; Niu, Z.; Chen, P.; Zhou, G.; Li, Y. A strategy for designing a concave Pt-Ni alloy through controllable chemical etching. *Angewandte Chemie International Edition* **2012,** *51* (50), 12524-12528.

[40] Stamenkovic, V. R.; Mun, B. S.; Arenz, M.; Mayrhofer, K. J.; Lucas, C. A.; Wang, G.; Ross, P. N.; Markovic, N. M. Trends in electrocatalysis on extended and nanoscale Pt-bimetallic alloy surfaces. *Nature Materials* **2007,** *6* (3), 241-247.

[41] Jana, P. P.; Lidin, S. Structural impact of platinum on the incommensurably modulated gamma-brass related composite structure $Pd_{15}Zn_{54}$. *Inorganic Chemistry* **2012,** *51* (18), 9893-901.

[42] Choi, K. –H.; Jang, Y.; Chung, D. Y.; Seo, P.; Jun, S. W.; Lee, J. E.; Hwan Oh, M.; Shokouhimehr, M.; Jung, N.; Yoo, S. J.; Sung, Y. – E.; Hyeon, T. A simple synthesis of urchin-like Pt-Ni bimetallic nanostructures as enhanced electrocatalysts for oxygen reduction reaction. *Chemical Communications* **2016**, *52*, 597-600...

[43] Kuroki, H.; Tamaki, T.; Matsumoto, M.; Arao, M.; Kubobuchi, K.; Imai, H.; Yamaguchi, T. Platinum–iron-nickel trimetallic catalyst with superlattice structure for enhanced oxygen reduction activity and durability. *Industrial & Engineering Chemistry Research* **2016,** *55* (44), 11458-11466.

[44] Vinayan, B. P.; Ramaprabhu, S. Platinum-TM (TM = Fe, Co) alloy nanoparticles dispersed nitrogen doped (reduced graphene oxide-multiwalled carbon nanotube) hybrid structure cathode electrocatalysts for high performance PEMFC applications. *Nanoscale* **2013,** *5* (11), 5109-5118.

[45] Zhang, Y.; Chen, T.; Alia, S.; Pivovar, B. S.; Xu, W. Single-molecule nanocatalysis shows in situ deactivation of Pt/C electrocatalysts during the hydrogen-oxidation reaction. *Angewandte Chemie International Edition* **2016,** *55* (9), 3086-3090.

[46] Sahin, N. E.; Napporn, T. W.; Dubau, L.; Kadirgan, F.; Léger, J.-M.; Kokoh, K. B. Temperature-dependence of oxygen reduction activity on Pt/C and PtCr/C electrocatalysts synthesized from microwave-heated diethylene glycol method. *Applied Catalysis B: Environmental* **2017,** *203*, 72-84.

[47] Pullamsetty, A.; Subbiah, M.; Sundara, R. Platinum on boron-doped graphene as cathode electrocatalyst for proton exchange membrane fuel cells. *International Journal of Hydrogen Energy* **2015,** *40* (32), 10251-10261.

[48] Jung, N.; Chung, D. Y.; Ryu, J.; Yoo, S. J.; Sung, Y.-E. Pt-based nanoarchitecture and catalyst design for fuel cell applications. *Nano Today* **2014,** *9* (4), 433-456.

[49] Chiwata, M.; Yano, H.; Ogawa, S.; Watanabe, M.; Iiyama, A.; Uchida, H. Oxygen reduction reaction activity of Carbon-supported Pt-Fe, Pt-Co, and Pt-Ni alloys with stabilized Pt-skin layers. *Electrochemistry* **2016,** *84* (3), 133-137.

[50] Han, B.; Carlton, C. E.; Suntivich, J.; Xu, Z.; Shao-Horn, Y. Oxygen reduction activity and stability trends of bimetallic $Pt_{0.5}M_{0.5}$ nanoparticle in acid. *The Journal of Physical Chemistry C* **2015,** *119* (8), 3971-3978.

[51] Šljukić, B.; Martins, M.; Kayhan, E.; Balčiūnaitė, A.; Şener, T.; Sequeira, C. A. C.; Santos, D. M. F. SnO_2 -C supported PdNi nanoparticles for oxygen reduction and borohydride oxidation. *Journal of Electroanalytical Chemistry* **2017,** *797*, 23-30.

[52] Galeano, C.; Meier, J. C.; Peinecke, V.; Bongard, H.; Katsounaros, I.; Topalov, A. A.; Lu, A.; Mayrhofer, K. J.; Schüth, F. Toward highly stable electrocatalysts via nanoparticle pore confinement. *Journal of the American Chemical Society* **2012,** *134* (50), 20457-20465.

[53] Fang, B.; Kim, J. H.; Kim, M.; Yu, J.-S. Ordered hierarchical nanostructured carbon as a highly efficient cathode catalyst support in proton exchange membrane fuel cell. *Chemistry of Materials* **2009,** *21* (5), 789-796.

[54] Liu, Y.; Shrestha, S.; Mustain, W. E. Synthesis of nanosize tungsten oxide and its evaluation as an electrocatalyst support for oxygen reduction in acid media. *ACS Catalysis* **2012,** *2* (3), 456-463.

[55] Tsuji, M.; Uto, K.; Nagami, T.; Muto, A.; Fukushima, H.; Hayashi, J.-I. Synthesis of carbon-supported Pt-YOx and PtY nanoparticles with high catalytic activity for the oxygen reduction reaction using a microwave-based polyol method. *ChemCatChem* **2017,** *9* (6), 962-970.

[56] Senevirathne, K.; Hui, R.; Campbell, S.; Ye, S.; Zhang, J. Electrocatalytic activity and durability of Pt/NbO_2 and Pt/Ti_4O_7 nanofibers for PEM fuel cell oxygen reduction reaction. *Electrochimica Acta* **2012,** *59*, 538-547.

[57] Liu, H.-j.; Wang, F.; Zhao, Y.; Fong, H. Mechanically resilient electrospun TiC nanofibrous mats surface-decorated with Pt nanoparticles for oxygen reduction reaction with enhanced electrocatalytic activities. *Nanoscale* **2013,** *5* (9), 3643-3647.

[58] Xie, X.; Chen, S.; Ding, W.; Nie, Y.; Wei, Z. An extraordinarily stable catalyst: Pt NPs supported on two-dimensional $Ti_3C_2X_2$ (X = OH, F) nanosheets for oxygen reduction reaction. *Chemical Communications* **2013,** *49* (86), 10112-10114.

[59] Navalon, S.; Dhakshinamoorthy, A.; Alvaro, M.; Antonietti, M.; Garcia, H. Active sites on graphene-based materials as metal-free catalysts. *Chemical Society Reviews* **2017,** *46* (15), 4501-4529.

[60] Chen, C.; Sun, Z.; Li, Y.; Yi, L.; Hu, H. Self-assembly of N doped 3D porous carbon frameworks from carbon quantum dots and its application for oxygen reduction reaction. *Journal of Materials Science: Materials in Electronics* **2017,** *28* (17), 12660-12669.

[61] Zhao, Y.; Yang, L.; Chen, S.; Wang, X.; Ma, Y.; Wu, Q.; Jiang, Y.; Qian, W.; Hu, Z. Can boron and nitrogen co-doping improve oxygen reduction reaction activity of carbon nanotubes? *Journal of the American Chemical Society* **2013,** *135* (4), 1201-1204.

[62] Yang, Z.; Yao, Z.; Li, G.; Fang, G.; Nie, H.; Liu, Z.; Zhou, X.; Chen, X.; Huang, S. Sulfur-doped graphene as an efficient metal-free cathode catalyst for oxygen reduction. *ACS Nano* **2011,** *6* (1), 205-211.

[63] Choi, C. H.; Park, S. H.; Woo, S. I. Phosphorus–nitrogen dual doped carbon as an effective catalyst for oxygen reduction reaction in acidic media: effects of the amount of P-doping on the physical and electrochemical properties of carbon. *Journal of Materials Chemistry* **2012,** *22* (24), 12107-12115.

[64] Gong, K.; Du, F.; Xia, Z.; Durstock, M.; Dai, L. Nitrogen-doped carbon nanotube arrays with high electrocatalytic activity for oxygen reduction. *Science* **2009,** *323* (5915), 760-764.

[65] Guo, D.; Shibuya, R.; Akiba, C.; Saji, S.; Kondo, T.; Nakamura, J. Active sites of nitrogen-doped carbon materials for oxygen reduction reaction clarified using model catalysts. *Science* **2016,** *351* (6271), 361-365.

[66] Yan, D.; Li, Y.; Huo, J.; Chen, R.; Dai, L.; Wang, S. Defect chemistry of nonprecious-metal electrocatalysts for oxygen reactions. *Advanced Materials* **2017**, DOI: 10.1002/adma.201606459.

[67] Ito, Y.; Cong, W.; Fujita, T.; Tang, Z.; Chen, M. High catalytic activity of nitrogen and sulfur co-doped nanoporous graphene in the hydrogen evolution reaction. *Angewandte Chemie Internationall Edition* **2015,** *54* (7), 2131-2136.

[68] Zhang, J.; Qu, L.; Shi, G.; Liu, J.; Chen, J.; Dai, L. N, P-codoped carbon networks as efficient metal-free bifunctional catalysts for oxygen reduction and hydrogen evolution reactions. *Angewandte Chemie Internationall Edition* **2016,** *55* (6), 2230-2234.

[69] Sun, T.; Wu, Q.; Jiang, Y.; Zhang, Z.; Du, L.; Yang, L.; Wang, X.; Hu, Z. Sulfur and nitrogen codoped carbon tubes as bifunctional metal-free electrocatalysts for oxygen reduction and hydrogen evolution in acidic medium. *Chemistry A European Journal Communication* **2016,** *22*(30), 10326-10329.

[70] Jiao, Y.; Zheng, Y.; Jaroniec, M.; Qiao, S. Z. Origin of the electrocatalytic oxygen reduction activity of graphene-based catalysts: a roadmap to achieve the best performance. *Journal of the American Chemical Society* **2014,** *136* (11), 4394-4403.

[71] Jasinski, R. A new fuel cell cathode catalyst. *Nature* **1964,** *201* (4925), 1212-1213.

[72] Ohms, D.; Herzog, S.; Franke, R.; Neumann, V.; Wiesener, K. Influence of metal ions on the

electrocatalytic oxygen reduction of carbon materials prepared from pyrolyzed polyacrylonitrile. *Journal of Power Sources* **1992,** *38*, 327-334.

[73] Zhu, C.; Li, H.; Fu, S.; Du, D.; Lin, Y. Highly efficient nonprecious metal catalysts towards oxygen reduction reaction based on three-dimensional porous carbon nanostructures. *Chemical Society Reviews* **2016,** *45* (3), 517-531.

[74] Liu, Y.; Yue, X.; Li, K.; Qiao, J.; Wilkinson, D. P.; Zhang, J. PEM fuel cell electrocatalysts based on transition metal macrocyclic compounds. *Coordination Chemistry Reviews* **2016,** *315*, 153-177.

[75] Liu, Y.; Jiang, H.; Zhu, Y.; Yang, X.; Li, C. Transition metals (Fe, Co, and Ni) encapsulated in nitrogen-doped carbon nanotubes as bi-functional catalysts for oxygen electrode reactions. *Journal of Materials Chemistry A* **2016,** *4* (5), 1694-1701.

[76] Abdol Rahim, A. H.; Tijani, A. S.; Kamarudin, S. K.; Hanapi, S. An overview of polymer electrolyte membrane electrolyzer for hydrogen production: Modeling and mass transport. *Journal of Power Sources* **2016,** *309*, 56-65.

[77] Osmieri, L.; Monteverde Videla, A.; Specchia, S. In Optimization of a Fe-N-C electrocatalyst supported on ordered mesoporous carbon functionalized with polypyrrole for oxygen reduction reaction. *Fuel Cells and Advanced Batteries* **2015,** 5-8.

[78] Meng, Y.; Song, W.; Huang, H.; Ren, Z.; Chen, S.-Y.; Suib, S. L. Structure–property relationship of bifunctional MnO_2 nanostructures: highly efficient, ultra-stable electrochemical water oxidation and oxygen reduction reaction catalysts identified in alkaline media. *Journal of the American Chemical Society* **2014,** *136* (32), 11452-11464.

[79] Guo, S.; Zhang, S.; Wu, L.; Sun, S. Co/CoO nanoparticles assembled on graphene for electrochemical reduction of oxygen. *Angewandte Chemie Internationall Edition* **2012,** *124* (47), 11940-11943.

[80] Xu, J.; Gao, P.; Zhao, T. Non-precious Co_3O_4 nano-rod electrocatalyst for oxygen reduction reaction in anion-exchange membrane fuel cells. *Energy & Environmental Science* **2012,** *5* (1), 5333-5339.

[81] Han, L.; Dong, S.; Wang, E. Transition-metal (Co, Ni, and Fe)-based electrocatalysts for the water oxidation reaction. *Advanced Materials* **2016,** *28*(42), 9266-9291.

[82] Wang, H.; Liang, Y.; Li, Y.; Dai, H. $Co_{1-x}S$–graphene hybrid: a high-performance metal chalcogenide electrocatalyst for oxygen reduction. *Angewandte Chemie International Edition* **2011,** *50* (46), 10969-10972.

[83] Uehara, N.; Ishihara, A.; Nagai, T.; Matsumoto, M.; Imai, H.; Kohno, Y.; Matsuzawa, K.; Mitsushima, S.; Ota, K. Kinetic study of oxygen reduction reaction on tantalum oxide-based electrocatalysts produced from oxy-tantalum phthalocyanines in acidic media. *Electrochimica Acta* **2015,** *182*, 789-794.

[84] Wang, T.; Gao, D.; Zhuo, J.; Zhu, Z.; Papakonstantinou, P.; Li, Y.; Li, M. Size-dependent enhancement of electrocatalytic oxygen-reduction and hydrogen-evolution performance of MoS_2 particles. *Chemistry A European Journal Communication* **2013,** *19* (36), 11939-11948.

[85] Cao, B.; Veith, G. M.; Diaz, R. E.; Liu, J.; Stach, E. A.; Adzic, R. R.; Khalifah, P. G. Cobalt molybdenum oxynitrides: synthesis, structural characterization, and catalytic activity for the oxygen reduction reaction. *Angewandte Chemie International Edition* **2013,** *52* (41), 10753-10757.

[86] Yang, J.; Zhu, G.; Liu, Y.; Xia, J.; Ji, Z.; Shen, X.; Wu, S. Fe_3O_4-decorated Co_9S_8 nanoparticles in situ grown on reduced graphene oxide: a new and efficient electrocatalyst for oxygen evolution reaction. *Advanced Functional Materials* **2016,** *26* (26), 4712-4721.

[87] Xia, D.; Liu, S.; Wang, Z.; Chen, G.; Zhang, L.; Zhang, L.; Hui, S. R.; Zhang, J. Methanol-tolerant MoN electrocatalyst synthesized through heat treatment of molybdenum tetraphenylporphyrin for four-electron oxygen reduction reaction. *Journal of Power Sources* **2008,** *177* (2), 296-302.

[88] Cao, B.; Veith, G. M.; Neuefeind, J. C.; Adzic, R. R.; Khalifah, P. G. Mixed close-packed cobalt molybdenum nitrides as non-noble metal electrocatalysts for the hydrogen evolution reaction. *Journal of the American Chemical Society* **2013,** *135* (51), 19186-19192.

[89] Kang, J.; Kim, H.-m.; Saito, N.; Lee, M.-H. A simple synthesis method for nanostructured Co-WC/carbon composites with enhanced oxygen reduction reaction activity. *Science and Technology of Advanced Materials* **2016,** *17* (1), 37-44.

[90] Kim, J. H.; Sa, Y. J.; Jeong, H. Y.; Joo, S. H. Roles of Fe-N_x and Fe-Fe_3C@C species in Fe-N/C electrocatalysts for oxygen reduction reaction. *ACS Applied Materials & Interfaces* **2017,** *9* (11), 9567-9575.

[91] Zhang, W.; Lai, W.; Cao, R. Energy-related small molecule activation reactions: oxygen reduction and hydrogen and oxygen evolution reactions catalyzed by porphyrin- and corrole-based systems. *Chemical reviews* **2017,** *117* (4), 3717-3797.

[92] Zhu, F.; Kim, J.; Tsao, K.-C.; Zhang, J.; Yang, H. Recent development in the preparation of nanoparticles as fuel cell catalysts. *Current Opinion in Chemical Engineering* **2015,** *8*, 89-97.

[93] He, C.; Desai, S.; Brown, G.; Bollepalli, S. PEM fuel cell catalysts: cost, performance, and durability. *Electrochemical Society Interface* **2005,** *14*(3), 41-44.

[94] Chia, X.; Eng, A. Y.; Ambrosi, A.; Tan, S. M.; Pumera, M. Electrochemistry of nanostructured layered transition-metal dichalcogenides. *Chemical Reviews* **2015,** *115* (21), 11941-11966.

[95] Shao, M.; Chang, Q.; Dodelet, J. P.; Chenitz, R. Recent advances in electrocatalysts for oxygen reduction reaction. *Chemical Reviews* **2016,** *116* (6), 3594-657.

[96] Nie, Y.; Li, L.; Wei, Z. Recent advancements in Pt and Pt-free catalysts for oxygen reduction reaction. *Chemical Society Reviews* **2015,** *44* (8), 2168-2201.

[97] Zhang, C.; Shen, X.; Pan, Y.; Peng, Z. A review of Pt-based electrocatalysts for oxygen reduction reaction. *Frontiers in Energy* **2017,** *11* (3), 268-285.

[98] He, Q.; Cairns, E. J. Review—recent progress in electrocatalysts for oxygen reduction suitable for alkaline anion exchange membrane fuel cells. *Journal of The Electrochemical Society* **2015,** *162* (14), 1504-1539.

[99] Wang, Y. J.; Wilkinson, D. P.; Zhang, J. Noncarbon support materials for polymer electrolyte membrane fuel cell electrocatalysts. *ChemicalReviews* **2011,** *111* (12), 7625-7651.

[100] Wang, Y. J.; Zhao, N.; Fang, B.; Li, H.; Bi, X. T.; Wang, H. Carbon-supported Pt-based alloy electrocatalysts for the oxygen reduction reaction in polymer electrolyte membrane fuel cells: particle size, shape, and composition manipulation and their impact to activity. *Chemical Reviews* **2015,** *115* (9), 3433-3467.

[101] Li, J.; Guttinger, R.; More, R.; Song, F.; Wan, W.; Patzke, G. R. Frontiers of water oxidation: the quest for true catalysts. *Chemical Society Reviews* **2017,** *46* (20), 6124-6147.

[102] Latsuzbaia, R.; Negro, E.; Koper, G. Synthesis, stabilization and activation of Pt nanoparticles for PEMFC applications. *Fuel Cells* **2015,** *15* (4), 628-638.

Chapter 2 Experimental section for electrode preparation, physic characteristic, and data analysis

2.1 Raw materials and instruments

All the raw materials purchased from the company are listed in Table 2.1 without any further treatment. The instruments used in the experiment are shown in Table 2.2.

Table 2.1 The starting materials used in the experiments in this thesis

Reagent	Purity	Company
Chloroplatinic acid	99.99%	Sigma-aldrich
Formic acid	98%	Wako Pure Chemical Industries
XC-72	99.99%	Strem chemicals
HCl	36.5%	Wako Pure Chemical Industries
CoCl2	99.5%	Wako Pure Chemical Industries
FeCl3	99.5%	Wako Pure Chemical Industries
NiCl2	99.5%	Wako Pure Chemical Industries
Phytic acid	98%	Wako Pure Chemical Industries
NaOH	99%	Wako Pure Chemical Industries
Nb powder	99.99%	Wako Pure Chemical Industries
Al powder	99%	Wako Pure Chemical Industries
Graphene	99.7%	Macklin Co., LTD.
NaCl	AR	Sigma-aldrich
2-Propanol	Super Dehydrated	Wako Pure Chemical Industries
KF	99%	Wako Pure Chemical Industries
LiF	99%	Wako Pure Chemical Industries
KCl	99%	Wako Pure Chemical Industries
HClO4	70%	Wako Pure Chemical Industries
KOH	99%	Wako Pure Chemical Industries
Ethanol	99.5%	Wako Pure Chemical Industries

Table 2.2 The instruments used in the experiments in this thesis

Apparatus	MODEL	Company
Muffle Furnace	FO300	Yamato Scientific Co., Ltd., Japan
Electrochemical workstation	CHI-760	CH Instruments, Inc. China
Compact pine rotator	AFCPRBE	Pine Instrument Company, USA
Electrolyte cell	RRPG310	Pine Instrument Company, USA
Counter electrode	AFCTR5	Pine Instrument Company, USA
Working electrode	E7R9	Pine Instrument Company, USA
Reference electrode	RREF0024	Pine Instrument Company, USA
Hot stirrer	CHPS-170DN	As one Co., Ltd., Japan
Vacuum oven	AVO250N	As one Co., Ltd., Japan
Normal oven	SONW-450S	As one Co., Ltd., Japan
Balance	VIBRA	Shinko denshi Co., Ltd., Japan
Balance	New Classic ML	Mettler toledo Co., Ltd., Japan
Dryer	EKK-450	As one Co., Ltd., Japan
Energy dispersive X-ray spectrometry	Genesis XM2	EDAX Co., Ltd., Japan
X-ray diffractometer	Rigaku	Rigaku Co., Ltd, Japan
Scanning electron microscope	JCM-6000	JEOL Co., Ltd, Japan
Inductively coupled plasma	SPS1700HVR	Seiko Instruments Co., Ltd., Japan
ionization energy measuring device	KV205-HK	Bunkoukeiki Co., Ltd, Japan

X-ray photoelectron spectroscopy	AXIS-HS	KRATOS Co., Ltd., Japan
Tube Furnace	ARF-30KC	ASAHI RIKA Co., Ltd., Japan
Field emission-scanning electron microscope	S5200	Hitachi Co., Ltd., Japan

2.2 Physical characterization and electrode preparation

2.2.1 X-ray diffraction

X-ray diffraction (XRD) is used to measure the crystal structure, which can analyze the materials with qualitative and quantitative. The prepared samples recorded on Rigaku D/MAX2550 diffractometer using Cu-Ka radiation (35 kV, 25 mA, λ= 1.54056 Å) with a scanning rate of 5° min^{-1}.

2.2.2 The morphology and microstructure characterization

The morphology and microstructure of the samples are analyzed by transmission electron microscopy (TEM, Tecnai G2 F20 S-TWIN at 200kV) and search engine marketing (SEM, JSM-6701).

2.2.3 Specific surface and pore size analysis

Specific surface is the total surface area per unit mass of the materials, used to calculate the surface area of sample particle. As we know, the specific surface area has a strong correlation with the adsorption of materials and stability. The high specific surface area is beneficial to the catalytic activity, because the higher specific surface area would expose more structure defect to increase the active sites. Therefore, it is important to explore the specific surface area of samples. In this thesis, Autosorb-iQ2 (Quantachrome Instruments) is used to obtain the surfaces area and the pore size distribution with nitrogen adsorption-desorption measurements at -196^{o}C. In detail, the specific surface area is calculated by the Brunauer-Emmett-Teller (BET) method, and pore size distribution from the N_2 adsorption is calculated by the quenched solid density functional theory (QSDFT). All the samples are outgassed under vacuum at 200^{o}C for 10 h using a turbo-molecular vacuum pump before the sorption.

2.2.4 Inductively coupled plasma-atomic emission spectrometry

Generally, the trace amount of transition metals is confirmed by the inductively coupled plasma-atomic emission spectrometry (ICP-AES, SPS1700HVR). The solution is prepared as the following process: 50 mg samples dissolved in the HCl: HNO_3 = 3:1 mixture solution stirring for 48 h, and then added the ultrapure water up to 50 mL with the filtrate.

2.2.5 X-ray photoelectron spectroscopy

In order to analyze the state of chemical bonds and valence, X-ray photoelectron spectroscopy (XPS, ESCALAB 250Xi system using monochromatic Cu KR X-ray source) is used. All the results are calibrated by the C 1s (284.6 eV).

2.2.6 Energy dispersive spectrometer

Energy dispersive X-ray spectrometry (EDS, Genesis XM2, EDAX) is recorded to determine the type of different elements and their stoichiometric ratio of the material.

2.2.7 Rotating disk electrode test system

Rotating disk electrode (RDE) is used to analyze the distribution of current density with the reduced or eliminated the effects of the diffusion layer. In this thesis, the standard three-electrode system connected to a CHI 760E electrochemistry workstation is the test system. Ag/AgCl with saturated 3 M KCl solution is the reference electrode. The platinum wire is acted as the counter electrode, and the working electrode preparation will be discussed in the following.

2.2.8 The preparation of working electrode and electrolyte

The catalyst ink is prepared by the following method. 4 mg prepared sample is dispersed in the mixture solution: 100 μL Nafion solution (5 wt.%), 150 μL ultrapure water and 250 μL isopropyl alcohol, and then kept in the ultrasonic bath more than 30 min to obtain the catalyst ink. In the measurement, the suitable volume ink is transferred onto the surface of glass-carbon (GC) by the micropipette, and then kept in the open oven at 60°C for 15 min, which is used as the working electrode. For the comparison, the Pt/C catalyst ink is prepared as the same process. The 0.1 M KOH or 0.1 M $HClO_4$ solution is the electrolyte.

2.3 The electrochemical measurements and analysis

This part is used to introduce the different methods of electrochemical measurements and the analyses.

2.3.1 Cyclic voltammetry

Cyclic voltammetry (CV), one of the most commonly used electroanalytical techniques, is an excellent method, which is used to analyze the electrochemical process between the electrode and the surface of the electrolyte. In order to receive the precise data, all the tools such as the cell, the reference electrode, and the counter electrode need to be washed by the ultrapure water (Millipore, 18.2 MU cm). All the catalysts prepared in this thesis including Pt/C should be acquired the CV curves in N_2 and O_2 saturated electrolyte. Bumbling more than 30 min N_2 obtain the CV curves in the N_2 saturated electrolyte, and then bumbling more than 30 min O_2 obtain the CV curves in the O_2 saturated electrolyte, the potential range from -0.2 to 1 V in acidic medium and -1 to 0.2 V in alkaline medium (corresponding to the Ag/AgCl as reference electrode). It should be noted that the catalysts need to be electrochemical washing named as activation before taking points: the working electrode is cycled at least five times before the data recorded in all CV tests.

Figure 2.1 is a standard CV curve of Pt/C in the 0.1 M $HClO_4$ solution. There is three main part in the CV curve: H zone, double layer, and O zone. In the H zone, peak 1 and peak 2 are the H desorption, peak 5 and peak 6 are the H adsoption. The double layer is charging showing the lower current. O zone includes the O desorption and adsorption, corresponding to the decomposition of water. Peak 4 is the oxygen reduced peak, which is the most important for ORR.

Generally, in the different CV curves may be not clearly showing all the peaks like the Figure 2.1, due to the different reaction mechanisms. However, the peak 4 is the most important due to it is the reflection of ORR catalytic activity.

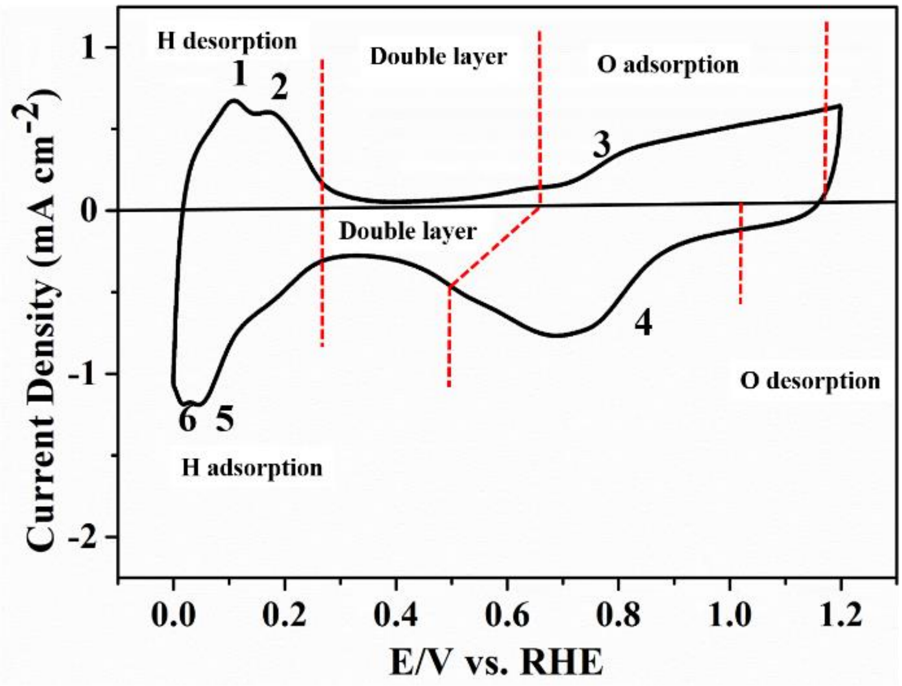

Figure 2.1 The CV curve of commercial Pt/C in 0.1 M $HClO_4$ solution with the scan rate of 10 mV/s at room temperature.

2.3.2 Linear sweep voltammetry

Linear sweep voltammetry (LSV) is to add a changing potential to obtain a curve, which is the current changing with the potential, suggesting the catalytic activity. The detailed test process in this thesis is the following: The onset-potential and the limited current are measured by displaying the catalytic activity. Bumbling more than 30 min N_2 to remove the reflect of H_2 and then bumbling more than 30 min O_2, we obtain in the O_2 saturated electrolyte. In order to further analyze the catalytic activity, LSV curves with different rotation speeds are needed: 625, 900, 1225, 1600, 2025 and 2500 rpm/min with the potential range from -0.2 to 1 V in acidic medium and -1 to 0.2 V in alkaline medium (corresponding to the Ag/AgCl as reference electrode).

Figure 2.2 is a typical ORR LSV curve. Clearly, the current density relies on the kinetic controlled in the high potential, the mix kinetic-diffusion controlled in the intermediate potential, and the diffusion controlled in the low potential. We can also obtain three parameters in the curve: onset-potential, half wave-potential, and the limited current. There are three pathways to confirm the onset potential: one is the point of zero current, one is the point at 0.1 mA/cm^2, and the last one the intersection of the kinetic controlled and the mix kinetic-diffusion controlled. In this thesis, the onset-potential is obtained from the last one method.

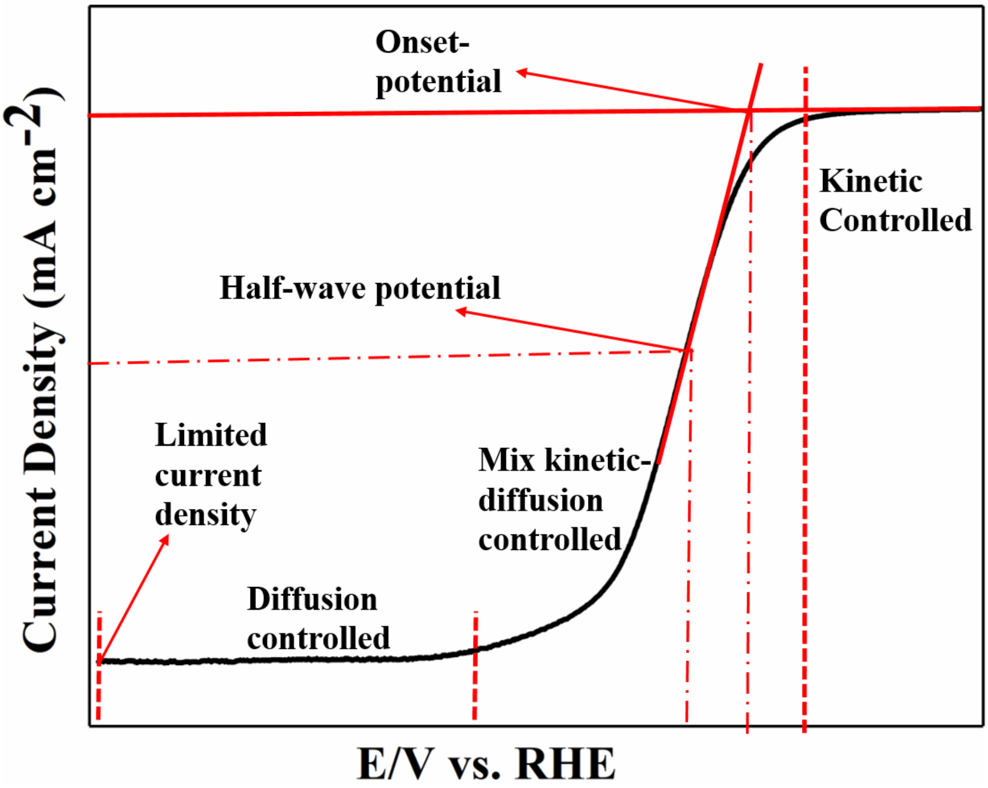

Figure 2.2 The typical LSV curve of the commercial Pt/C catalyst in the electrolyte with the scan rate of 10 mV/s at room temperature.

2.3.3 Koutecky–Levich curve

As introduced in Chapter 1, there are two thoroughly different electron transfer pathways, calculated by the Koutecky–Levich (K–L) equation [1-2]:

$$1/j=1/j_k+1/j_d=1/j_k+1/(B\omega_{1/2})$$

Among them, j is the measurement current density, j_d is the limited diffusion current density, j_k is the kinetic current density, ω is the rotation speed, and B is the Levich slope called B factor, obtained from the equation:

$$B=0.62nFD_{O2}^{2/3}v^{-1/6}C_{O2}$$

n is the number of electron transfer, F is the Faraday's constant 96485 C/mol; D_{O2} is the coefficient of diffusion (1.86×10^{-5} cm^2/s in alkaline solution); v is the dynamic viscosity (0.01 cm^2/s); C is the solubility of oxygen in the electrolyte (12).

Thus, we can obtain the number of electron transfer n combined with this two equations.

2.3.4 Chronoamperometry

Chronoamperometry is performed to explore the stability of the catalysts, which measure the charging current with the time at the constant voltage. In this thesis, the detailed measurement process is that: testing in the O_2-saturated 0.1 M KOH or HClO4 solution electrolyte with a rotation speed of 400 rpm at the -0.5 V or 0.2 V (corresponding to the Ag/AgCl as the reference electrode) for 30000 s, respectively.

2.3.5 Electronic impedance spectroscopy

Electronic impedance spectroscopy (EIS) refers to a small amplitude symmetrical sine wave alternating current impedance method, used to analyze the physical properties of catalysts and the effect of electrochemical reaction on interface impedance. In the thesis, CHI 760 electrochemical workstation is used to record in the O_2-saturated 0.1 M KOH or $HClO_4$ solution electrolyte. The measurements range is from 0.1 to 1×10^6 Hz at the open voltage. The ZView software is used to simulate the schematic illustrations of the equivalent circuit in the EIS of the samples.

2.3.6 Tafel curve

In the dynamic process of electrochemical reaction, Tafel curve displays the correlation between the over-potential and current density, which is a typical line relationship. In the high polarization condition, the over-potential and current density meet the following equation [3-5]:

$$\eta=2.303RT/(anF)\log(j_k/j_d)$$

where a is the electron transfer coefficient, R is the gas constant, F is the Faraday's constant 96485 C/mol, T is the temperature, the j_k is the kinetic current density, n is the number of electrons transferred in the rate determining step, and j_d is the exchange current density. Simplified this equation, we can obtain the following equation:

$$\eta = a + b\log j_k$$

so $a = (-2.303RT/anF)\log j_d$ and the Tafel slope $b = 2.303RT/anF$, in other words, electrocatalysts with low Tafel slopes and high exchange current density are better catalysts in reducing activation polarization. Generally, according to the peer report that the Tafel slope b is close to 60 mV per decade.

Connected with the K–L equation in **2.3.3**, the kinetic current was calculated from the mass transport correction of the LSV curve with a rotation speed of 1600 rpm in this thesis using the following equation:

$$J_K = (J \times J_L)/ (J_L - J)$$

In the equation, J is the measured current density on the GC disk, and J_K and J_L are the kinetic and limited diffusion current densities, respectively.

2.4 References

[1] Zhu, F.; Kim, J.; Tsao, K.-C.; Zhang, J.; Yang, H. Recent development in the preparation of nanoparticles as fuel cell catalysts. *Current Opinion in Chemical Engineering* **2015,** *8*, 89-97.

[2] He, C.; Desai, Brown, G.; Bollepalli, S. PEM fuel cell catalysts: cost, performance, and durability. *Electrochemical Society Interface* **2005,** *14*(3), 41-44.

[3] Saji, V. S. Electrocatalysts for Low Temperature Fuel Cells: Fundamentals and Recent Trends, John Wiley & Sons: 2017.

[4] Meng_Li. Electrocatalysis in Fuel Cells. **2014**.

[5] Zhang, C.; Shen, X.; Pan, Y.; Peng, Z. A review of Pt-based electrocatalysts for oxygen reduction reaction. *Frontiers in Energy* **2017,** *11* (3), 268-285.

Chapter 3 PtM (M: Fe, Co, Ni) alloys as the ORR electrocatalysts with the facile operating conditions

3.1 Introduction

In the background, we discussed different types of fuel cells, and we pointed out that the key problem is to develop an effective catalyst for ORR. The Pt-based alloys as the most promising cathode catalyst show an excellent electrocatalytic activity for oxygen reduction reaction (ORR) [1-10]. However, there are three questions need to be solved before it is applicated in practice. Firstly, Pt is one of the lowest natural abundances in the world, according to the book: Geological environments of the platinum group elements (Hulbert, L J). And except the rare, it is very difficult to mine due to it scattered all over the world [2-7]. Secondly, many papers showed that Pt nanoparticles would be solvent in acid or base solution under the higher over-potential, which is also the main reason for the insufficient durability [5-8]. Thirdly, scientists prepared different morphology Pt nanoparticles such as a cube, dodecahedron. However, it still cannot prevent dissolving with bringing in a new question: aggregation [9-11]. How to solve these questions attracted many scientists to pay attention to, because Pt-based catalyst has the irreplaceable advantages, such as the most effective pathways (4-electron pathway) in the reaction and the highest electrocatalytic activity [12].

As explained before, the most effective method is that Pt alloys with other transition metals (such as Fe, Co, Ni, Cu, etc.) [13-26]. The main mechanism of the Pt-based alloy is also investigated [13-18]. In brief, the alloy changes the Pt-Pt bonds distance to increase the Pt active surface and weaken the adsorption of the oxygen-containing species, because of the transition metal dissolution, negative shifting or changing the *d*-band center, and vacancies, proved by the calculations and experiments [12-18]. Fe, Co, and Ni are the most investigated transition metals, due to their cheap, abundant, and suitable binding energy with oxygen [15-17, 27-30]. For Pt-based catalysts, several groups confirmed that the catalytic activity relay on their morphology and size of the PtM nanoparticles [31-37], suggesting the exposed crystal facet and surface area have an effect on the electrocatalytic activity [38-40].

Herein, we introduced a facile method to synthesize a serial of 2-D hexagonal nanoplates PtM (M: Fe, Co, Ni) catalysts. With the help of XPS, XRD, EDS, and TEM, the PtFe sample shows a well-defined homogeneous hexagonal nanoplates structure, and ultra-small particle size (ca. 2.6 nm). After the electrochemical measurements and analyses, such as CV, LSV, EIS, K-L equation, and Tafel curves, the PtFe sample displays a superior electrocatalytic activity and stability.

3.2 Experimental

3.2.1 Synthesis of the PtM (M: Fe, Co, Ni) catalysts

The PtM (M: Fe, Co, Ni) catalysts were prepared by the following method: 10 mL of formic acid stirred with 0.015 mmol of chloride metal for 1 h to form the core solution. Then, the mixed solution of 1.5 mL of 0.2 mmol/L $H_2PtCl_6 \cdot 6H_2O$ and 13.5 mL of distilled water slowly drop into the core solution, corresponding to 0.585 mg_{Pt}. At last, in order to reduce the Pt, 1.22 g formic acid and 0.018g XC-72 were mixed into the solution, acted as the reductant and support. After stirring for 24 hours, the filtered products washed with distilled water several times, the catalysts were obtained after dried in an open oven at 60°C (see the Scheme 1).

Scheme 1. Synthesis of the PtFe alloy followed by the soft chemistry method.

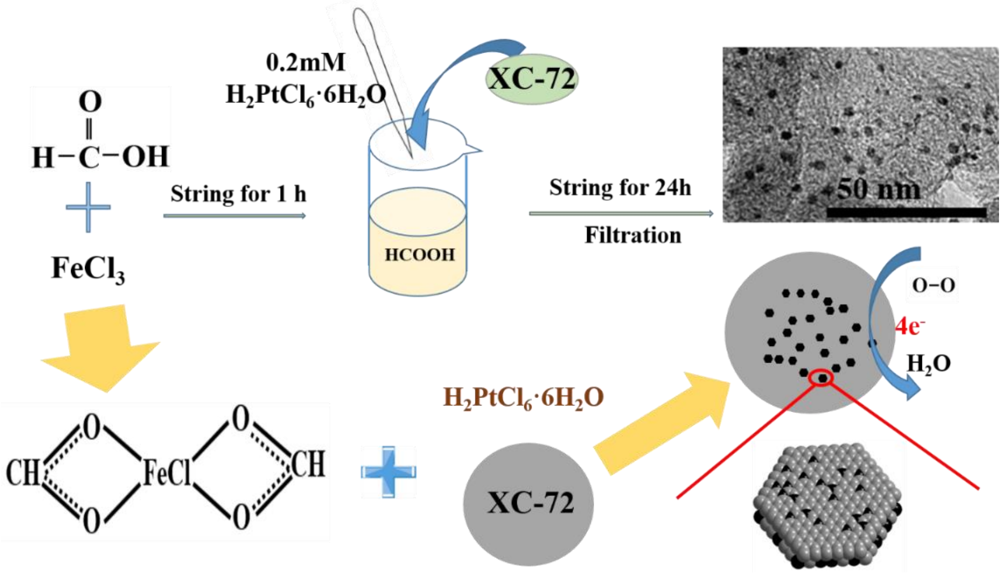

3.2.2 Physical characterizations

The crystalline was confirmed by powder X-ray diffraction (XRD) with the scanning step of 5° min^{-1} from 10° to 70°. The transmission electron microscopy (TEM) and TEM-EDS (Tecnai G2 F20 S-TWIN) were used to analyze the catalyst's morphology and microstructure. In order to display the surface state of the catalyst, X-ray photoelectron spectroscopy (XPS, Thermo Escalab 250Xi) was recorded.

3.2.3 Electrochemical measurements

A typical three-electrode system with a rotating disk electrode (RDE) setup from Pine Instrument Company connected to a CHI 760E electrochemistry workstation was used to explain the catalytic activity of the catalysts. As introduced in Chapter 2, 6 mg of the catalyst with the mixture solution: Nafion solution (5 wt%, 0.1 mL), distilled water (0.15 mL), and IPA (0.25 mL) were ultrasonic for about 0.5 hours to form the catalytic ink. Then 8 μL of the ink was then transferred to the GC electrode with a loading amount of 489 μg cm^{-2} (corresponding to a 3.48 $\mu g_{Pt}/cm^2$, thus no loss in the experiment process). At the same time, the commercial Pt/C was used as a comparison with the loading amount of 20.41 $\mu g_{Pt}/cm^2$ and 3.48 $\mu g_{Pt}/cm^2$. The N_2 or O_2–saturated 0.1 M KOH or $HClO_4$ solution was used as the electrolyte.

The electrochemical impedance spectroscopy (EIS) measurement was recorded to illustrate the effect of electrochemical reaction on interface impedance in a frequency range of 100 kHz to 1 Hz in the alkaline and acidic medium at open circuit voltage. Koutecky–Levich (K–L) equation was used to analyze the kinetic process of the samples. For the Tafel plot, the kinetic current was calculated from the mass transport correction of the LSV curve by the following equation:

$$J_K= (J\times J_L)/ (J_L-J)$$

In the equation, J is the measured current density on the GC disk, and J_K and J_L are the kinetic and diffusion of the limited current densities, respectively.

3.3 Results and discussion

3.3.1 XRD results

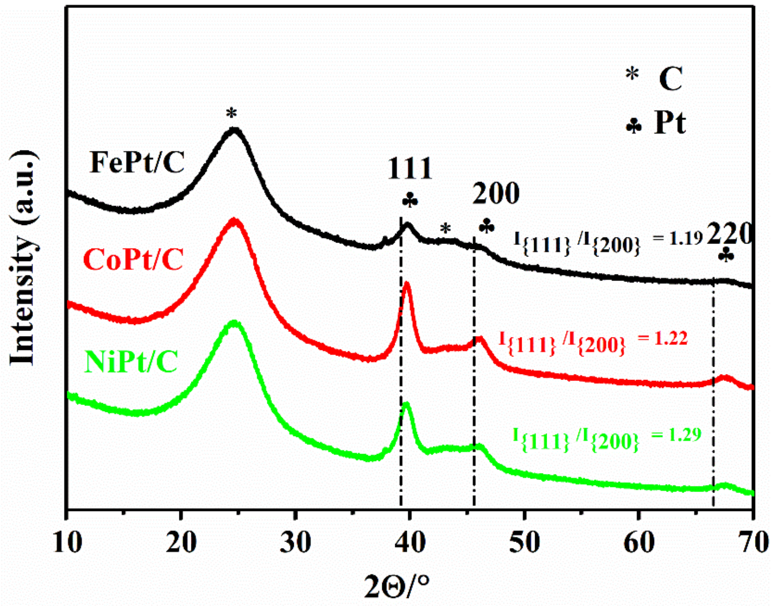

Figure 3.1 The XRD patterns of PtM (M: Fe, Co, Ni) detected from 10 ° to 70°.

Figure 3.1 is the XRD pattern of PtM (M: Fe, Co, Ni) catalysts. There are two broad peaks at ca. 25° and 43°, belonged to (002) and (100) crystalline plane of the support XC-72 (ICDD No. 00-001-0640). There are three weak and sharp peaks in the XRD pattern, corresponding to (111), (200), and (220) planes of the cubic (fcc) polycrystalline Pt (ICDD No. 01-088-2343). The peaks of pure transition metal and chloride cannot be detected by the X-rays, due to the water washing. Compared with the standard Pt pattern (39.27°), about 0.47°, 0.40° and 0.32° positive shift for PtM (M: Fe, Co, Ni), respectively. It is believed that the crystal parameter of Pt is changed, suggesting M atoms were incorporated into the Pt structure to become PtM (M: Fe, Co, Ni) bio-metals. In order to explore the exposed crystal plane, we calculate the ratio of the two main peaks (111) and (200), which is about 1.19 times larger than the normal digital 1.07 from the PDF card [39]. It verifies that the preferential growth direction is the (111). In addition, according to the reports, the (111) and (100) facets would enclose the final exposed plane of Pt nanocrystal, confirming that the exposed plane is (111) and (200) [41].

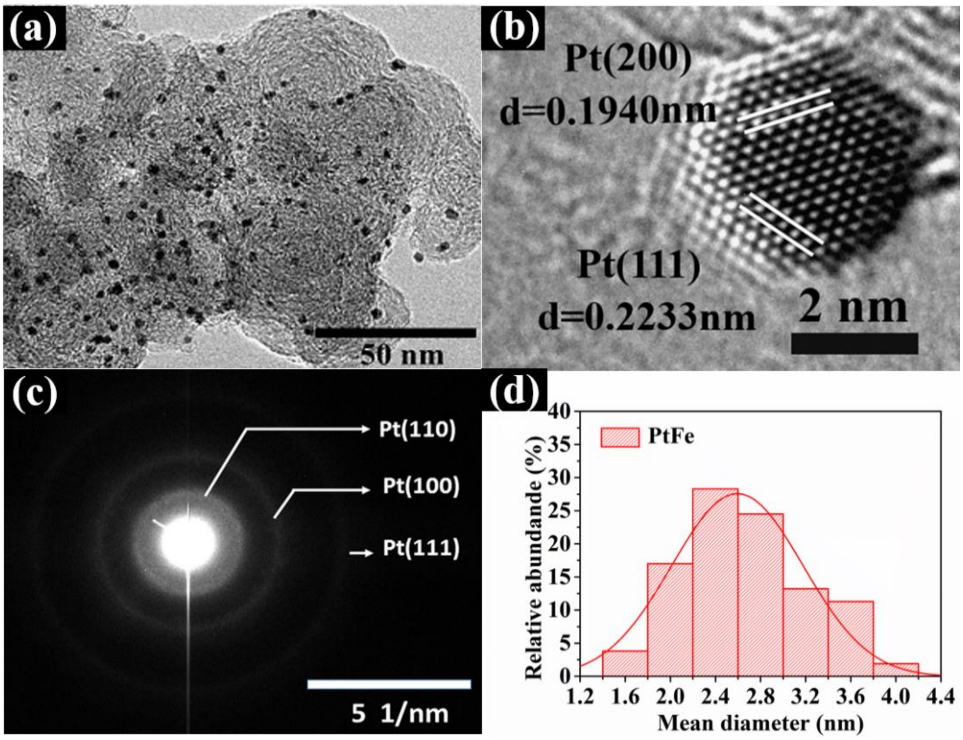

Figure 3.2 The TEM images of the PtFe alloy (a); The high-resolution TEM micrograph (b) and the selected area electron diffraction (c) of the PtFe alloy nanoparticles; The average size analysis of the PtFe alloy nanoparticles (d).

3.3.2 TEM and TEM-EDS results

Transmission electron microscopic (TEM) was used to illustrate the morphology and microstructure of the PtFe alloy catalyst, showing in Figure 3.2 a. The PtFe nanoplates were evenly dispersed on the XC-72 support with the particle size between 1.0-5.0 nm, and the average size is 2.6 ± 0.5 nm after mathematical statistics (figure 3.2d). Figure 3.2 b is the high-resolution TEM micrograph showing the crystal lattice spaces 0.1940 and 0.2233 nm for (111) and (100) directions, respectively.

However, the lattice space is lower than the standard lattice parameter of Pt (200) (0.1985 nm) and (111) (0.2292 nm). The selected area electron diffraction (SAED) shows in the Figure 3c, the unclear diffraction fringes suggest that the PtFe alloy is polycrystalline, corresponding to the {110}, {100} and {111} facet of a platinum crystal.

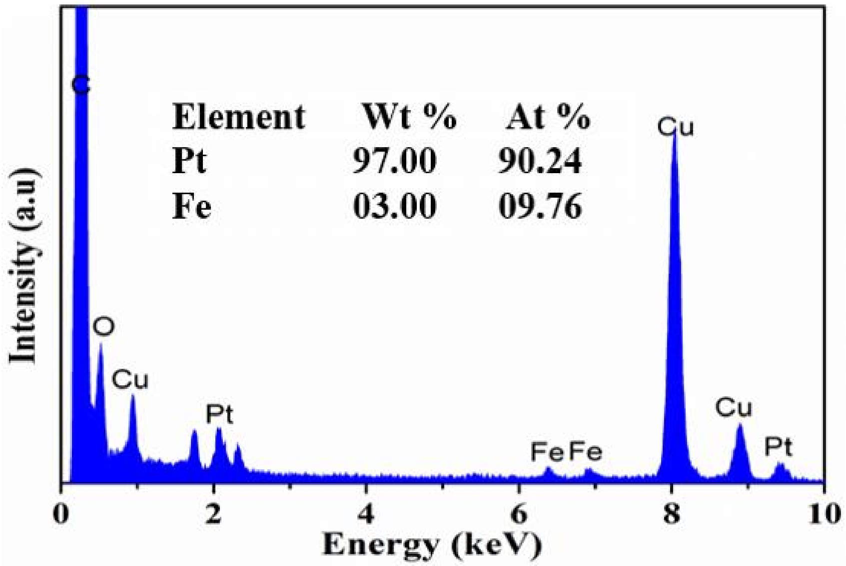

Figure 3.3 TEM-EDS analysis of the PtFe alloy catalyst prepared by the soft chemistry method and the detail ratio of Pt and Fe is in the inset.

Transmission electron microscopic-energy dispersive spectrometer (TEM-EDS) images of the PtFe sample was used to explore the atom ratio of platinum and iron, estimated to be 90.24: 9.76 (Figure 3.3). In the same time, we also estimate the quantities ratio of platinum and iron, which is ca. 97: 3. The TEM-EDS results show that the iron is doped into the Pt nanoplates. The detected iron content is very different from the starting materials after the reduced and filtered, suggesting that partial of Fe ions were reduced or lost in the experiment.

3.3.3 XPS results

The surface states of the sample for different elements were detected by XPS. There are three obvious peaks located at 75, 284.3, and 533 eV, belonging to the signals of C 1s, Pt 4f, and O 2p, respectively (Figure 3.4). The high-resolution of Pt 4f has two peaks $4f_{7/2}$ and $4f_{5/2}$, which can be further split into four peaks 71.4, 74.8 and 72, 75.7 eV, corresponding to the different oxide states of platinum: Pt^0 and Pt^{2+} species. The fraction of each surface oxygen groups was obtained by deconvolution of the O 1s peak in three components, double oxygen bond in C=O (peak at 531.8 eV), hydroxyl and other groups (533 eV), and the oxygen atoms in acid carboxyl groups (534.3 eV). Generally, the elements only less than 20 Å from the surface can be detected by the XPS instrument, due to the intensity of X-ray decreased with the increasing depth. So in the PtFe alloy sample, only the Fe atoms close to the surface (several atomic layers) can be detected [31, 32].

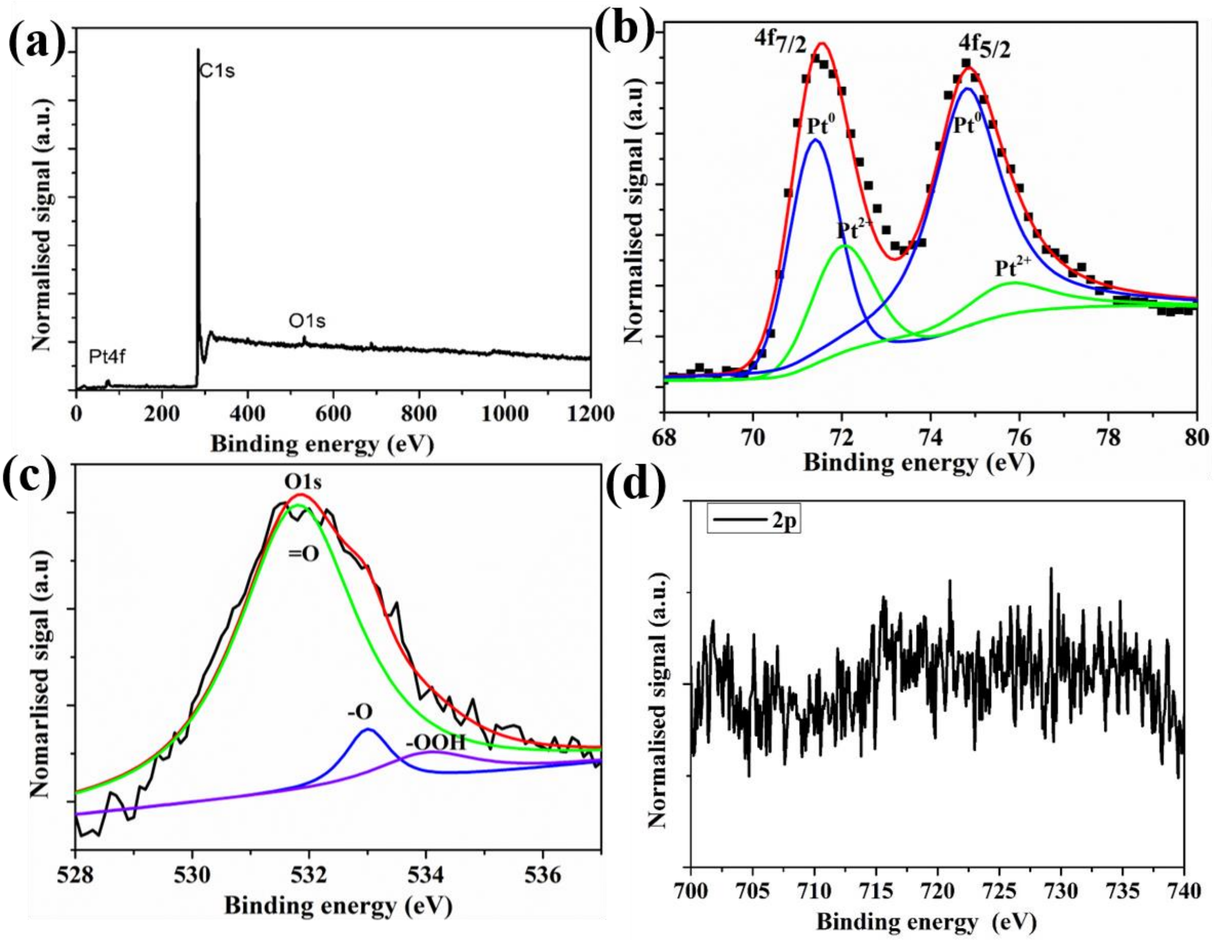

Figure 3.4 The full XPS survey for the as-prepared sample the PtFe alloy (a), Pt 4f (b), O 1s (c) and Fe 2p (d).

3.3.4 Electrochemical characterizations and discussion

The ORR catalytic activity of catalysts in the alkaline medium is shown in Figure 3.5. The cyclic voltammetry (CV) measurement is in the N_2 and O_2-saturated 0.1 M KOH with the scan rate of 10 mV/s. In the low onset potential, one pair of the peak can be observed corresponding to desorption and adsorption of hydrogen (Figure 3.5a). Except that, no peak in the high potential but a broad weak anode peak at the 0.3 V in the N_2-saturated electrolyte, which is the hydrogen oxidation peak. What the significant difference, a sharper and higher reduction peak was observed in the O_2-saturated electrolyte at 0.91 V vs. RHE, indicating a superior ORR catalytic activity. The PtCo and PtNi show the same behavior, but the lower positive shift than the PtFe sample, indicating the potential catalytic activity.

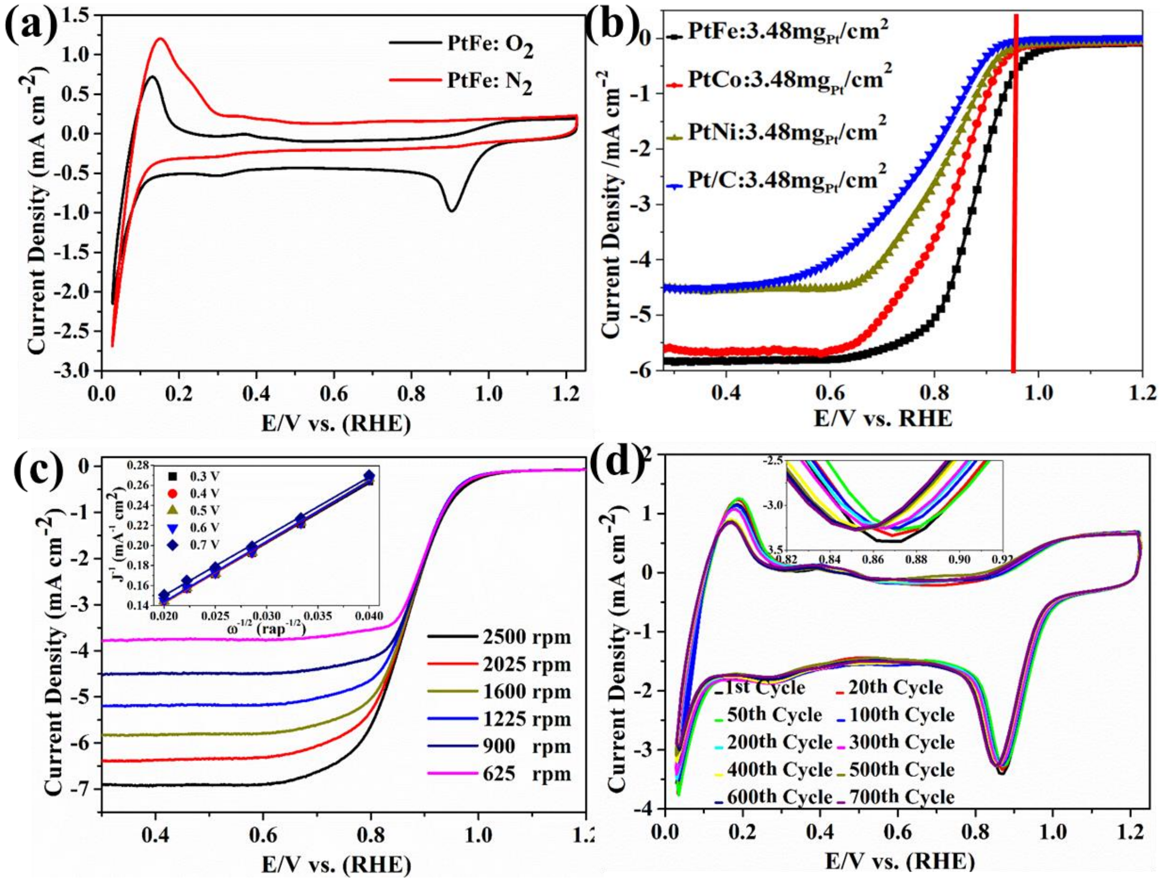

Figure 3.5 CV curves of the PtFe alloy in nitrogen and oxygen–saturated solutions (a). LSV curves in oxygen–saturated solutions at 1600 rpm for three samples and commercial Pt/C (b). LSV curves of the PtFe alloy at different rotation speeds and with a scan rate of 10mV s^{-1} (c). The K-L plots for the PtFe alloy at different potentials shown inset of (c); Electrochemistry stability of the PtFe alloy accessed by CV curves at a scan rate of 50 mV s^{-1} (d). The entire test is in the 0.1 M KOH medium.

Linear sweep voltammetry (LSV) was used to illustrate the catalytic properties of PtM (M: Fe, Co, Ni) catalysts. Figure 3.5b shows that the PtFe alloy sample has the more positive inflection point in the low current density. The highest onset-potential of 0.95 V vs. RHE than other two samples, means that the highest onset-potential than other two samples even the same as to the commercial Pt/C (20.41 $\mu g_{Pt}/cm^2$). Deeper analysis is made to prove that the PtFe alloy is a good electrocatalyst, such as half-wave potentials and limiting current density shown in Table 3.1. As we known, the electrocatalytic activity of Pt-based alloy is controlled by the transition metals, but there is no consensus about the key point because of many reasons, such as morphology, dissolution, and their native properties. Recently, theoretical calculation found that the onset-potential of Pt-based alloy relay on the thermodynamic dissolution potential of the transition metals at pH=0 [42], which obey the inverse proportion. In the Figure 3.5b, the comparison of PtM (M: Fe, Co, Ni) and the commercial Pt/C with the same Pt loading amount is investigated. Clearly, the Pt/C (3.48 $\mu g_{Pt}/cm^2$) shows the lower onset-potential and the limited current. In detail, the PtFe catalyst displays about 11.43 times of the Pt/C (3.48 $\mu g_{Pt}/cm^2$) for onset-potential at 0.9 V, indicating the excellent ORR catalytic activity.

The kinetics of the catalysts PtM (M: Fe, Co, Ni) was performed by the Koutecky–Levich (K–L) analysis, which is from LSV curves at different rotation speeds with the scan rate of 10 mV/s. From the inset of Figure 3.5c, the electron transfer number of the PtFe alloy sample is from 3.73 to 3.85 at the potential range of 0.3-0.7 V, suggesting the ORR process of the PtFe alloy is the four-electron pathway. In addition, the samples of PtCo and PtNi are calculated by the K-L equation, which is close to four at different potentials, indicating the ORR process is the effective four-electron pathway.

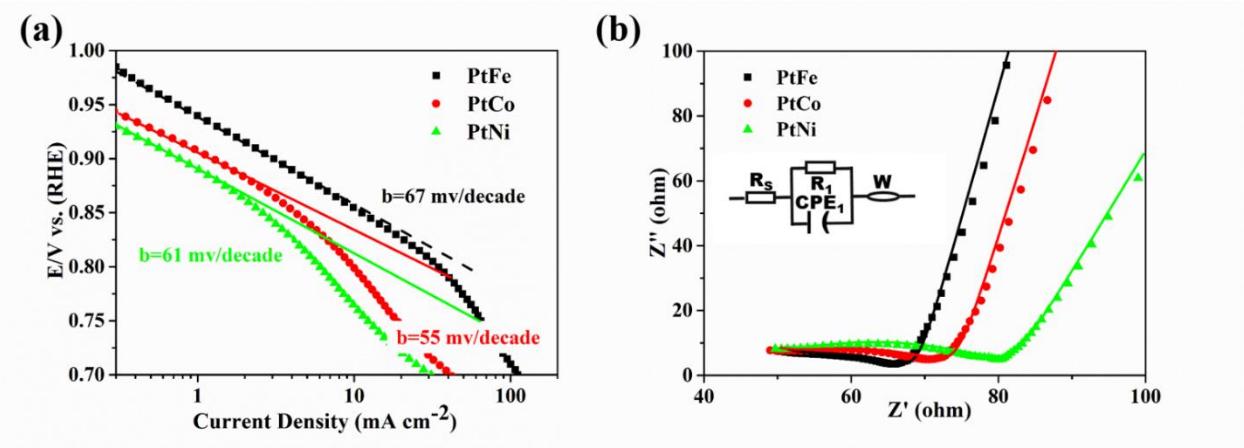

Figure 3.6 The corresponding Tafel plots from LSV curves at 1600 rpm of PtM (M: Fe, Co, Ni) (a); The impedance spectra of three samples at open circles potential, and the line is the fitting results (b). The entire test is in the 0.1 M KOH medium.

The superior catalytic activity and good stability are essential for one excellent catalyst. The CV curve measurements of the PtFe alloy is from 0.02 to 1.21 V for 700 cycles with the scan rate of 50 mV/s to explore their stability, as shown in Figure 3.5d. In the CV curves, there are two factors to measure the stability: the electrochemically-active surface area (ECSA) and the cathode peak. ECSA was used to prove the active area decreasing with the active sites. The cathode peak would negatively shift due to the active sites dissolved or aggregated. There is an obvious negative shift for the cathode peak and decrease of the ECSA before 400 circles, due to the dissolution or corrosion of unstable products and the decrease of the surface area. None clearly changes were observed after 400 circles (inset of Figure 3.5d), both the surface area and the cathode peak, suggesting the high stability.

The Tafel slope was used to further explore the kinetic process of the catalysts. In the previous paper, the standard Tafel slope of platinum is close to 60 mV per decade, as discussed in Chapter 2. However, the measurements of platinum are different from the theoretical value, due to the condition and measurement error. In this chapter, we find the Tafel slope of the PtFe alloy is 67 mV/dec, and the PtCo and PtNi is about 55 and 61 mV/dec, which is close to the 65 mV/dec of Pt, indicating that the ORR process is controlled by the first transfer electron step (Figure 3.6a).

Table 3.1. The ORR performance of different catalysts in alkaline medium

Samples	**PtFe**	**PtCo**	**PtNi**	**Pt/C (20.4μg$_{Pt}$/cm^2)**	**Pt/C (3.48μg$_{Pt}$/cm^2)**
Onset potential (V)	0.95	0.94	0.93	0.97	0.90
Half wave potential (V)	0.88	0.83	0.82	0.86	0.78
Diffusion limiting current (mA/cm^2)	5.83	5.66	4.55	5.67	4.40
Electron transfer number at 0.5V	3.73	3.59	2.93	4.00	4.00

The electronic impedance spectroscopy (EIS) was used to calculate the surface resistance in the electrochemical reaction. It is known that lower resistance is beneficial to electron transfer. Figure 3.6b is the EIS spectra of PtM (M: Fe, Co, Ni), and the schematic illustration for the equivalent circuit is shown in the inset of Figure 3.6 b. R_S is the same for the three samples ca. 15 ohms, suggesting that R_1 is the system resistance. We believe R_2 represents the surface resistance in the electrochemical reaction, which is about 22.48, 27.72 and 29.50 ohms for PtM (M: Fe, Co, Ni), respectively. As discussed before, the suitable resistance value has advantages to improve the reaction, suggesting the excellent electron transfer ability [43, 44]. In order to make the connection between the resistance and the catalytic activity, we input the resistance combined with the half-wave potential (Figure 3.7a), the limited current (Figure 3.7b) and the onset potential (Figure 3.7c) from the LSV data on the coordinate map.

The inverse line relationship shows that the catalyst for the lower resistance has the higher electrochemical activity [17].

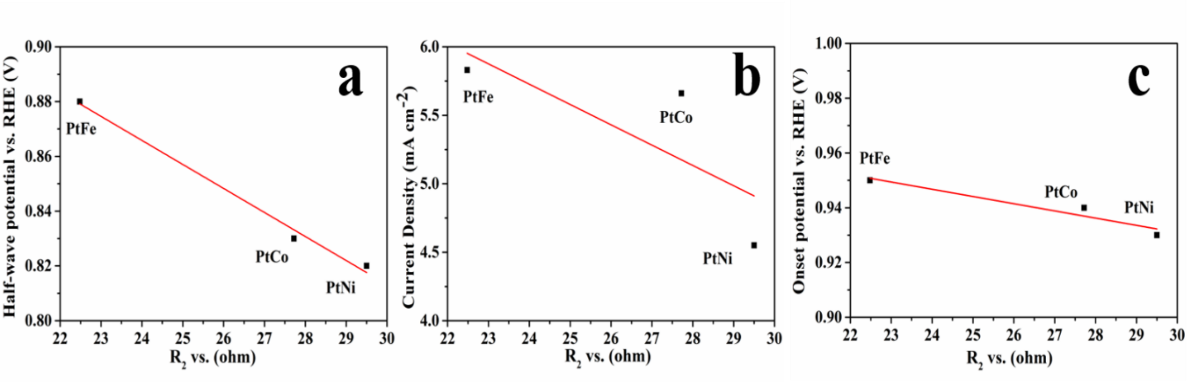

Figure 3.7 The correlation of the half-wave potential (a), the limited current (b) and onset potential (c) from the LSV data and the resistance, the red line is the simulated line.

The electrochemical measurements including CV, LSV, EIS, K-L, and Tafel slope indicate that the PtFe alloy is an excellent ORR catalyst in the 0.1 M KOH solution. We also explored the activity of PtM (M: Fe, Co, Ni) in the acidic solution, as shown in Figure 3.8. The rectangular shape of CV curve appeared in the nitrogen-saturated acidic electrolyte. In the oxygen-saturated solution, a prominent oxygen reduction peak comes out at 0.72 V *vs.* RHE (Figure 3.8a). Interestingly, for the three samples, the PtFe alloy shows the most positive potential and the sharpest peak, suggesting the highest ORR catalytic activity. Linear sweep voltammetry (LSV) was used to illustrate the catalytic properties of PtM (M: Fe, Co, Ni) catalysts. Figure 3.8b shows that the PtFe alloy sample has the more positive inflection point in the low current density. The highest onset-potential of 0.75 V vs. RHE than other two samples, meaning that the highest onset-potential than other two samples even the same as to the commercial Pt/C (20.41 $\mu g_{Pt}/cm^2$). Deeper analysis is made to prove that the PtFe alloy is a good electrocatalyst, such as half-wave potentials and limiting current density shown in Table 3.2. As we know, the electrocatalytic activity of Pt-based alloy is controlled by the transition metals, which is discussed in the previous. In the Figure 3.7b, the comparison of PtM (M: Fe, Co, Ni) and the commercial Pt/C with the same Pt loading amount have been investigated. Clearly, the Pt/C (3.48 $\mu g_{Pt}/cm^2$) shows the lower onset-potential and the limited current. In detail, the PtFe catalyst displays about 18.53 times of the Pt/C (3.48 $\mu g_{Pt}/cm^2$) for the limited current at 0.7 V, indicating the excellent ORR catalytic activity.

At the same time, we founded the K-L simulated to calculate the electron transfer number. From the inset of Figure 3.8c, six parallel lines indicate the stable ORR process for different potentials, estimated from 3.79 to 4.26, suggesting that four-electron pathway is dominated. The other two samples of PtCo and PtNi alloy are calculated ca. 4, the detail shown in Table 3.2. The K-L simulated line implies all the samples follow the effective electron transfer pathway on the electrochemical reaction.

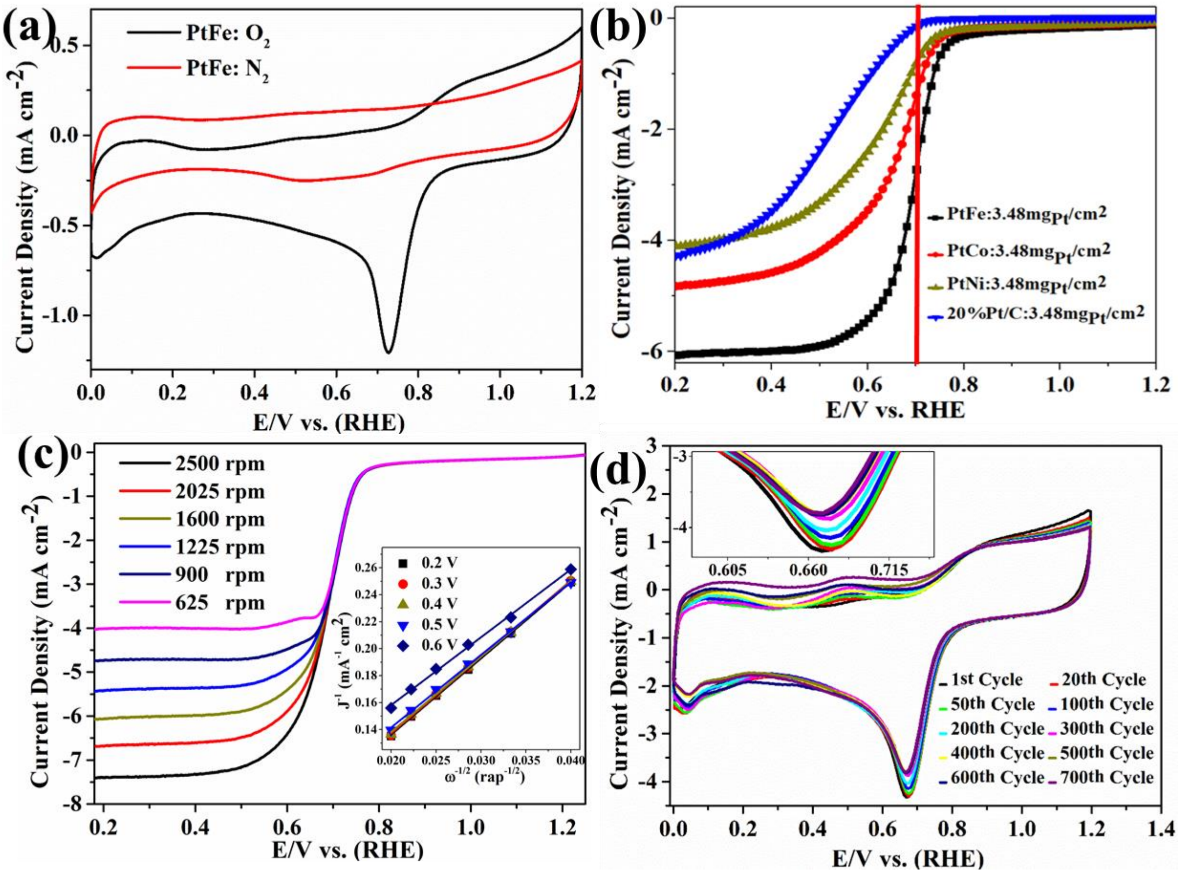

Figure 3.8 CV curves of the PtFe alloy in nitrogen and oxygen–saturated solutions (a). LSV curves in oxygen–saturated solutions at 1600 rpm for three samples and commercial Pt/C (b). LSV curves of the PtFe alloy at different rotation speeds and with a scan rate of 10mV s^{-1} (c). The K-L plots for the PtFe alloy at different potentials shown inset of (c); Electrochemistry stability of the PtFe alloy accessed by CV curves at a scan rate of 50 mV s^{-1} (d). The entire test is in the 0.1 M $HClO_4$ medium.

Similar to the investigation in the alkaline solution, the CV curve measurements of the PtFe alloy is also from 0.02 and 1.21 V for 700 cycles with the scan rate of 50 mV/s to explore its stability, as shown in Figure 3.8d. As introduced in Section 2.3.1, the cathode peak decreased by ca. 20 mV and 0.45 mA/cm^2 due to the dissolved or aggregate of the PtFe nanoplates.

However, no obvious difference can be observed after 400 circles, indicating its high stability.

The Tafel slope was carried on to further explore the kinetic process of the catalysts. As we know, the standard Tafel slope of platinum is about 60 mV per decade. In this part, we estimated the Tafel slope of the PtFe alloy is 62 mV/dec. The PtCo and PtNi alloys are about 71 and 93 mV/dec, indicating that their ORR process is controlled by the first transfer electron step (Figure 3.9a). The detailed data is shown in Table 3.2.

EIS was carried on calculating the surface resistance in the electrochemical reaction. As discussed in the previous, the lower resistance is beneficial to electron transfer. Figure 3.9b is the EIS spectra of PtM (M: Fe, Co, Ni) alloys, and the schematic illustration for the equivalent circuit is shown in the inset of Figure 3.6. R_S shows the same value for the three samples, which is about 14 ohms, suggesting that R_S is the system or electrolyte resistance. Moreover, R_2 is about 46.37, 192.2 and 317.2 ohms for PtM (M: Fe, Co, Ni), respectively. It is popular that the suitable resistance value has advantages to improve the reaction, due to the excellent electron transfer ability. In order to make the connection between the resistance and the catalytic activity, we input the resistance combined with the half-wave potential (Figure 3.10 a), the limited current (Figure 3.10 b) and the onset potential (Figure 3.10c) from the LSV data on the coordinate map [43, 44]. The inverse line relationship shows that the catalyst with the lower resistance has the higher electrochemical activity [17].

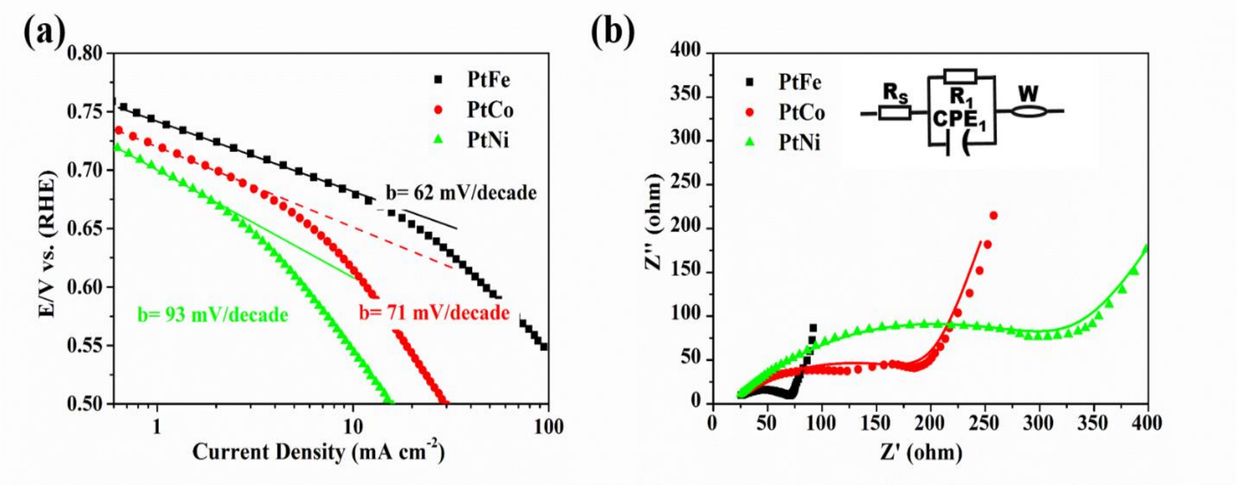

Figure 3.9 The corresponding Tafel plots from LSV curves at 1600 rpm of PtM (M: Fe, Co, Ni) (a); The impedance spectra of three samples at open circles potential, and the line is the fitting results (b). The entire test is in the 0.1 M $HClO_4$ medium.

Table 3.2. The ORR performance of different catalysts in acidic medium

Samples	**PtFe**	**PtCo**	**PtNi**	**Pt/C**	**Pt/C**
				(20.4μg$_{Pt}$/cm^2)	**(3.48μg$_{Pt}$/cm^2)**
Onset potential (V)	0.75	0.74	0.73	0.75	0.69
Half wave potential (V)	0.70	0.67	0.63	0.67	0.52
Diffusion limiting current (mA/cm^2)	6.06	4.82	4.10	5.15	4.30
Electron transfer number at 0.5V	3.84	3.88	4.61	4.00	4.00

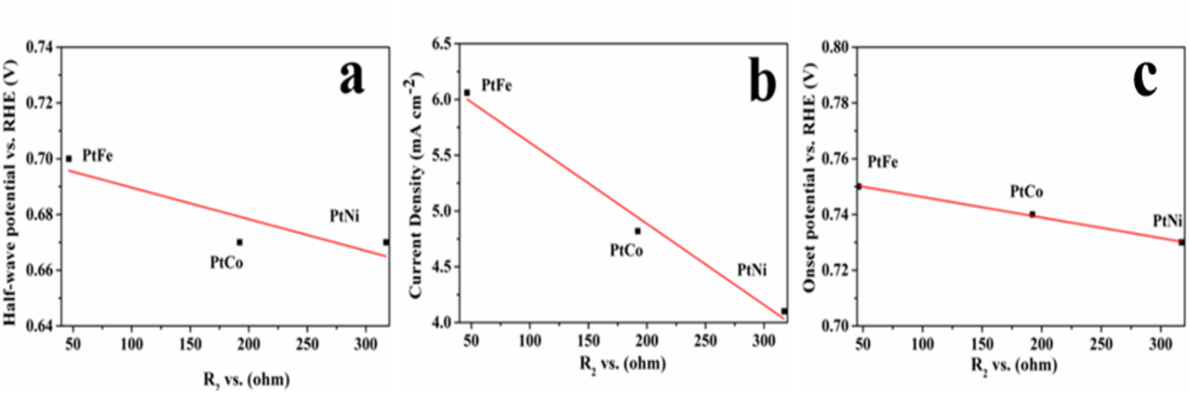

Figure 3.10 The correlation of the half-wave potential (a), the limited current (b) and the onset potential (c) from the LSV data and the resistance, the red line is the simulated line.

In short, after the various electrochemical measurements, we believe the PtFe alloy is the best ORR catalyst in the samples with the excellent catalytic activity and stability, implying a promising candidate to replace the Pt/C. The physical characterize shows Fe atoms doped into the Pt nanoparticle. The Pt crystal lattice was confined to promote the electron transfer and the weak strain of crystal lattice would prevent the Pt dissolved at the high over-potential. In another factor, the raw precursor transition metal salt has effects on the catalytic activity. Scientists indicate the chloride iron would form the stable polymeric $FeCl(OOCH)_2 \cdot H_2O$ with the formic acid at room temperature, and the Fe^{3+} would be reduced in the over formic acid. At the same time, several groups proved that formic acid would promote the electrochemical activity during the reaction, due to the low over-potential and decrease the accumulation of intermediates on the catalyst surface [34-36].

As we know, the transition metals affect the catalytic activity of Pt-based alloy [45]. Although, there is no consensus for that range. It is no questioning that Pt-based alloy follows the effective 4-electron pathway process with the Griffiths- or Bridged-type adsorptions [31, 46]. The transition metal doping would increase the vacancies of the Pt surface and shorten the Pt-Pt bond distance, due to the electron structure of transition metals. The exposed crystalline facet is the effective (111) plane, which is discussed in Chapter 1. At last, the average nanoparticles would support more active sites to promote ORR process.

3.4 Conclusions

In conclusion, PtM (M: Fe, Co, Ni) alloys were prepared by a simple method and used as the ORR catalysts. The physical characterization shows that the small particles are evenly distributed, which contributes to the catalytic activity. In addition, the Fe atoms doped into the Pt crystal would change the distance of Pt-Pt bonds to suitable for adsorption and desorption of oxygen. Finally, the PtFe alloy used as the ORR catalyst possesses the best electrocatalytic activity in terms of the onset-potential and stability. Advanced electrochemistry analyses indicate that the PtFe alloy exhibits the best activity and superior electrochemical stability both in acid and base media, which has a great potential for replacing the Pt/C as an ORR catalyst for fuel cells.

3.5 References

[1] Shao, M.; Chang, Q.; Dodelet, J.- P.; Chenitz, R. Recent advances in electrocatalysts for oxygen reduction reaction. *Chemical Reviews* **2016**, *116*(6), 3594-3657.

[2] Jalan, V. M.; Landsman, D. A.; Lee, J. M. Electrochemical cell electrodes incorporating noble metal-base metal alloy catalysts. U.S. Patent 4,192,907, 1980.

[3] Stephens, I. E. I.; Bondarenko, A. S.; Gronbjerg, U.; Rossmeisl, J.; Chorkendorff, I. Understanding the electrocatalysis of oxygen reduction on platinum and its alloys. *Energy & Environmental Science* **2012**, *5*, 6744-6762.

[4] Yang, H. Platinum–based electrocatalysts with core–shell nanostructures. *Angewandte Chemie International Edition* **2011,** *50*(12), 2674-2676.

[5] Kim, J. H.; Fang, B.; Kim, M. S.; Yoon, S. B.; Bae, T. S.; Ranade, D. R.; Yu, J. S. Facile synthesis of bimodal porous silica and multimodal porous carbon as an anode catalyst support in proton exchange membrane fuel cell. *Electrochimica Acta* **2010**, *55*(26), 7628-7633.

[6] Wang, Y. J.; Wilkinson, D. P.; Guest, A.; Neburchilov, V.; Baker, R.; Nan, F.; Botton, G. A.; Zhang, J. Synthesis of Pd and Nb–doped TiO_2 composite supports and their corresponding Pt–Pd alloy catalysts by a two-step procedure for the oxygen reduction reaction. *Journal of Power Sources* **2013**, *221*(1), 232-241.

[7] Balgis, R.; Widiyastuti, W.; Ogi, T.; Okuyama, K. Enhanced electrocatalytic activity of Pt/3D hierarchical bimodal macroporous carbon nanospheres. *ACS Applied Materials &Interfaces* **2017**, *9*(28), 23792-23799.

[8] Escudero-Escribano, M.; Malacrida, P.; Hansen, M. H.; Vej-Hansen, U. G.; Velázquez-Palenzuela, A.; Tripkovic, V.; Schiøtz, J.; Rossmeisl, J.; Stephens, I. E. L.; Chorkendorff, I. Tuning the activity of Pt alloy electrocatalysts by means of the lanthanide contraction. *Science* **2016**, *352*(6281), 73-76.

[9] Fu, T.; Fang, J.; Wang, C.; Zhao, J. Hollow porous nanoparticles with Pt skin on an Ag-Pt alloy structure as a highly active electrocatalyst for the oxygen reduction reaction. *Journal of Materials Chemistry A* **2016**, *4*, 8803-8811.

[10] Antolini, E. Platinum-based ternary catalysts for low-temperature fuel cells: part I. Preparation methods and structural characteristics. *Applied Catalysis B: Environmental* **2007**, *74*, 324-336.

[11] Coleman, E. J.; Chowdhury, M. H.; Co, A. C. Insights into the oxygen reduction reaction activity of Pt/C and PtCu/C catalysts. *ACS Catalysis* **2015**, *5*, 1245-1253.

[12] Stephens, I. E.; Bondarenko, A. S.; Grønbjerg, U.; Rossmeisl, J.; Chorkendorff, I. Understanding the electrocatalysis of oxygen reduction on platinum and its alloys. *Energy & Environmental Science* **2012**, *5*, 6744-6762.

[13] Sahin, N. E.; Napporn, T. W.; Dubau, L.; Kadirgan, F.; Léger, J. M.; Kokoh, K. B. Temperature-dependence of oxygen reduction activity on Pt/C and PtCr/C electrocatalysts synthesized from microwave-heated diethylene glycol method. *Applied Catalysis B: Environmental* **2017**, *203*, 72-84.

[14] Ammam, M.; Easton, E. B. Oxygen reduction activity of binary PtMn/C, ternary PtMnX/C (X= Fe, Co, Ni, Cu, Mo and, Sn) and quaternary PtMnCuX/C (X= Fe, Co, Ni, and Sn) and PtMnMoX/C (X= Fe, Co, Ni, Cu and Sn) alloy catalysts. *Journal of Power Sources* **2013**, *236*, 311-320.

[15] Du, X. X.; He, Y.; Wang, X. X.; Wang, J. N. Fine-grained and fully ordered intermetallic PtFe catalysts with largely enhanced catalytic activity and durability. *Energy & Environmental Science* **2016**, *9*, 2623-2632.

[16] Lin, S. P.; Wang, K. W.; Liu, C. W.; Chen, H. S.; Wang, J. H. Trends of oxygen reduction reaction on platinum alloys: a computational and experimental study. *The Journal of Physical Chemistry C* **2015**, *119*, 15224-15231.

[17] Wang, P.; Yin, S.; Wen, Y.; Tian, Z.; Wang, N.; Key, J.; Shen, P. K. Ternary Pt_9RhFe_x nanoscale alloys as highly efficient catalysts with enhanced activity and excellent CO-Poisoning tolerance for ethanol oxidation. *ACS Applied Materials & Interfaces* **2017**, *9*, 9584-9591.

[18] El-Deeb, H.; Bron, M. Microwave-assisted polyol synthesis of PtCu/carbon nanotube catalysts for electrocatalytic oxygen reduction. *Journal of Power Sources* **2015**, *275*, 893-900.

[19] Hassan, A.; Carreras, A.; Trincavelli, J.; Ticianelli, E. A. Effect of heat treatment on the activity and stability of carbon supported PtMo alloy electrocatalysts for hydrogen oxidation in proton exchange membrane fuel cells. *Journal of Power Sources* **2014**, *247*, 712-720.

[20] Lim, B.; Jiang, M.; Camargo, P. H.; Cho, E. C.; Tao, J.; Lu, X.; Zhu, Y.; Xia, Y. Pd-Pt bimetallic nanodendrites with high activity for oxygen reduction. *Science* **2009**, *324*, 1302-1305.

[21] Liang, Y. T.; Lin, S. P.; Liu, C. W.; Chung, S. R.; Chen, T. Y.; Wang, J. H.; Wang, K. W. The performance and stability of the oxygen reduction reaction on Pt–M (M= Pd, Ag and Au) nanorods: an experimental and computational study. *Chemical Communications* **2015**, *51*, 6605-6608.

[22] Dorjgotov, A.; Jeon, Y.; Hwang, J.; Ulziidelger, B.; Kim, H. S.; Han, B.; Shul, Y. G. Synthesis of durable small-sized bilayer Au@Pt nanoparticles for high performance PEMFC catalysts. *Electrochimica Acta* **2017**, *228*, 389-397.

[23] Nielsen, J. H.; Hansen, T. W.; Nilsson, A.; Stephens, I. E.; Mass-selected nanoparticles of Pt_xY as model catalysts for oxygen electroreduction. *Nature Chemistry* **2014**, *6*, 732-738.

[24] Johansson, T. P.; Ulrikkeholm, E. T.; Hernandez-Fernandez, P.; Malacrida, P.; Hansen, H. A.; Bandarenka, A. S.; Chorkendorff, I. Pt skin versus Pt skeleton structures of Pt_3Sc as electrocatalysts for oxygen reduction. *Topics in Catalysis* **2014**, *57*, 245-254.

[25] Stephens, I. E.; Bondarenko, A. S.; Bech, L.; Chorkendorff, I. Oxygen electroreduction activity and X-Ray photoelectron spectroscopy of platinum and early transition metal alloys. *ChemCatChem* **2012**, *4*, 341-349.

[26] Yoo, S. J.; Hwang, S. J.; Lee, J. G.; Lee, S. C.; Lim, T. H.; Sung, Y. E.; Wieckowski, A.; Kim, S. K. Promoting effects of La for improved oxygen reduction activity and high stability of Pt on Pt-La alloy electrodes. *Energy & Environmental Science* **2012**, *5*, 7521-7525.

[27] Nguyen, M. T.; Wakabayashi, R. H.; Yang, M.; Abruña, H. D.; DiSalvo, F. J. Synthesis of carbon supported ordered tetragonal pseudo-ternary $Pt_2M'M''$(M= Fe, Co, Ni) nanoparticles and their activity for oxygen reduction reaction. *Journal of Power Sources* **2015**, *280*, 459-466.

[28] Pizzutilo, E.; Knossalla, J.; Geiger, S.; Grote, J. P.; Polymeros, G.; Baldizzone, C.; Mezzavilla, S.; Ledendecker, M.; Mingers, A.; Cherevko, S.; Schu¨h, F.; Mayrhofer K. J. J. The Space Confinement Approach Using Hollow Graphitic Spheres to Unveil Activity and Stability of Pt-Co Nanocatalysts for PEMFC. *Advanced Energy Materials* **2017**, 1700835.

[29] Shi, G.; Yano, H.; Tryk, D. A.; Iiyama, A.; Uchida, H. Highly Active, CO-Tolerant, and Robust Hydrogen Anode Catalysts: Pt-M (M= Fe, Co, Ni) Alloys with Stabilized Pt-Skin Layers. *ACS Catalysis* **2016**, *7*, 267-274.

[30] Bhattacharjee, S.; Yoo, S. J.; Waghmare, U. V.; Lee, S. C. NH_3 adsorption on PtM (Fe, Co, Ni) surfaces: Cooperating effects of charge transfer, magnetic ordering and lattice strain. *Chemical Physics Letters* **2016**, *648*,166-169.

[31] Toda, T.; Igarashi, H.; Uchida, H.; Watanabe, M. Enhancement of the electroreduction of oxygen on Pt alloys with Fe, Ni, and Co. *Journal of The Electrochemical Society* **1999**, *146*, 3750-3756.

[32] Ding, X.; Yin, S.; An, K.; Luo, L.; Shi, N.; Qiang, Y.; Pasupathi, S.; Pollet, B. G.; Shen, P. K. FeN stabilized FeN@Pt core-shell nanostructures for oxygen reduction reaction. *Journal of Materials Chemistry A* **2015**, *3*, 4462-4469.

[33] Stamenkovic, V. R.; Mun, B. S.; Arenz, M.; Mayrhofer, K. J.; Lucas, C. A.; Wang, G.; Ross, P. N.; Markovic, N. M. Trends in electrocatalysis on extended and nanoscale Pt-bimetallic alloy surfaces. *Nature Materials* **2007**, *6*, 241.

[34]Wang, C.; Markovic, N. M.; Stamenkovic, V. R. Advanced platinum alloy electrocatalysts for the oxygen reduction reaction. *ACS Catalysis* **2012**, *2*, 891-898.

[35] Huang, X.; Zhao, Z.; Cao, L.; Chen, Y.; Zhu, E.; Lin, Z.; Li, M.; Yan, A.; Zettl, A.; Wang, Y. M.; Mueller, T.; Huang, Y.; Duan, X. High-performance transition metal–doped Pt_3Ni octahedra for oxygen reduction reaction. *Science* **2015**, *348*, 1230-1234.

[36] Bu, L.; Zhang, N.; Guo, S.; Zhang, X.; Li, J.; Yao, J.; Wu, T.; Lu, G.; Ma, J.; Su, D.; Huang, X. Biaxially strained PtPb/Pt core/shell nanoplate boosts oxygen reduction catalysis. *Science* **2016**, *354*, 1410-1414.

[37] Wang, L.; Tang, Z.; Yan, W.; Wang, Q.; Yang, H.; Chen, S. Co@Pt Core@Shell nanoparticles encapsulated in porous carbon derived from zeolitic imidazolate framework 67 for oxygen electroreduction in alkaline media. *Journal of Power Sources* **2017**, *343*, 458-466.

[38] Paul, R. C.; Baidya, O. B.; Kaur, A. J.; Sharma, R. D.; Kapoor, R. Reactions of iron (II) and iron (III) chlorides with formic acid. *Australian Journal of Chemistry* **1977**, *30*, 1439-1443.

[39] Silva, L. S.; López-Suárez, F. E.; Perez-Cadenas, M.; Santos, S. F.; da Costa, L. P.; Eguiluz, K. I.; Salazar-Banda, G. R. Synthesis and characterization of highly active Pb_x@Pt_y/C core-shell nanoparticles toward glycerol electrooxidation. *Applied Catalysis B: Environmental* **2016**, *198*, 38-48.

[40] Juan, V.; Jose, S.; Enrique, H.; Carlos, M.; Enhanced catalytic activity and stability for the electrooxidation of formic acid on lead modified shape controlled platinum nanoparticles. *Applied Catalysis B: Environmental* **2017**, *201*, 48-57.

[41] Wang, D.; Xin, H.; Hovden, R.; Wang, H.; Yu, Y.; Muller, D.; Disalvo, F.; Abruna, H. Structurally ordered intermetallic platinum–cobalt core–shell nanoparticles with enhanced activity and stability as oxygen reduction electrocatalysts. *Nature Chemistry* **2013**, *12*, 81.

[42] Han, B.; Carlton, C.; Suntivich, J.; Xu, Z.; Yang, S.; Oxygen reduction activity and stability trends of bimetallic $Pt_{0.5}M_{0.5}$ nanoparticle in acid. *JThe Journal of Physical Chemistry C* **2015**, *119*, 3971-3978.

[43] Li, Y.; Zhou, W.; Wang, H.; Xie, L.; Liang, Y.; Wei, F.; Idrobo, J.; Pennycook, S.; Dai, H. An oxygen reduction electrocatalyst based on carbon nanotube-graphene complexes. *Nature Nanotechnology* **2012**, *7*, 394-400.

[44] Li, L.; Dai, P.; Gu, X.; Wang, Y.; Yan, L.; Zhao, X.; High oxygen reduction activity on a metal–organic framework derived carbon combined with high degree of graphitization and pyridinic-*N* dopants. *Journal of Materials Chemistry A* **2017**, *5*, 789-795**.**

[45] Mukerjee, S.; Srinivasan, S.; Soriaga, M. P.; McBreen, J. Role of structural and electronic properties of Pt and Pt alloys on electrocatalysis of oxygen reduction An in situ XANES and EXAFS investigation. *Journal of The Electrochemical Society* **1995**, *142*, 1409-1422.

[46] Yeager, E.; Razaq, M.; Gervasio, D.; Tryk, D.; Structural Effects in Electrocatalysis and Oxygen Electrochemistry. **1992**, *PV 92-11*, 440.

Chapter 4 Temperature-dependence of electrocatalytic activity for dual transition metals embedded in P-doped porous carbon used as ORR catalyst

4.1 Introduction

The overuse of fossil energy leads to greenhouse gases and acid rain. Therefore, how to develop the energy structure with the clean energy is important for environmental protection. Fuel cells as the most promising candidate attract more attention. However, it is limited by the lower working efficiency, due to the slow ORR kinetics in the cathode. The extra catalyst is necessary to improve the ORR process. The most efficient catalyst is platinum particles loading on the high conductivity carbon (XC-72). The high price and scarce of platinum hinder the Pt-based catalysts for large-scale production [1-5]. In addition, the weaknesses of Pt-based catalysts such as poor durability and CO sensitive catalysis in the reaction promote scientists to develop the new efficient, durable, and cheap catalysts.

In decades, many substitutes are investigated: noble metal (Pd, Au, Ru) [5-6], normal transition metal (FeN_4, Co_2P, Co_8S_9) [7-8], and heteroatom atom carbon materials [9]. Among them, heteroatom atom doping carbon materials draw great attention, due to their high catalytic activity and stability. In general, the catalytic reason of heteroatom atoms carbon materials is that the heteroatom atom doping changes the asymmetry of the carbon atomic spin density to increase the adsorption of oxygen [10-11]. Moreover, the active groups are also investigated well, for example, pyridine-like N and graphite-like N show more contribution to the catalytic activity than pyrrole-type N for the N-doped carbon materials [12-13]. However, we still cannot make sure the mechanism and the active groups in the reaction for other heteroatom atoms doped carbon catalysts [14-17]. Recently, Masa’s group found that the trace of transition metal doping would improve ORR process [14]. Too many transition metals were investigated to promote ORR process. Iron and cobalt are the best two because of their natural properties, such as the 3D Fe-N-nanocarbon intercalated graphene catalyst [16]. Further investigation shows that the synergetic effect of different metals is beneficial for the catalytic activity [17-23]. However, the ratios of different metals are not clear even for different heteroatom atoms.

P element is in the same group with nitrogen showing the similar chemical properties [22-24]. Moreover, it attracts more attention than usual after Fe-P-C and Fe-P-Graphene catalysts synthesized [23-24]. Nevertheless, the question is that rare papers about cobalt and iron incorporated in P-doped carbon (FCPA) were published, because of the insurmountable selectivity of phytic acid (abundant the P and C source).

Herein, we synthesized the cobalt and iron incorporated in P-doped porous carbon materials with the traditional solid-state reaction method. We first investigated the synergetic effect of Fe and Co in P-doped porous carbon, confirming the correlation between the catalytic activity and the ratios of transition metals. With different physic measurements such as EDS, XRD, TEM, XPS, and ICP, we confirmed that the ORR activities relied on the metal type, the ratio, and the carbonization temperature. Electrochemical measurements indicated that the sample of FCPA-900 shows the best ORR catalytic performance. Therefore, we believe that FCPA-900 is a promising candidate to substitute the commercial Pt/C catalyst.

4.2 Experimental

4.2.1 Catalysts preparation

All the raw materials (AR >99.5%) were purchased from the Wako Company. In detailed, 10 g of the phytic acid solution was adjusted the pH to 6.2 with Sodium hydroxide. Then the 3:1 ratio of $FeCl_3 \cdot 6H_2O$ and $CoCl_2 \cdot 6H_2O$ were added into the solution with 10 mL distilled water, stirring for more than 30 min to ensure the full polymerization. Transferred the thick pink solution in an open oven at 160^oC for 12 h. At last, the obtained brown powder was carbonization at the different temperatures of 800, 900 and 1000^oC for 3 h in Ar atmosphere. The black powder was stirred with 80 mL 3 M HCl to keep 10 h at 90^oC, and then filtered with more than 200 mL of distilled water to remove the impurities and unstable compounds. After the experiment process, FCPA-800, FCPA-900 and FCPA-1000 samples were obtained. F2CPA-900 (2:1 of $FeCl_3 \cdot 6H_2O$ and $CoCl_2 \cdot 6H_2O$) and F4CPA-900 (4:1 of $FeCl_3 \cdot 6H_2O$ and $CoCl_2 \cdot 6H_2O$) samples were prepared by the same experiment process with the carbonization at 900^oC, except for the different ratios of $FeCl_3 \cdot 6H_2O$ and $CoCl_2 \cdot 6H_2O$.

The same amount of $FeCl_3 \cdot 6H_2O$ or $CoCl_2 \cdot 6H_2O$ with the FCPA sample stirred with the PA solution (pH = 6.2) for 30 min, then dried and carbonized with the same process with the FCPA sample to obtain the sample of FPA-800, FPA-900, and FPA-1000 or CPA-800, CPA-900, and CPA-1000, respectively.

The single PA solution dried at 160°C for 12 h after adjusting the pH to 6.2, and then carbonized at 900°C before leaching with 3 M HCl and washing with 200 mL of distilled water. At last, the sample of PA-900 was obtained.

Scheme 1. Synthesis of dual transition metals embedded in P-doped porous carbon by the *in-situ* solid-state reaction method.

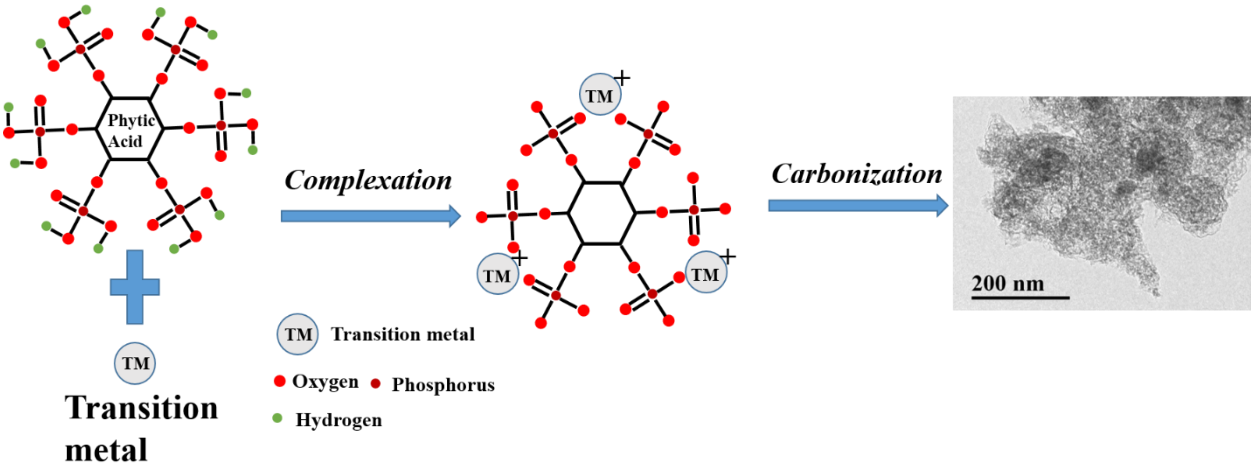

4.2.2 Physical characterizations

The crystalline was confirmed by powder X-ray diffraction (XRD) with the scanning step of 5° min^{-1} from 10° to 70°. The transmission electron microscopy (TEM, Tecnai G2 F20 S-TWIN) were used to analyze the catalyst's morphology and microstructure. In order to display the surface state of the catalyst, X-ray photoelectron spectroscopy (XPS, Thermo Escalab 250Xi) was recorded. The specific surface area is calculated by the Brunauer-Emmett-Teller (BET) method. In addition, the quenched solid density functional theory (QSDFT) was used to estimate the pore size distribution with the help of the N_2 adsorption. The trace amount of transition metals were confirmed by the inductively coupled plasma-atomic emission spectrometry (ICP-AES, SPS1700HVR).

4.2.3 Electrochemical measurements

A typical three-electrode system with a rotating disk electrode (RDE) setup from Pine Instrument Company connected to a CHI 760E electrochemistry workstation was used to explain the catalytic activity of the catalysts. As introduced in Chapter 2, 4 mg of the catalyst and the mixture solution: Nafion solution (5 wt. %, 0.1 mL), distilled water (0.15 mL), and IPA (isopropanol, 0.25 mL) are ultrasonic for about 0.5 hour to form the catalytic ink. Then

10 μL of the ink was transferred onto the GC electrode with a loading amount of 408 μg cm^{-2}. At the same time, the commercial Pt/C used as a comparison with the loading amount of 204 μg cm^{-2}. The N_2 and O_2-saturated 0.1 M KOH solution were used as the electrolyte. The electrochemical impedance spectroscopy (EIS) and Tafel curve were recorded to illustrate the effect of electrochemical reaction on interface impedance and the dynamic process of electrochemical reaction.

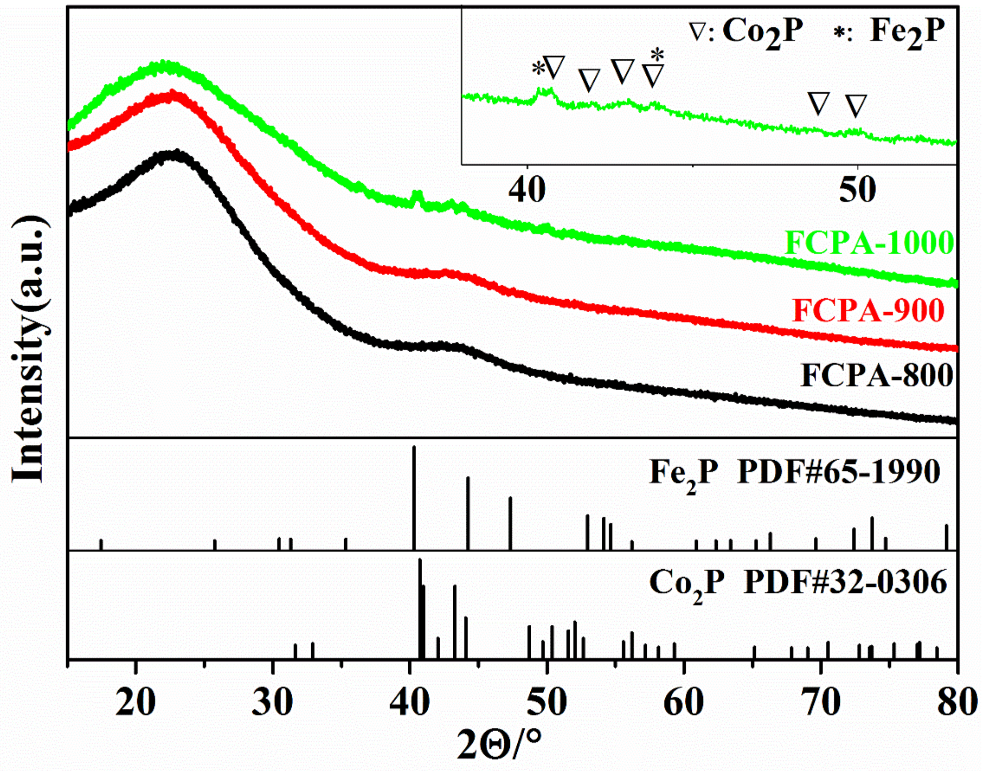

Figure 4.1 X-ray diffractograms for the three samples: FCPA-1000, FCPA-900 and FCPA- 800. The inset is the XRD detail pattern of FCPA-1000 from 38 to 53 degree. The bottom is the standard patterns of Fe_2P and Co_2P.

4.3 Results and discussion

4.3.1 XRD results

Figure 4.1 is the XRD pattern of FCPA catalyst. For all the samples, two broad peaks were found at ca. 25° and 43°, which belong to (002) and (100) crystalline plane of graphene. There is no any peaks in the FCPA-800 and FCPA-900 samples except for the two broad peaks of graphene, which means no impurity in the samples. However, some impurities are observed in the FCPA-1000 sample such as Co_2P (PDF# 32-0306) and Fe_2P (PDF# 65-1990), suggesting the over carbonization temperature. In the FPA samples, FPA-800 showed clearly $Fe_2P_4O_{12}$ peaks, and disappeared in the FPA-900, indicating the decomposing of $Fe_2P_4O_{12}$ in the high temperature. The weak and sharp Fe_2P peak would be confirmed in the FPA-1000, suggesting the over temperature. In the CPA-800 sample, very weak P peak was observed, getting stronger in the CPA-900. Similar to FPA sample, there is a $Co_2P_4O_{12}$ impurity in the CPA-900. In the sample of CPA-1000, the peaks of Co_2P was discovered, suggesting the same reason with FCPA and FPA samples. Comparison of these nine samples, we can obtain the reasons that the impurities rely on the carbonization temperature. That is due to that the carbon skeleton is broken to free amorphous carbon or phosphide with the temperature increasing [23]. However, there is a consensus that FCPA samples have fewer impurities than FPA and CPA samples due to the synergistic effect.

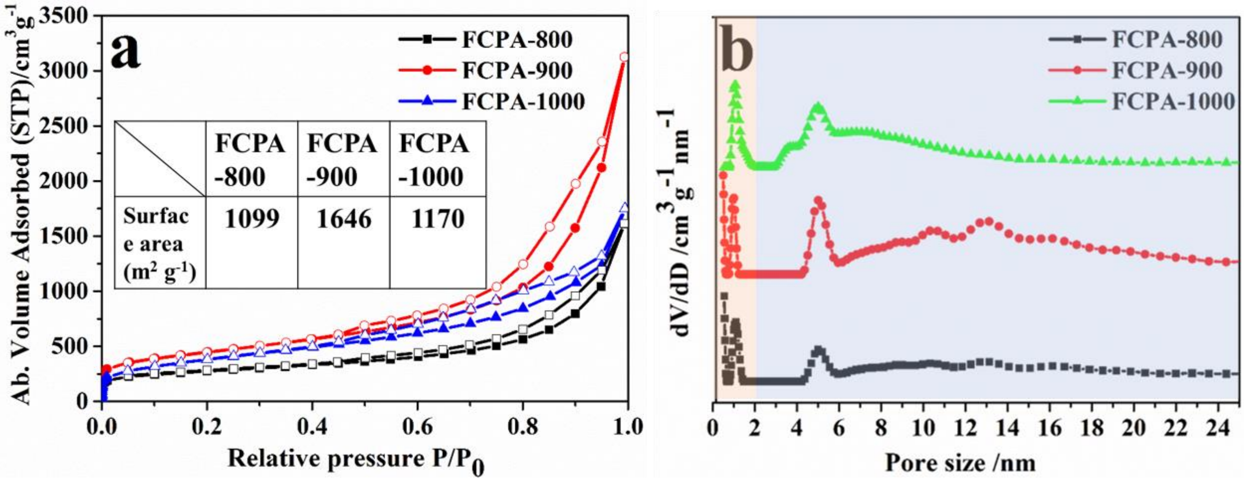

	FCPA -800	FCPA -900	FCPA -1000
Surface area (m^2 g^{-1})	1099	1646	1170

Figure 4.2 N_2 adsorption-desorption isotherms at 77 K (solid symbols are adsorption and open symbols are desorption) and pore size distributions of FCPA (a). The QSDFT model calculates the pore size distributions, the pink shade (0-2 nm) represents microspores and the blue shade (2-25 nm) represents mesoporous (b).

4.3.2 BET results

The nitrogen adsorption-desorption isotherms were carried out to illustrate the surface area of FCPA samples, which is a typical type- IV isotherm. A marked uptake is in Figure 4.2a close to zero, meaning the micropores structure in the sample. With the increasing the pressure, a hysteresis loop is appearing, corresponding to the mesopores structure. From the isotherms, the specific surface area of the FCPA-800, FCPA-900 and FCPA-1000 is about 1099 m^2 g^{-1}, 1646 m^2 g^{-1} and 1170 m^2 g^{-1}, respectively. The surface area relied on the temperature, the positive relationship is in the lower temperature, but converse in the higher temperature because of the over carbonization. The quenched solid density functional theory (QSDFT) was used to estimate the pore size distribution. All the samples show the micropores (1-5 nm) and mesopores (5-25 nm) in the structure. FCPA-900 implies the uniform dispersion due to the sharp and multiple peaks between the ranges of 5-25 nm. The micropores are increasing with the decreasing of mesopores, maybe due to the collapse of the carbon skeleton. It is believed that the hierarchical structures of support would supply more active sites and facilitate mass transport of ions to improve the catalytic activity.

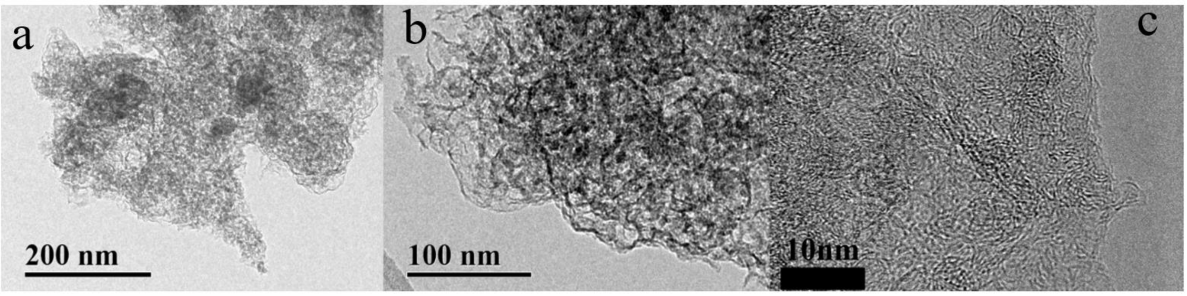

Figure 4.3 The TEM images of FCPA-900 at different magnifications 200 nm (a), 100 nm (b), and 10 nm (c).

4.3.3 TEM and EDS results

Transmission electron microscopic (TEM) was used to illustrate the morphology and microstructure of FCPA-900 catalyst, showing in Figure 4.3. The TEM shows that FCPA-900 mainly has the amorphous carbon structure [31]. Energy dispersive spectrometer (EDS) layer images of the FCPA-900 sample were used to explore the distribution of different elements (Figure 4.4). The Fe, Co, and P elements homogeneously distributed over the whole vision, which indicates that Fe, Co and P tri-doping material is successfully synthesized.

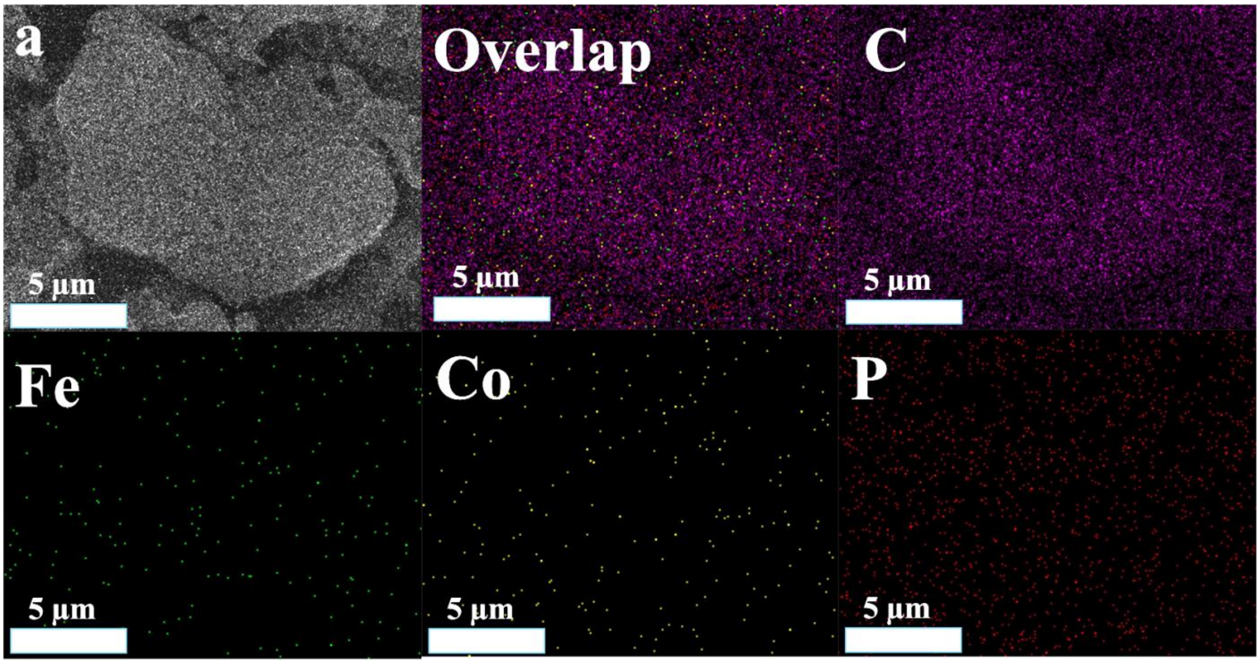

Figure 4.4 Energy dispersive X-ray spectroscopy (EDS) mapping of elements C, P, Co and Fe with corresponding to SEM (a) image.

4.3.4 XPS results

The surface states of the sample for different elements were detected by XPS. There are four obvious peaks at 533, 284.7, and 228 and 171 eV, which belong to the signals of O 1s, C 1s, and P 2p, respectively (Figure 4.5a) [25-26]. It should be noted that the peaks of the P element are higher than the standard location, which belongs to the energy loss line due to the machine limitation. The high-resolution C 1s can be further split into four synthetic peaks: 284.2 eV (C-C), 285.2 eV (C-O/C-P), 286.2 eV (C=O), and 290 eV (O-C=O), corresponding to the different states of carbon (Figure 4.5b). The O 1s spectra were split into six peaks to analyze the different oxygen-containing functional groups: 530.5, 531, 531.5, 532.3, 533.2, and 534.3 eV corresponding to Fe-O, Co-O, C=O /P=O, O-C/P-O-C, C-OH/P-OH, and O-C=O groups, respectively (Figure 4.5c) [28].

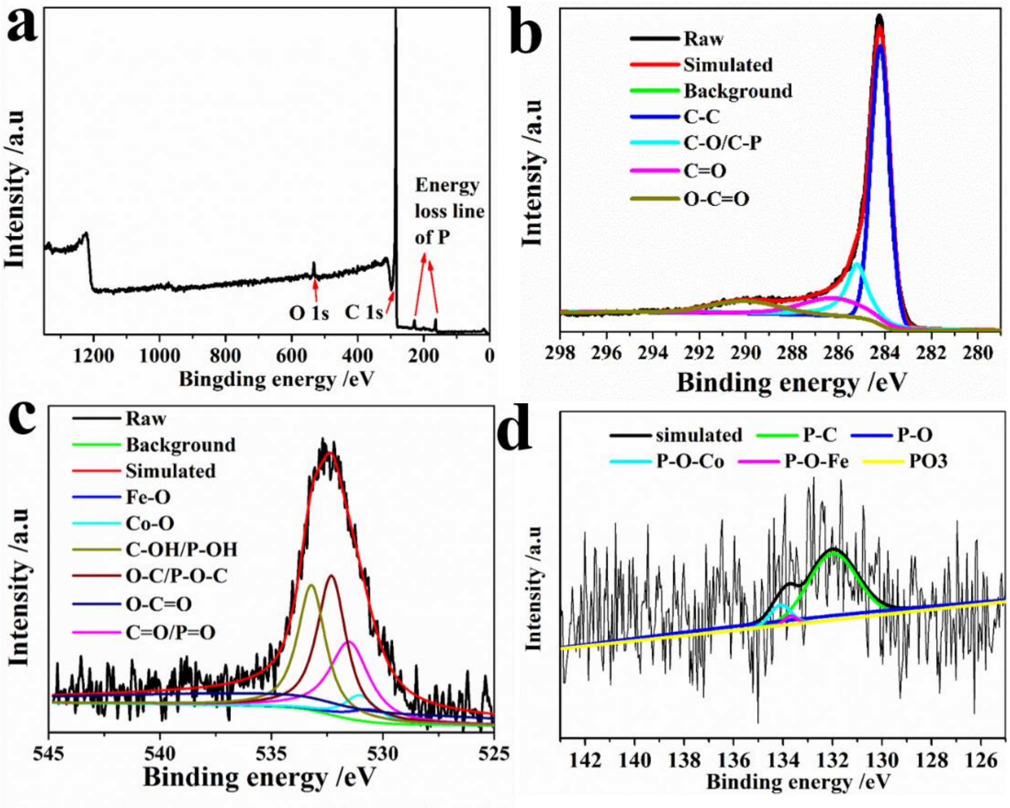

Figure 4.5 The full XPS spectra of FCPA-900 sample (a), C 1s (b), O 1s (c), and P2p (d).

In the FCPA-900, FPA-900, and CPA-900 samples, the P 1s signal was confirmed in the high-resolution, corresponding to P-C, P-O, P-O-Fe and/or P-O-Co, and metaphosphate (such as PO_3^- empirical formula) (Figure 4.5d). In the earlier report [23], only P-C and P-O signals can be observed in the high-resolution P 1s peak for PA-900 sample. In this thesis, the significant shift can be confirmed in the phosphorus binding energy due to the Fe and/or Co doping. Two relatively independent groups discovered the deeper reason, the metals doping lead to the hydration of the phosphates HPO_4^{2-} group [27-28]. Here, we give an example to analyze the FCPA-900 sample. P-C bonds are domination in the sample. P-O-Fe and P-O-Co bonds are in the sample, but the area of P-O-Co is larger than P-O-Fe, due to the acid washing and/or the natural properties of iron and cobalt. The weak and broad peak (the blue line) belongs to the trace phosphates P-O bond. Metaphosphate groups are too few to be observed in all the three samples, due to lacking the reaction condition at the high temperature. The similar results can be obtained from the FPA-900 sample. CPA-900 shows the different results: the domination is P-O and P-O-Co bonds due to the too much impurity $Co_2(P_4O_{12})$.

However, we cannot detect the signals of Fe 2p and Co 2p in three samples. Generally, the XPS instruments can detect the elements less than 20 Å from the surface, which is due to the intensity of X-ray decreased with the increasing depth. Therefore, in the FCPA-900, FPA-900, and CPA-900 sample, only the Fe and/or Co atoms close to the surface (several atomic layers) can be detected [29-30].

The ICP-AES was used to calculate the quantity of Fe and Co in the sample of FCPA-900. We obtained the content of Fe, Co, and P are 0.16 wt%, 1.2 wt%, and 0.9 wt%, respectively. It is clear that the contents are not in agreement with the starting ratio, due to the acidic washing and the intrinsic characteristics of the transition metal. Connected with the EDS, XRD, XPS, ICP, and TEM, we believed that the Fe, Co incorporated in P-doped porous carbon catalysts were successfully synthesized.

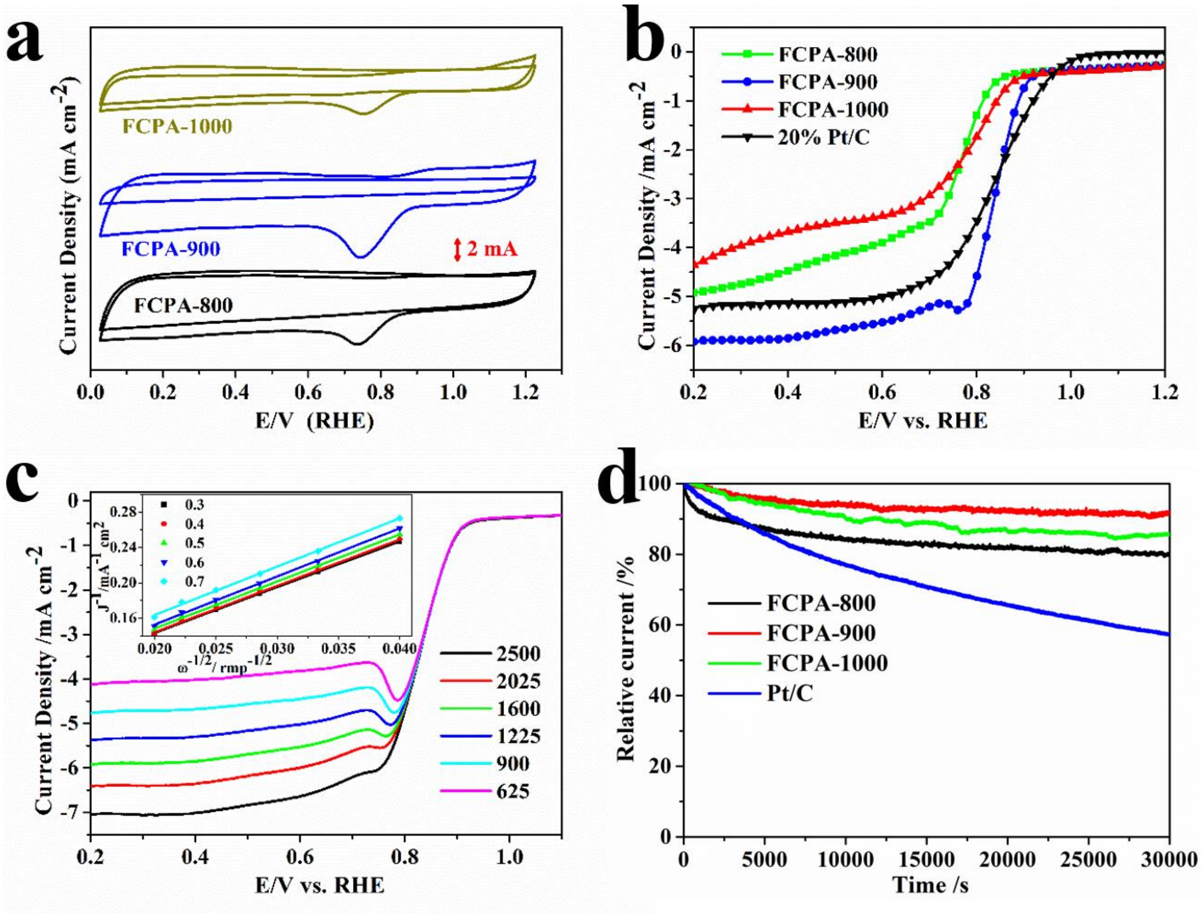

Figure 4.6 The CV curves of FCPA samples in N_2 or O_2 saturated electrolyte with a scan rate of 10mV s^{-1} (a). The LSV curves of FCPA samples and 20% Pt/C at 1600 rpm in O_2 saturated electrolyte (b). LSV curves of FCPA-900 at different rotation speeds and the K-L plots for FCPA-900 at different potentials (c). The electrochemical stability accessed by chronoamperometric curves of FCPA in O_2-saturated at a rotation speed of 300 rpm for 30000s (d). The entire test is in the 0.1 M KOH media.

4.3.5 Electrochemistry results and discussion

The ORR catalytic activity of catalysts FCPA-800, FCPA-900, and FCPA-1000 in the alkaline medium is shown in Figure 4.6a. The cyclic voltammetry (CV) measurement is in the N_2 and O_2-saturated 0.1 M KOH with the scan rate of 50 mV/s. It is clear that there are no peaks in the N_2-saturated electrolyte. The big difference is that a sharp reduction peak was observed in the O_2-saturated electrolyte. In addition, FCPA-900 shows the higher positive and sharper peak than other two sample, indicating the potential catalytic activity. The linear sweep voltammetry (LSV) was used to illustrate the catalytic properties of FCPA-800, FCPA-900, and FCPA-1000 catalysts with commercial Pt/C. Figure 4.6b shows that FCPA-900 sample has the more positive inflection point in the low current density. The highest onset-potential of 0.87 V *vs.* RHE than the other two samples, which means that the highest catalytic activities. The onset-potential is only 50 mV negative shift than the commercial Pt/C catalyst, but 15 mV positive shift for the half-wave potential, showing a promising catalytic activity (Table 4.1). In order to the comparison, we also investigated the FPA and CPA samples, obtained the similar results with the FCPA samples, indicating 900°C is the best carbonization temperature.

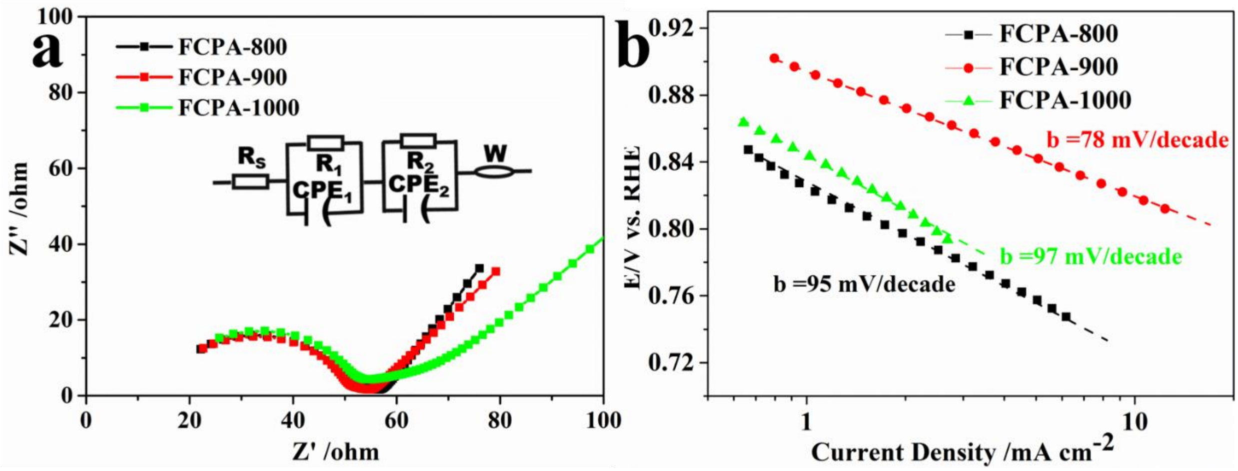

Figure 4.7 The impedance spectra fitting results of FCPA samples at open circles potential (a) and the equivalent circuit in the EIS of the sample (inset of a); The corresponding Tafel plots from LSV curves at 1600r (b). All the tests are in the 0.1 M KOH media.

The kinetics of the catalyst FCPA-900 was performed by the Koutecky–Levich (K–L) analysis, according to the LSV curves at the different rotation speeds with the scan rate of 10 mV/s. From Figure 4.6c, the electron transfer number of FCPA-900 sample is from 3.91-3.98 at the potential range of 0.3-0.7 V, suggesting the ORR process of FCPA-900 is the four-electron pathway. We also calculated FCPA-800 and FCPA-1000 samples electron transfer number shown in Table 4.1. FCPA-800 is same with FCPA-900 closer to 4 with the four-electron pathway; However, FCPA-1000 is estimated 3 to the electron transfer number, indicating that it is the mixture of 2 and 4-electron-transfer pathway in the reaction due to the phosphide purities.

The electronic impedance spectroscopy (EIS) was used to calculate the surface resistance in the electrochemical reaction. It is well known that a lower resistance is beneficial to electron transfer. Figure 4.7a is the EIS spectra of FCPA-800, FCPA-900, and FCPA-1000, the schematic illustration for the equivalent circuit is shown in the inset of Figure 4.7a, where R_s is the electrolyte resistance; R_1 is the electrons resistance of transferring in the P-doped porous carbon. We believe R_2 represents the surface resistance in the electrochemical reaction, which is about 5 ohms for FCPA-900, suggesting the excellent conductivity. In order to make the connection between the resistance and the catalytic activity, we input the resistance combined with the onset potential, the half-wave potential, and the limited current from the LSV data of 1600 rpm. The inverse line relationship shows that the catalyst with the lower resistance has the higher electrochemical activity [32].

Further exploring the kinetic process of the catalysts, the Tafel slope was used. As we know, the standard Tafel slope is close to 60 mV per decade for the effective reaction [33]. In fact, the measurements of platinum are different from the theoretical value, due to the condition and measurement error. In this chapter, we find the Tafel slope of FCPA-900 is 78 mV/dec, which is close to the 75 mV/dec of Pt. In addition, the FCPA-800 and FCPA-1000 are about 95 and 97 mV/dec, indicating that the ORR process is controlled by the first transfer electron step (Figure 4.7b). The CPA and FPA samples were also calculated to be from 90 to 100 mV/dec higher than Pt, showing the weak ORR process.

The superior catalytic activity and good stability are both essential for one excellent catalyst. The chronoamperometry measurement for all the samples is in 0.1 M KOH solution for 30,000 seconds with the rotation speed of 300 rpm to explore their stability, shown in Figure 4.6d. After scanning, only 5% attenuation for FCPA-900 compared to 50% for the commercial Pt/C catalyst under the same condition, indicating the higher stability. We also estimated all samples and proved that they are more stable than the commercial Pt/C.

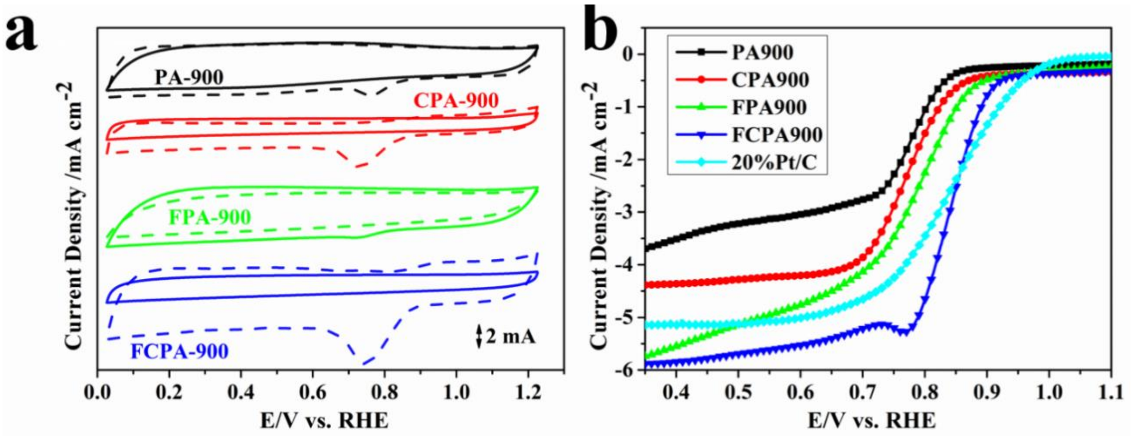

Figure 4.8 CV curves of four samples at a scan rate of 50 mV s^{-1} (a); LSV curves of 4 samples and 20% Pt/C at a scan rate of 10 mV s^{-1} (b). All the tests are in the 0.1 M KOH media.

All the electrochemical measurements show that FCPA-900 has the better catalytic activity than other two samples. We believe that the highest surface area, the lowest resistance, the most effective ORR process, and the suitable carbonization temperature are beneficial to promote oxygen reduction reaction.

In order to investigate the effect of a synergistic effect in the ORR process, PA-900, FPA-900, CPA-900, and FCPA-900 are explored, shown in Figure 4.8. The cyclic voltammetry (CV) data shows that there are no peaks in the N_2-saturated electrolyte with a scan rate of 50 mV/s. The catalytic activity of FPA-900 is higher than CPA-900, showing the higher onset-potential, and the limited current. FCPA-900 shows the highest onset-potential and the limited current in the CV and LSV data (Figure 4.8b), indicating that the synergistic effect is important to improve the ORR process. The synergistic effect whether relying on the ratios of two different metals is another question in this part. We explored that the different ratios of iron and cobalt in the experiment, the LSV and CV data show that the best ratio is 3:1 of Fe and Co. The more details showed in Table 4.1.

The kinetics of the catalysts PA-900, FPA-900, CPA-900, and FCPA-900 were performed by the Koutecky–Levich (K–L) analysis, which is come from LSV curves at different rotation speeds with the scan rate of 10 mV/s. After calculation, the electron transfer number of PA-900, FPA-900, and CPA-900 samples are close to 3.0 at the potential range of 0.3-0.7 V, suggesting that the 2-electron transfer pathway also occurred in the ORR process.

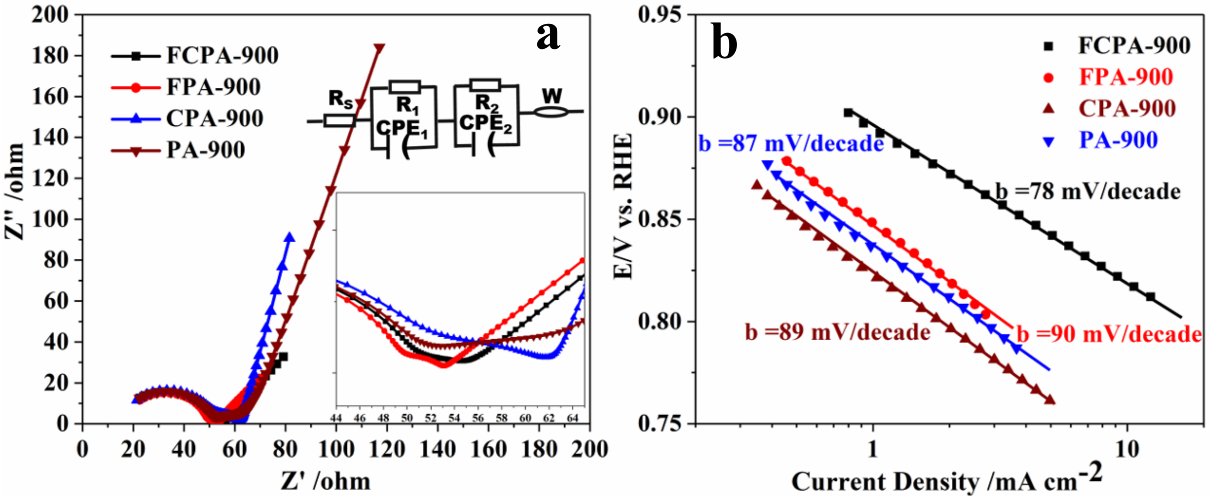

Figure 4.9 The impedance spectra fitting results of 900 samples at open circles potential (a), the equivalent circuit in the EIS of the sample and the enlarge images (inset of a); The corresponding Tafel plots from LSV curves at 1600 rpm (b). All the tests are in the 0.1 M KOH media.

The electronic impedance spectroscopy (EIS) was used to calculate the surface resistance in the electrochemical reaction (Figure 4.9a). The Zview program was used to estimate the electronic resistances of PA-900, FPA-900, CPA-900, and FCPA-900 samples, the schematic illustration for the equivalent circuit is shown in the inset of Figure 4.9a. We know that R_1 and R_S are the P-doped porous carbon or electrolyte resistance, due to their same resistance in all the samples. We believe that R_2 represents the surface resistance in the electrochemical reaction. FCPA-900 shows the lowest surface resistance, suggesting the highest conductivity. As discussed before, the low resistance value has advantages to improve the reaction, indicating the excellent electron transfer ability. We input the resistance combined with the onset potential, the half-wave potential and the limited current from the LSV data at 1600 rpm. The inverse line relationship shows that the catalyst with the lower resistance has the higher electrochemical activity.

In order to explore the kinetic process of the catalysts, the Tafel slope was introduced. The Tafel slopes of PA-900, FPA-900, and CPA-900 samples are close to 95 mV/dec. It is larger than the standard measurements 75 mV per decade of the commercial Pt/C catalyst and 78 mV per decade of FCPA-900, indicating the complicated ORR process (Figure 4.9b). The similar results can be obtained in the synergistic effect investigation.

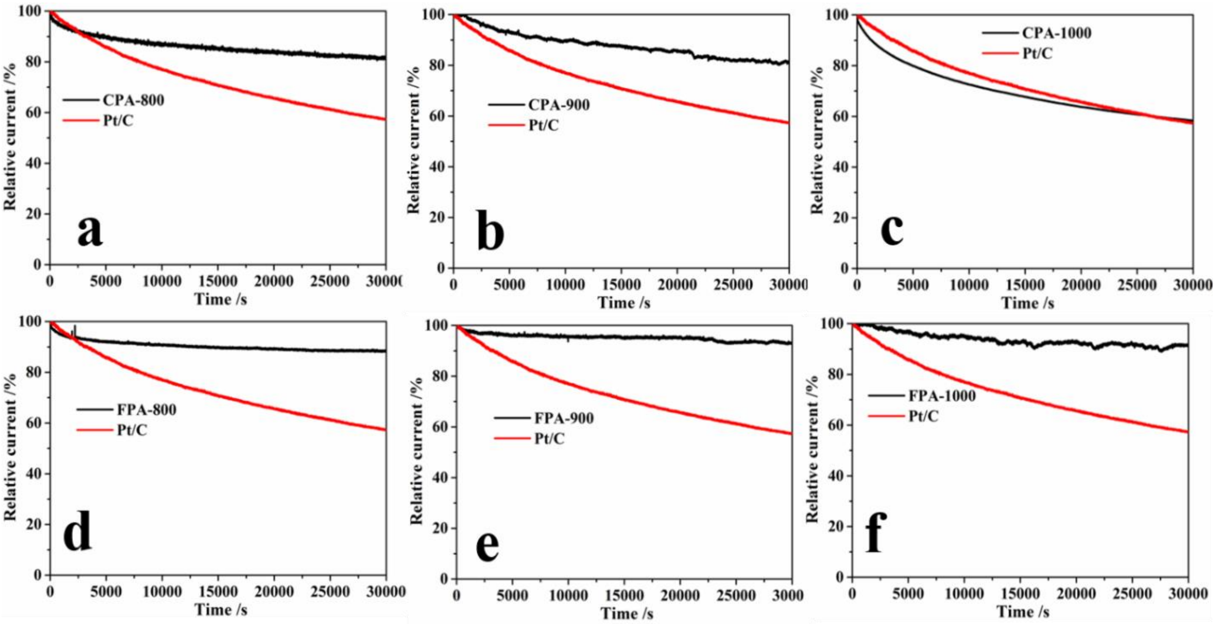

Figure 4.10 Electrochemistry stability accessed by chronoamperometric curves of all the samples in O_2-saturated 0.1 M KOH media at a rotation speed of 300 rpm for 30000s (a-f).

The superior catalytic activity and good stability are essential for one excellent catalyst. The chronoamperometry measurements for PA-900, FPA-900, CPA-900, and FCPA-900 samples is in 0.1 M KOH solution for 30,000 seconds with the rotation speed of 300 rpm to explore their stability, shown in Figure 4.10. After scanning, less attenuation for PA-900, FPA-900, and CPA-900 than 50% for the commercial Pt/C under the same condition, indicating the excellent stability. We also estimated all samples, and proved that they are stabler than the commercial Pt/C catalyst.

After the different electrochemical measurements, such as CV, LSV, EIS, Tafel curve, and K-L calculation, we confirmed that FCPA-900 has better catalytic activities than other samples. The high surface area of porous carbon and evenly distributed pore size mean more active sites and fast electrons transport. The P doping would change the symmetry of the carbon atomic spin density to increase the adsorption ability of O atoms, and the metals doping strengthen the asymmetry to promote the ORR process [11-12, 34]. At the same time, we also believe that the synergistic effect of the transition metals is beneficial for the reactant adsorption and reduction on the catalyst surface [35].

Table 4.1. The ORR performance of different catalysts in alkaline media

Sample	**Onset-potential (V)**	**Half- -wave potential (V)**	**Diffusion Limiting current (mA/cm^2)**	**Electron transfer number at 0.5V**	**Tafel plot value (mV/dec)**	**Resistance value (ohm)**
PA-900	0.83	0.76	4.10	2.09	87	18.67
CPA-800	0.81	0.75	3.89	3.12	87	24.11
CPA-900	0.84	0.77	4.30	2.88	89	14.32
CPA-1000	0.77	0.69	1.65	1.62	93	56.28
FPA-800	0.84	0.75	4.80	3.26	98	11.53
FPA-900	0.87	0.76	5.68	3.72	90	3.35
FPA-1000	0.85	0.69	3.65	2.32	99	16.25
FCPA-800	0.83	0.76	4.92	3.64	95	9.30
FCPA-900	0.91	0.84	5.92	4.28	78	5.03
FCPA-1000	0.88	0.77	4.34	3.04	97	11.44
F4CPA-900	0.84	0.77	5.03	4.36	97	9.27
F2CPA-900	0.85	0.78	4.97	4.37	99	11.89
20% Pt/C	0.96	0.84	5.25	4.00	75	—

4.4 Conclusions

In this part, we successfully prepared a series of ORR catalysts Fe, Co, P tri-doping porous carbon by the *in-situ* solid-state carbonization method. The effect of the carbonization temperatures, the components, and the ratios between the transition metals was investigated in terms of the ORR performance. In the study, we established the correlation between the carbonization temperature and the dual transition metals co-doping. The sample of FCPA-900 shows the best ORR catalytic activities because of the higher specific surface area and better-defined amorphous carbon structure. At the same time, we found that the synergistic effect of the transition metals would improve the electrocatalytic activity. In short, we developed a new excellent ORR catalyst FCPA-900, displaying a comparable electrocatalytic activity with the commercial Pt/C catalyst. The FCPA-900 sample has a great potential to substitute the Pt/C catalyst.

4.5 References

[1] Shao, M.; Chang, Q.; Dodelet, J. P.; Chenitz, R. Recent advances in electrocatalysts for oxygen reduction reaction. *Chemical Reviews* **2016**, *116*, 3594-3657.

[2] Nie, Y.; Li, L.; Wei, Z. Recent advancements in Pt and Pt-free catalysts for oxygen reduction reaction. *Chemical Society Reviews* **2015**, *44*, 2168-2201.

[3] Zhang, W.; Lai, W.; Cao, R. Energy-related small molecule activation reactions: oxygen reduction and hydrogen and oxygen evolution reactions catalyzed by porphyrin-and corrole-based systems. *Chemical Reviews* **2016**, *117*(4), 3717-3797.

[4] Zhang, C.; Shen, X.; Pan, Y.; & Peng, Z. A review of Pt-based electrocatalysts for oxygen reduction reaction. *Frontiers in Energy*, **2017** *11*(3), 268-285.

[5] Qian, Y.; Khan, I. A.; Zhao, D. Electrocatalysts derived from metal–organic frameworks for oxygen reduction and evolution reactions in aqueous media. *Small* **2017**, *13*(37), 1701143.

[6] Gopalsamy, K.; Balamurugan, J.; Thanh, T. D.; Kim, N. H.; Hui, D.; Lee, J. H. Surfactant-free synthesis of NiPd nanoalloy/graphene bifunctional nanocomposite for fuel cell. *Composites Part B: Engineering* **2017**, *114*, 319-327.

[7] Ishihara, A.; Tamura, Y.; Chisaka, M.; Ohgi, Y.; Kohno, Y.; Matsuzawa, K.; Ota, K. I. Titanium-niobium oxides as non-noble metal cathodes for polymer electrolyte fuel cells. *Catalysts* **2015**, *5*(3), 1289-1303.

[8] Yuan, Y.; Yang, L.; He, B.; Pervaiz, E.; Shao, Z.; & Yang, M. Cobalt–zinc nitride on nitrogen doped carbon black nanohybrids as a non-noble metal electrocatalyst for oxygen reduction reaction. *Nanoscale* **2017**, *9*(19), 6259-6263.

[9] Zhang, J.; Zhao, Z.; Xia, Z.; & Dai, L. A metal-free bifunctional electrocatalyst for oxygen reduction and oxygen evolution reactions. *Nature nanotechnology* **2015**, *10*(5), 444.

[10] Guo, D.; Shibuya, R.; Akiba, C.; Saji, S.; Kondo, T.; Nakamura, J. Active sites of nitrogen-doped carbon materials for oxygen reduction reaction clarified using model catalysts. *Science* **2016**, *351*(6271), 361-365.

[11] Xing, T.; Zheng, Y.; Li, L. H.; Cowie, B. C.; Gunzelmann, D.; Qiao, S. Z.; Chen, Y. Observation of active sites for oxygen reduction reaction on nitrogen-doped multilayer graphene. *ACS Nano* **2014**, *8*(7), 6856-6862.

[12] Gong, K.; Du, F.; Xia, Z.; Durstock, M.; Dai, L. Nitrogen-doped carbon nanotube arrays with high electrocatalytic activity for oxygen reduction. *Science* **2009**, *323*(5915), 760-764.

[13] Liang, J.; Jiao, Y.; Jaroniec, M.; Qiao, S. Z. Sulfur and nitrogen dual–doped mesoporous graphene electrocatalyst for oxygen reduction with synergistically enhanced performance. *Angewandte Chemie International Edition* **2012**, *51*(46), 11496-11500.

[14] Masa, J.; Zhao, A.; Xia, W.; Sun, Z.; Mei, B.; Muhler, M.; Schuhmann, W. Trace metal residues promote the activity of supposedly metal-free nitrogen-modified carbon catalysts for the oxygen reduction reaction. *Electrochemistry Communications* **2013**, *34*, 113-116.

[15]Wang, L.; Ambrosi, A.; Pumera, M. “Metal–Free” catalytic oxygen reduction reaction on heteroatom-doped graphene is caused by trace metal impurities. *Angewandte Chemie International Edition* **2013**, *52*(51), 13818-13821.

[16] He, D.; Xiong, Y.; Yang, J.; Chen, X.; Deng, Z.; Pan, M.; Mu, S. Nanocarbon-intercalated and Fe–N-codoped graphene as a highly active noble-metal-free bifunctional electrocatalyst for oxygen reduction and evolution. *Journal of Materials Chemistry A* **2017**, *5*(5), 1930-1934.

[17] Gadipelli, S.; Zhao, T.; Shevlin, S. A.; Guo, Z. Switching effective oxygen reduction and evolution performance by controlled graphitization of a cobalt–nitrogen–carbon framework system. *Energy Environmental Science* **2016**, *9*(5), 1661-1667.

[18] Bu, L.; Shao, Q.; E, B.; Guo, J.; Yao, J.; Huang, X. PtPb/PtNi intermetallic core/atomic layer shell octahedra for efficient oxygen reduction electrocatalysis. *Journal of the American Chemical Society* **2017**, *139*(28), 9576-9582.

[19] Li, Y.; Kuttiyiel, K. A.; Wu, L.; Zhu, Y.; Fujita, E.; Adzic, R. R.; Sasaki, K. Enhancing the electrocatalytic performance of bifunctional cobalt–manganese–oxynitride nanocatalysts on graphene. *ChemSusChem* **2017**, *10*(1), 68-73.

[20] Guan, B. Y.; Lu, Y.; Wang, Y.; Wu, M.; Lou, X. W. D. Porous iron–cobalt alloy/nitrogen–doped carbon cages synthesized via pyrolysis of complex metal-organic framework hybrids for oxygen reduction. *Advanced Functional Materials* **2018**, *28*(10), 1706738.

[21] Wu, G.; More, K. L.; Johnston, C. M.; Zelenay, P. High-performance electrocatalysts for oxygen reduction derived from polyaniline, iron, and cobalt. *Science* **2011**, *332*(6028), 443-447.

[22] Chang, J.; Xiao, Y.; Xiao, M.; Ge, J.; Liu, C.; Xing, W. Surface oxidized cobalt-phosphide nanorods as an advanced oxygen evolution catalyst in alkaline solution. *ACS Catalysis* **2015**, *5*(11), 6874-6878.

[23] Singh, K. P.; Bae, E. J.; Yu, J. S. Fe–P: a new class of electroactive catalyst for oxygen reduction reaction. *Journal of the American Chemical Society* **2015**, *137*(9), 3165-3168.

[24] Razmjooei, F.; Singh, K. P.; Bae, E. J.; Yu, J. S. A new class of electroactive Fe-and P-functionalized graphene for oxygen reduction. *Journal of Materials Chemistry A* **2015**, *3*(20), 11031-11039.

[25] Yu, D.; Wu, C.; Kong, Y.; Xue, N.; Guo, X.; Ding, W. Structural and catalytic investigation of mesoporous iron phosphate. *The Journal of Physical Chemistry C* **2007**, *111*(39), 14394-14399.

[26] Yan, R.; Gao, X.; He, W.; Guo, R.; Wu, R.; Zhao, Z.; Ma, H. A simple and convenient method to fabricate new types of phytic acid–metal conversion coatings with excellent anti-corrosion performance on the iron substrate. *RSC Advances* **2017**, *7*(65), 41152-41162.

[27] Yan, D.; Dou, S.; Tao, L.; Liu, Z.; Liu, Z.; Huo, J.; Wang, S. Electropolymerized supermolecule derived N, P co-doped carbon nanofiber networks as a highly efficient metal-free electrocatalyst for the hydrogen evolution reaction. *Journal of Materials Chemistry A* **2016**, *4*(36), 13726-13730.

[28] Li, H. Y.; Liu, L.; Zhang, Z. W.; Wang, S. S.; Yu, Y.; Liu, L.; Wu, Y. Phytic acid-assisted electrochemically synthesized three-dimensional O, P-functionalized graphene monoliths with high capacitive performance. *Nanoscale* **2017**, *9*(34), 12601-12608.

[29] Toda, T.; Igarashi, H.; Uchida, H.; Watanabe, M. Enhancement of the electroreduction of oxygen on Pt alloys with Fe, Ni, and Co. *Journal of the Electrochemical Society* **1999**, *146*(10), 3750-3756.

[30] Ding, X.; Yin, S.; An, K.; Luo, L.; Shi, N.; Qiang, Y.; Shen, P. K. FeN stabilized FeN@ Pt core–shell nanostructures for oxygen reduction reaction. *Journal of Materials Chemistry A* **2015***3*(8), 4462-4469.

[31] Li, Y.; Xu, H.; Huang, H.; Gao, L.; Zhao, Y.; Ma, T. Facile synthesis of N, S co-doped porous carbons from a dual-ligand metal organic framework for high performance oxygen reduction reaction catalysts. *Electrochimica Acta* **2017**, *254*, 148-154.

[32] Li, Y.; Zhou, W.; Wang, H.; Xie, L.; Liang, Y.; Wei, F.; Dai, H. An oxygen reduction electrocatalyst based on carbon nanotube–graphene complexes. *Nature Nanotechnology* **2012**, *7*(6), 394.

[33] Li, L.; Dai, P.; Gu, X.; Wang, Y.; Yan, L.; Zhao, X. High oxygen reduction activity on a metal–organic framework derived carbon combined with high degree of graphitization and pyridinic-N dopants. *Journal of Materials Chemistry A* **2017**, *5*(2), 789-795.

[34] Chai, G. L.; Qiu, K.; Qiao, M.; Titirici, M. M.; Shang, C.; Guo, Z. Active sites engineering leads to exceptional ORR and OER bifunctionality in P, N Co-doped graphene frameworks. *Energy Environmental Science 10*(5), **2017**, 1186-1195.

[35] Deng, J.; Ren, P.; Deng, D.; Yu, L.; Yang, F.; Bao, X. Highly active and durable non-precious-metal catalysts encapsulated in carbon nanotubes for hydrogen evolution reaction. *Energy Environmental Science* **2014**, *7*(6), 1919-1923.

Chapter 5 2-D material MXene Nb_2C synthesized by the traditional molten salt assisted solid-state reaction method at the low temperature as the ORR catalyst support

5.1 Introduction

The new 2-D materials MAX compounds attract great attention due to their electrical conductivity, high surface area, and corrosion resistance since it was first discovered in 2011. 2-D materials MAX show an extensive application in the different fields, such as ions battery, solar cell, supercapacitor, and electrocatalyst [1-5]. However, the sintering temperature is too high to hinder their application. MXene, which is etching from the corresponding MAX compounds, is a new family of transition metal carbide, carbonitride, or nitride [6, 7]. Among the different MXene compounds, metal carbides were investigated a lot, such as Ti_2C, Ti_3C_2, and Nb_2C, displaying the excellent electronic, mechanical, and optical properties [8-10]. However, in decades, almost no paper reports focus on the synthesized method under the mild condition.

Proton exchange membrane fuel cell (PEMFC) is important to change the energy structure because of the high-energy transfer efficiency with the increasing energy demands [11-14]. However, the ORR Pt-based catalyst limited its wide application of PEMFC due to expensive, corrosion, and the rare metal. It is believed that the corrosion has a strong correlation with the supporter [15]. It is a knowledge that a high electrical conductivity, high surface area, and corrosion resistance are necessary for a good catalyst support. Due to these factors, 2D materials are becoming the best choice. Carbon materials, especially for Vulcan XC-72, are the widely used as support in the world due to their high surface area and conductivity [16-19]. Nevertheless, many papers prove that the lower corrosion resistance of carbon support is the main reason of low durability of PEMFC [18]. In the cycle of potential for zero to the onset potential, some carbon oxide occurred to separate noble particles from carbon support, even poison the active noble particles. Therefore, it is urgent to explore stable alternatives to substitute the carbon materials as catalyst support [20-24].

Recently, 2-D materials MXene as support are reported, such as Ti_3C_2 support Pt nanoparticles [20] or MnO_2 nanowires [22], displaying excellent ORR catalytic activities. However, the over-high sintering temperature conditions limit their deep investigation.

Herein, we reported a new idea to synthesize the MAX Nb_2AlC compound with the traditional molten salt assisted solid-state reaction method at low temperature. In the reaction, we successfully decreased the synthesized temperature by 600°C. Among them, we choose one sample as an example to load Pt nanoparticle to obtain its electrochemical performance, such as CV, LSV, EIS, K-L equation, and Tafel curves. Clearly, the Pt-loading sample shows good electrocatalytic properties. We believe that 2-D material Nb_2C is a promising candidate as the support to substitute the usual carbon.

5.2 Experimental

5.2.1 Synthesis of the MAX compound Nb_2AlC

The synthesized method is investigated for four parts: the choosing of molten salt or flux, the temperature of controlling, the heating time, and the amount of molten salt or flux. The samples name are listed in Table 5.1.

1. The exploration of different molten salts or fluxes

The Nb_2AlC (NAC) powder was obtained by the conventional solid-state reaction method. The starting materials of Al (0.18 g), Nb (1.1 g), C (0.07 g), and NaCl (5 g) were ground carefully in an agate mortar, and then transferred into an alumina boat. The mixture compound was heated in furnace tube under the Ar atmosphere for 12 hours at 1000°C. Then the gray particle was washed with 9 M HCl solution, centrifuged, and then dried in a vacuum oven at 60°C to obtain the black powder, named as NAC-1. At the same time, NAC-2 was prepared using KCl as the molten salt by the same process with NAC-1. NAC-3 was synthesized with 1.8 g Al as the flux. NAC-4 is using the mixture compounds (KCl, KF, and LiCl) as the molten salt, and heated for 48 hours. As the comparison, the starting materials Al (0.18 g), Nb (1.1 g) and C (0.07 g) without any molten salt or flux were heated for 72 hours to obtain the NAC-5 sample.

2. The temperatures of controlling

The starting materials Al (0.18 g), Nb (1.1 g), C (0.07 g), and NaCl (5 g) were ground carefully in an agate mortar, and then transferred into an alumina boat. The mixture compound was heated in furnace tube under the Ar atmosphere for 12 hours at 850°C and 1000°C. Then followed experiment process is the same with NAC-1, named as NAC-6 and NAC-1 samples, respectively.

3. The investigation of heating time

Similar to the NAC-1 sample experiment process, the same amount of starting materials was heated for the different time, such as 12h (NAC-1), 24h (NAC-7), 36h (NAC-8), 48h (NAC-9). The followed experiment process is the same as the NAC-1.

4. The investigation of the amount of molten salt

The starting materials Al (0.18 g), Nb (1.1 g), C (0.07 g), and NaCl (5/10 g) were ground carefully in an agate mortar, and then transferred into an alumina boat. The mixture compound was heated in furnace tube under the Ar atmosphere for 24/36/48 hours at 1000°C. The followed experiment process is the same as the NAC-1. In this case, we named the samples one by one: 5 g + 24 h as NAC-7; 10 g + 24 h as NAC-10; 5 g + 36 h as NAC-8; 10 g + 36 h as NAC-11; 5 g + 48 h as NAC-9; 10 g + 48 h as NAC-12.

5. The investigation of the etching method

In order to obtain the layered structure sample, we set the NAC-9 and NAC-12 as the example. About 0.5 g NAC-9 or NAC-12 sample was transferred into a plastic bottle stirred with 10 mL HF for 72 h at 60°C. Then the solution was centrifuged at 10000 rpm for 10 min, and dried at 60°C in a vacuum oven for 24 hours. The samples were obtained named as NAC-91 and NAC-121 to make more measurements.

6. The loading method of Pt nanoparticles

The NAC-9/Pt and NAC-91/Pt catalysts were prepared by the following method. The mixed solution of 20 mL of 2 mmol/L $H_2PtCl_6 \cdot 6H_2O$ and 13.5 mL of distilled water was slowly dropped into the core solution for 1 hour, corresponding to 0.078 $mg_{Pt.}$ Then, 0.078g of NAC-9 or NAC-91 were mixed into the solution, acted as the support. After stirring for 24 hours, the filtered products washed with distilled water several times were obtained after dried in an open oven at 60°C, named as NAC-9/Pt and NAC-91/Pt.

5.2.2 Physical characterizations

The crystalline was confirmed by the powder X-ray diffraction (XRD) with the scanning speed of 5° min^{-1} from 5° to 80°. The scanning electron microscope (SEM, JEOL-6900) was used to analyze the catalyst's morphology and microstructure. In order to display the surface state of the catalyst, X-ray photoelectron spectroscopy (XPS, Thermo Escalab 250Xi) and energy dispersive spectroscopy (EDS) were introduced.

Table 5.1 the sample name of different temperature process with the impurities results

	Time (h)	Degree (°C)	The quality of flux (g)	Flux	Phase compositions in the samples
NAC-1	12	1000	5	NaCl	NbC, Al_3Nb, $NbAl_2$, Nb_2AlC
NAC-2	12	1000	5	KCl	NbC, Al_3Nb, Nb, $NaAlCl_4$
NAC-3	12	1000	5	Al	NbC,Al_3Nb
NAC-4	48	1000	5	KF, LiF, KCl	NbC, Al_3Nb
NAC-5	72	1000	0	None	NbC, Al_3Nb, Nb
NAC-6	12	850	5	NaCl	NbC, Nb
NAC-7	24	1000	5	NaCl	NbC, Al_3Nb, Nb Al_2, Nb_2AlC, C
NAC-8	36	1000	5	NaCl	NbC, $NbAl_2$, Nb_2AlC, C
NAC-9	48	1000	5	NaCl	NbC, $NbAl_2$, Nb_2AlC, C
NAC-10	24	1000	10	NaCl	NbC, $NbAl_2$, Nb_2AlC, Al_3Nb
NAC-11	36	1000	10	NaCl	NbC, $NbAl_2$, Nb_2AlC, Al_3Nb
NAC-12	48	1000	10	NaCl	NbC, $NbAl_2$, Nb_2AlC, Al_3Nb

5.2.3 Electrochemical measurements

A typical three-electrode system with a rotating disk electrode (RDE) setup from Pine Instrument Company connected to a CHI 760E electrochemistry workstation was used to explain the catalytic activity of the catalysts. As introduced in Chapter 2, 6 mg of the catalyst with the mixture solution: Nafion solution (5 wt. %, 0.1 mL), distilled water (0.15 mL), and IPA (0.25 mL) are ultrasonic for about 0.5 hours to form the catalytic ink. Then 10 µL of the ink was transferred onto the GC electrode with a loading amount of 489 µg cm^{-2} (corresponding to a 48.9 $\mu g_{Pt}/cm^2$, thus no loss in the experiment process). At the same time, the commercial Pt/C used as a comparison with the loading amount 48.9 $\mu g_{Pt}/cm^2$. The N_2 and O_2–saturated 0.1 M KOH solution was used as the electrolyte. The electrochemical impedance spectroscopy (EIS) and the Tafel curve were recorded to illustrate the effect of electrochemical reaction on interface impedance and the dynamic process of electrochemical reaction.

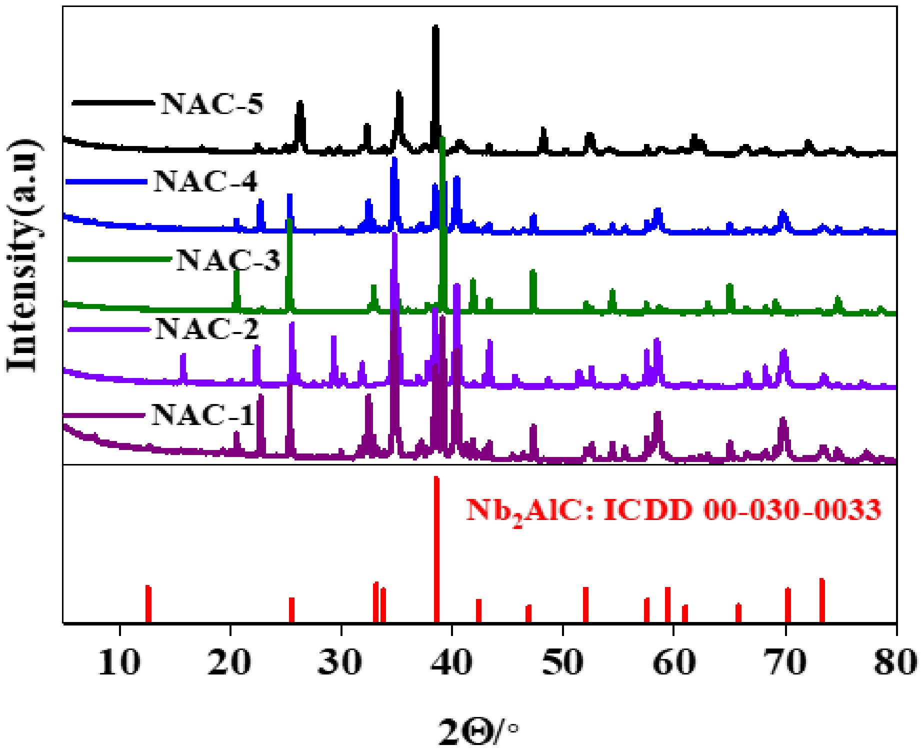

Figure 5.1 XRD patterns of different samples for the diverse molten salts of fluxes.

5.3 Results and discussion

5.3.1 XRD and SEM results

Figure 5.1 is the XRD pattern of NAC 1-5 sample. In the NAC-1 pattern, it is clear that a weak peak at ca. 10° can be observed, which is the typical peak of Nb_2AlC. Except for the typical peak, the other peaks of Nb_2AlC can also be observed in the NAC-1 XRD pattern, suggesting little target compound in the samples. Generally, the impurities come from the starting material, such as NbC, and Nb_2Al. For the NAC 1-5 samples, four sharp and strong peaks were found at ca. 35°, 40°, 60°, and 70°, belonging to the different crystalline planes of NbC (ICDD No. 03-065-7964). Except for the NbC impurities, we also confirmed the Al_3Nb and $NaNbO_3$, due to the strong oxidation in the high temperature. In the NAC-2, too many impurities in the sample, NbC is the main phase and $K_6Nb_{10.8}O_{30}$ as the new impurity appears due to the incompletely sealed tube furnace. However, there is no typical peak of Nb_2AlC in the XRD pattern, indicating no target products in the sample. The starting material as the molten salt or flux is good for the reaction, because it cannot bring in the new atoms. NAC-3, using the Al as the flux to decrease the whole reaction temperature, shows the XRD pattern in Figure 5.1. Only two different products peaks can be observed, Al_3Nb and CNb, which is very different from the former two XRD pattern. The reason is that the starting material is surrounding by the NaCl or KCl ions liquid at the high temperature, but the molten Al would lead to the starting materials dispersion on the surface of the metal liquid due to the high surface tension. According to the phase diagram, the lower melting point of the flux, the more decreasing the whole reaction temperature. At last, we choose the traditional mixture (KCl, KF, and LiCl) as the molten salt, which the melting point is only 300°C lower than that of NaCl 800°C, shown in Figure 5.1. NbC is the main phase in the sample with other impurities. Unfortunately, there are no peaks of Nb_2AlC in the XRD pattern. By now, we investigated the effect of different molten salts or fluxes in the reaction. However, we have no idea whether the Nb_2AlC can be synthesized without any molten salt or flux or not. In NAC-5, the reaction only heated at the 1000°C for 72 h. Clearly, no peaks of Nb_2AlC in the XRD pattern, except for the NbC and Al_2O_3 peaks, suggesting that the molten salt is important for the reaction.

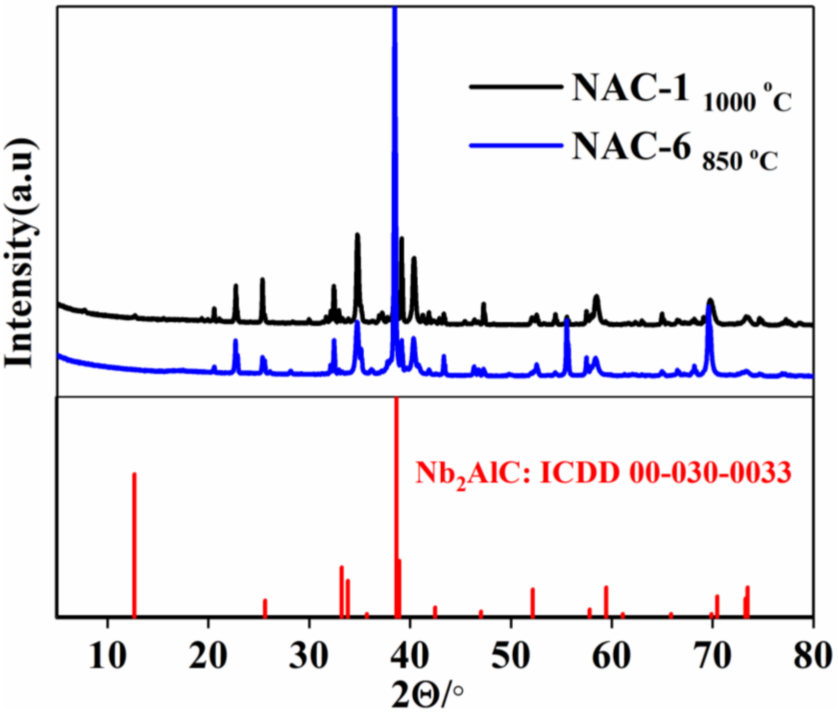

Figure 5.2 XRD patterns of different samples for diverse reaction temperature.

As we know, the traditional synthesized method to obtain Nb_2AlC is at the over-higher temperature [25-26]. In this paragraph, we confirmed the suitable temperature. Firstly, we set the heated temperature lower than 1100°C, due to the scientific value. Secondly, we need to obtain the typical product at the as low as the heating temperature. Figure 5.2 shows the two samples heated at the different heating temperatures at the same time. They show the similar XRD pattern. However, the incomplete reaction is in the lower temperature, such as the obvious peaks of Nb. NAC-1 shows the clear but weak typical peak of Nb_2AlC, displaying the suitable reaction temperature. More interestingly, there are no peaks of Al, indicating that Al is completely reacted [25]. In other words, the reaction equation is:

$$3Al + Nb = Al_3Nb \qquad (5.1)$$

Figure 5.3 shows the XRD patterns of NAC-1 and NAC-7~9. NAC-1 is heated for 12 hours showing a weak typical peak of Nb_2AlC. NAC-7 shows the similar XRD pattern with the sample of NAC-1, but a stronger typical peak. Al_3Nb still occupy the main phase and get stronger. Except for these, the tiny impurities peaks disappear, suggesting that increasing the heating time is beneficial to decrease the tiny peaks [27]. Continuing to increase the heating time (NAC-8), Al_3Nb is disappeared with the stronger peaks of Nb_2AlC. Nb_2Al as the impurity come out, suggesting the Nb_2Al is an intermediate product after Al_3Nb [25]. Therefore, the reaction equation can be given as:

$$Al_3Nb + 5Nb = 3Nb_2Al \qquad (5.2)$$

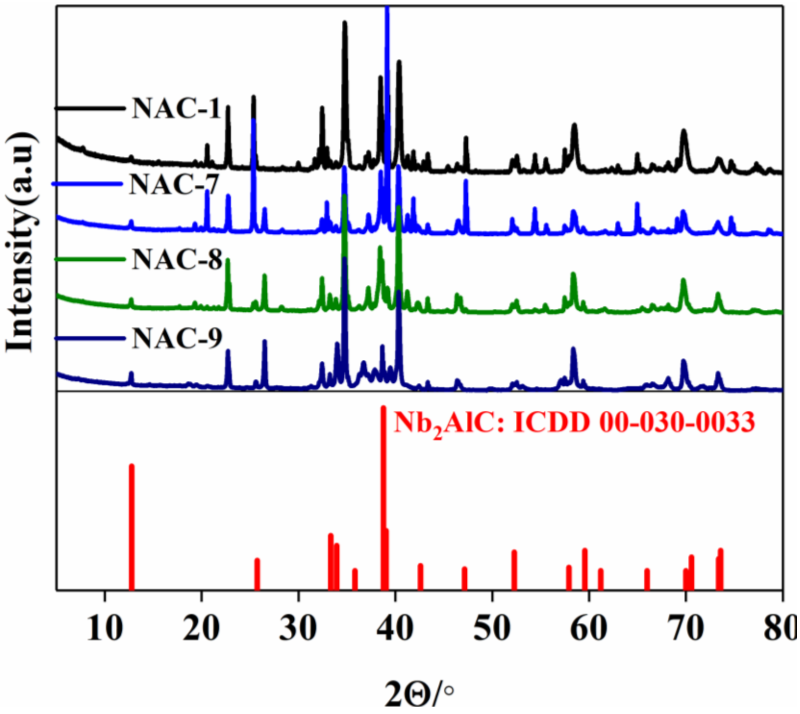

Figure 5.3 XRD patterns of different samples for diverse reaction time.

Compared to the NAC-8, NAC-9 shows few tiny peaks in the XRD pattern, and the dominated phase are Nb_2AlC and NbC. The Nb_2Al peak is getting weak with the stronger Nb_2AlC, indicating that partial Nb_2Al reacted with C or NbC to synthesize Nb_2AlC. The results of the heating time investigation show that increasing the heating time is good for obtaining the pure target product.

$$Al_3Nb + 2Nb_2Al + 5NbC = 5Nb_2AlC \text{ or } Nb_2Al + C = Nb_2AlC \quad (5.3)$$

Scanning electron microscope (SEM) was used to illustrate the morphology and microstructure of different samples. Figure 5.4 shows the morphology of NAC-8 (a and b) and NAC-9 (c and d). In Figure 5.4 a and b, the smooth and large bulk can be observed with the tiny impurities. In the Figure 5.4 c and d, the morphology of NAC-9 is very different with NAC-8, showing the clearer and smoother layer structure with many microspheres. The microsphere may be the impurities NbC according to the XRD patterns.

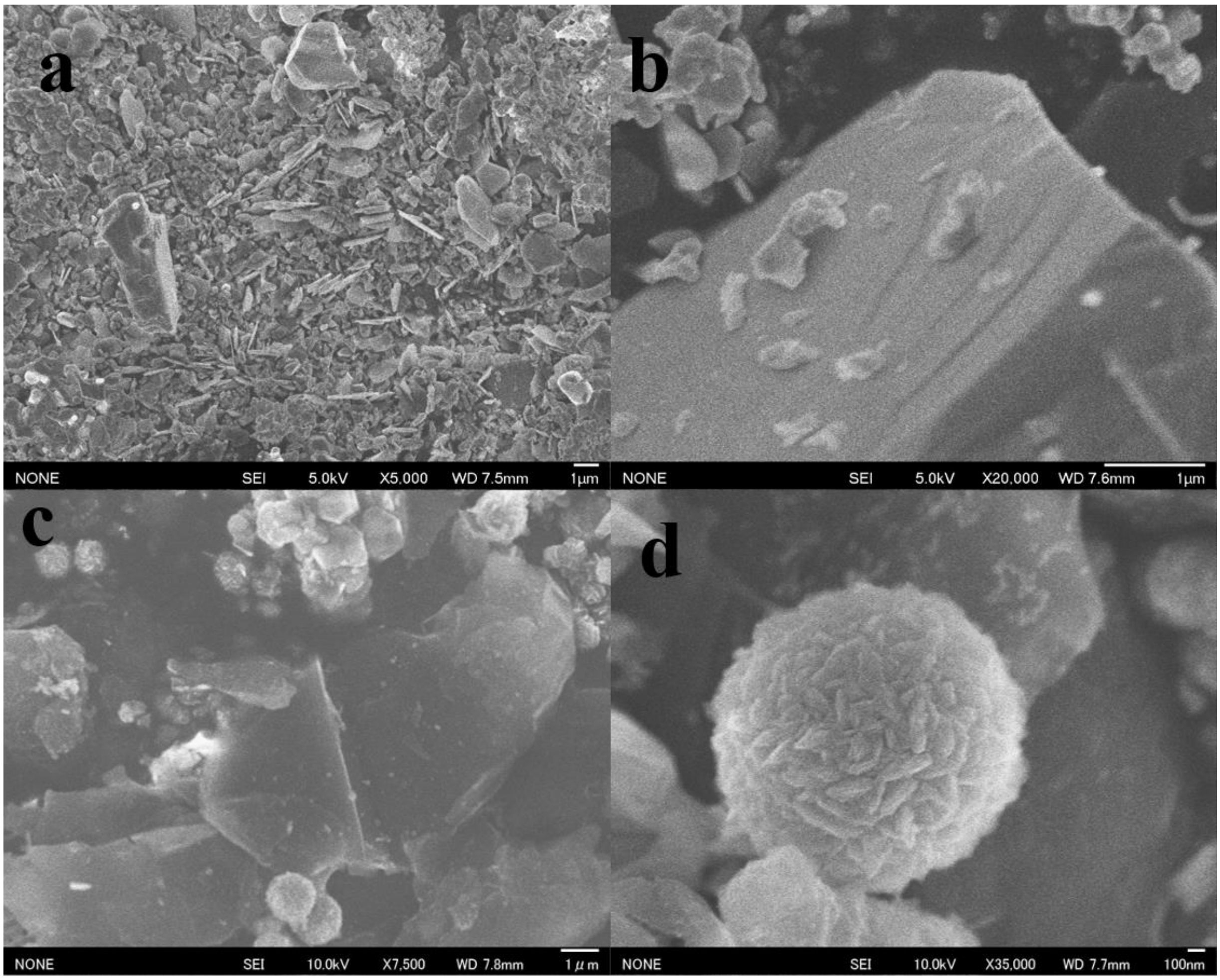

Figure 5.4 The SEM images of NAC-8 and NAC-9 with the different reaction time.

The last investigation is to explore the effect of the different amount of molten salt. In Figure 5.5, the big difference between the two samples indicates the diverse reaction process. It is obvious that NAC-10, NAC-11, and NAC-12 show stronger impurities peak than NAC-7, NAC-8, and NAC-9, indicating adsorption of more oxygen in the reaction. The intensity of the $NaNbO_3$ peaks is a volcano-like shape with the reaction time, indicating that prolong the reaction time is beneficial to decrease impurities due to the carbonization. In Figure 5.4a, NAC-10 shows none peaks of Al_3Nb, but very strong peaks of Nb_2Al, indicating that arise the amount of flux may be good for the reaction. However, the trace of Nb_2AlC can be detected by the XRD at this moment, showing the weak effect on the reaction. The peaks of Nb_2AlC are getting stronger with the increasing time, indicating the increased target product (NAC-8 and NAC-11). Figure 5.4c is the comparison of the sample of NAC-9 and NAC-12, they show the similar XRD pattern except for the different intensity of impurities, confirming that increasing the molten salt has the weak effect on the reaction.

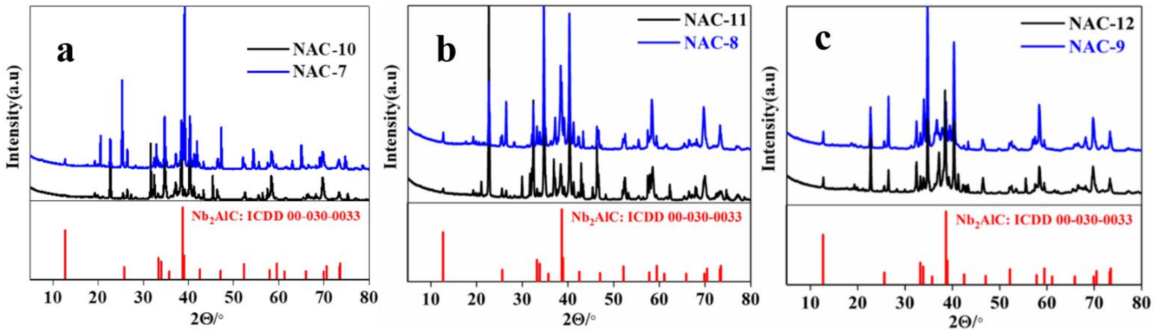

Figure 5.5 The comparison of samples with the different amount molten salts at the same reaction time.

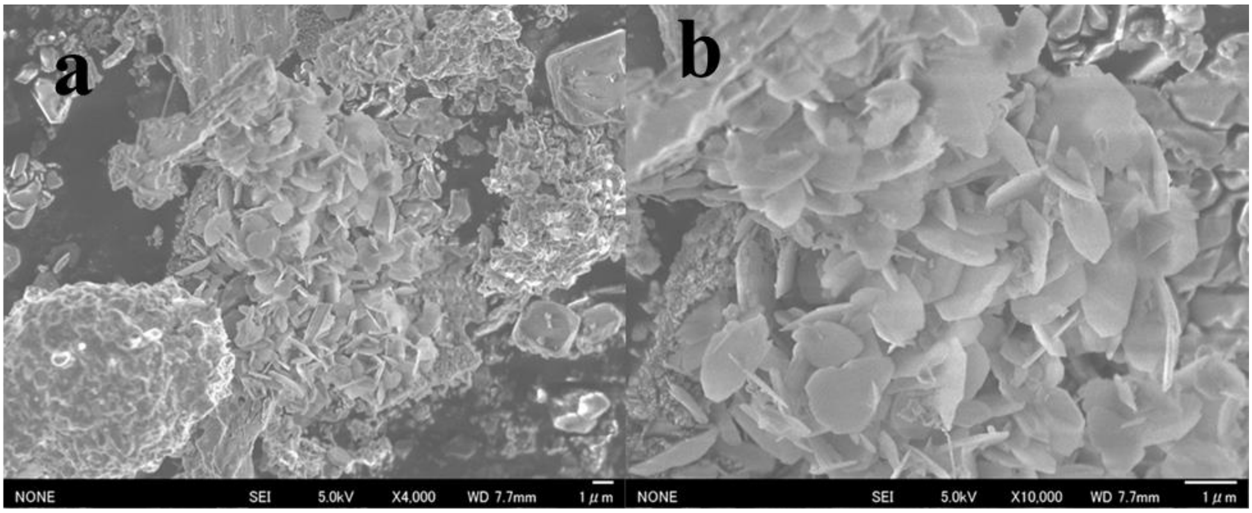

Figure 5.6 The SEM images of the sample NAC-10 at the different magnification.

Figure 5.6 is the morphology of the NAC-10 sample, showing that the large bulk and microplates coexist in the sample. The irregular and thin flakes intersperse and accumulate with each other to form a cluster, which is the intermediate product Nb_2Al. Figure 5.7 shows the different morphology of the NAC-11 sample. At low magnification, bulk and flake coexist in the sample. The standard hexagon and thin flakes intersperse in all the vision, and partial flakes accumulate with each other to form layer structure dispersed in the vision, suggesting the layer structure is formed. The morphology of the NAC-12 sample shows in Figure 5.8, a large and obvious layer structure bulk can be observed with the dispersed deformed hexagon flakes in the vision at low magnification, indicating that the Nb_2AlC is synthesized. The layer bulk shows the clear gap about the decade's nanometer with the thickness only nanometers, which is beneficial for deeper investigation.

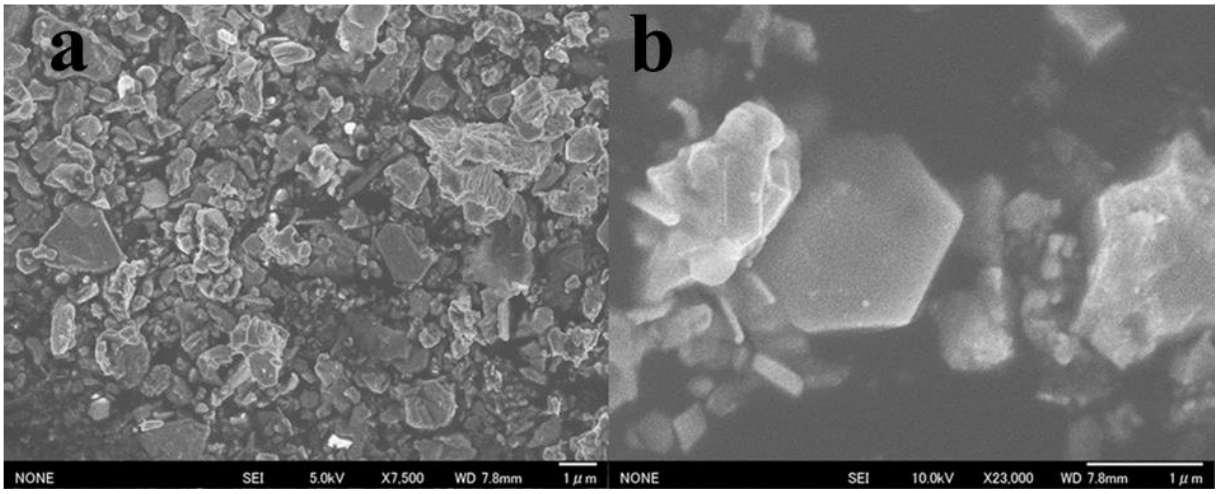

Figure 5.7 The SEM images of the sample NAC-11 at the different magnification.

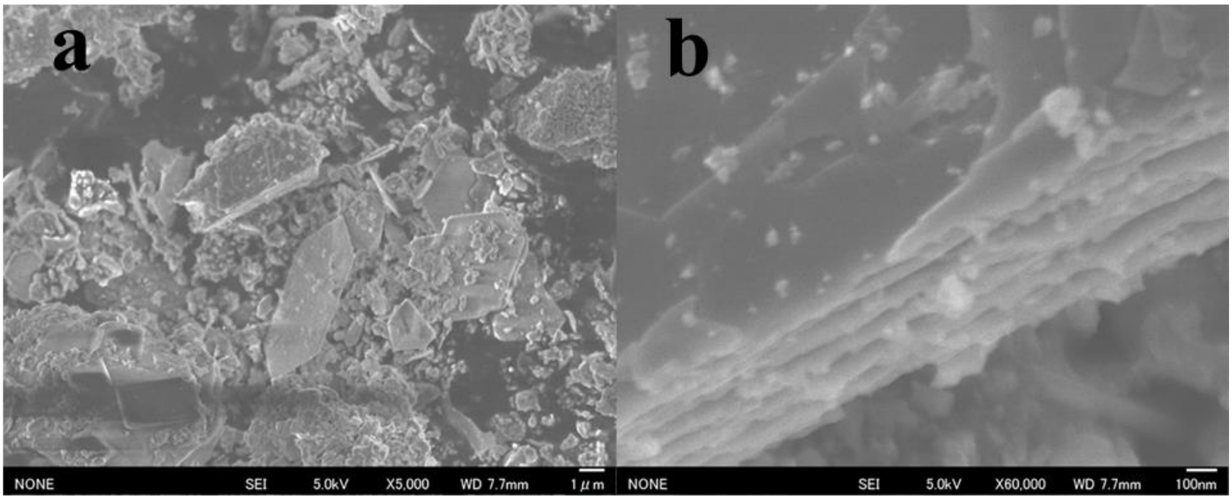

Figure 5.8 The SEM images of the sample NAC-12 at the different magnification.

As previously discussed, we choose NaCl as the flux to decrease the synthesized temperature of Nb_2AlC. In the investigation, we founded the reaction process of Nb_2AlC, indicating that synthesis Nb_2AlC at low temperature is feasible. In the experiment, we explored the effect of reaction time and the amount of flux. The reaction time is the key factor, and increasing reaction time is beneficial to obtain the pure product. The different amount of flux would improve the reaction with less time, but lead to the more impurities. In order to further investigation, we choose two best samples to etch to explore their electrocatalytic activity. Considering the reaction time and the amount of flux, NAC-12 and NAC-9 are the representatives to take more measurements.

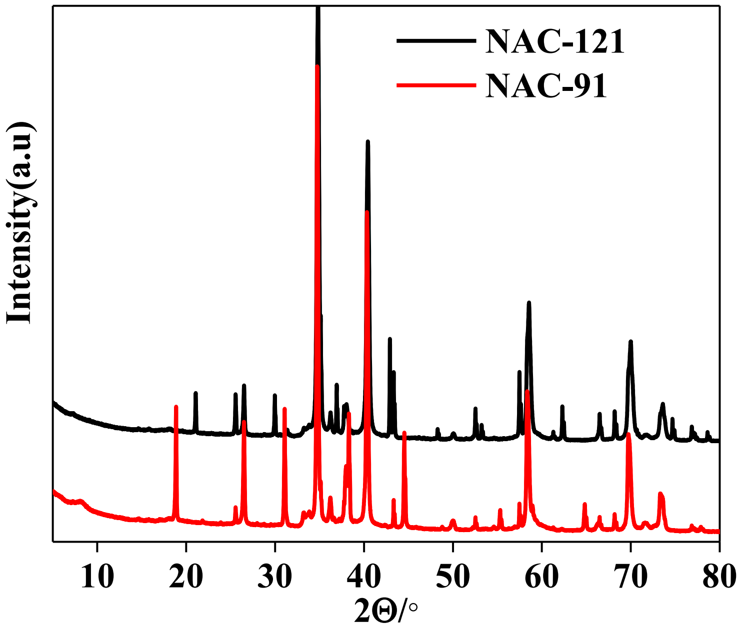

Figure 5.9 The comparison of the samples NAC-91 and NAC-121 after etching from NAC-9 and NAC-12 by the HF solution.

In Figure 5.9, NAC-91 shows a more obvious and broader layer peak about at 8°, indicating that the layer structure is synthesized [10, 28]. As we know, Nb_2Al and Al_3Nb are the intermediate products in the solid-state reaction, and Nb_2Al is produced in the late reaction, so they can be acted as the instruction in the reaction. In Figure 5.9, NAC-91 only shows the peaks of Nb_2Al, indicating NAC-91 reacted deeper than NAC-121. More interestingly, NAC-91 shows fewer impurities than NAC-121. They show the completely different impurities, proving that the different amount of flux leads to arising the diverse impurities. It should be noted that the two samples show fewer impurities, except for the NbC and Nb_2Al or Al_3Nb than the original materials (NAC-12 and NAC-9) because of the HF washing.

The XRD pattern is corresponding to the morphology, SEM was used to obtain the morphology and microstructure of samples. In the XRD, we previously showed that the MXene Nb_2C is obtained, as evidenced herein in Figure 5.10. The compact restacking of MXene flakes can be observed in the vision, showing the multilayered counterparts structure. Figure 5.10 a and b are the NAC-121, showing the smaller layer gap than NAC-91 (Figure 5.10 c and d), indicating NAC-91 is beneficial for electrons transfer.

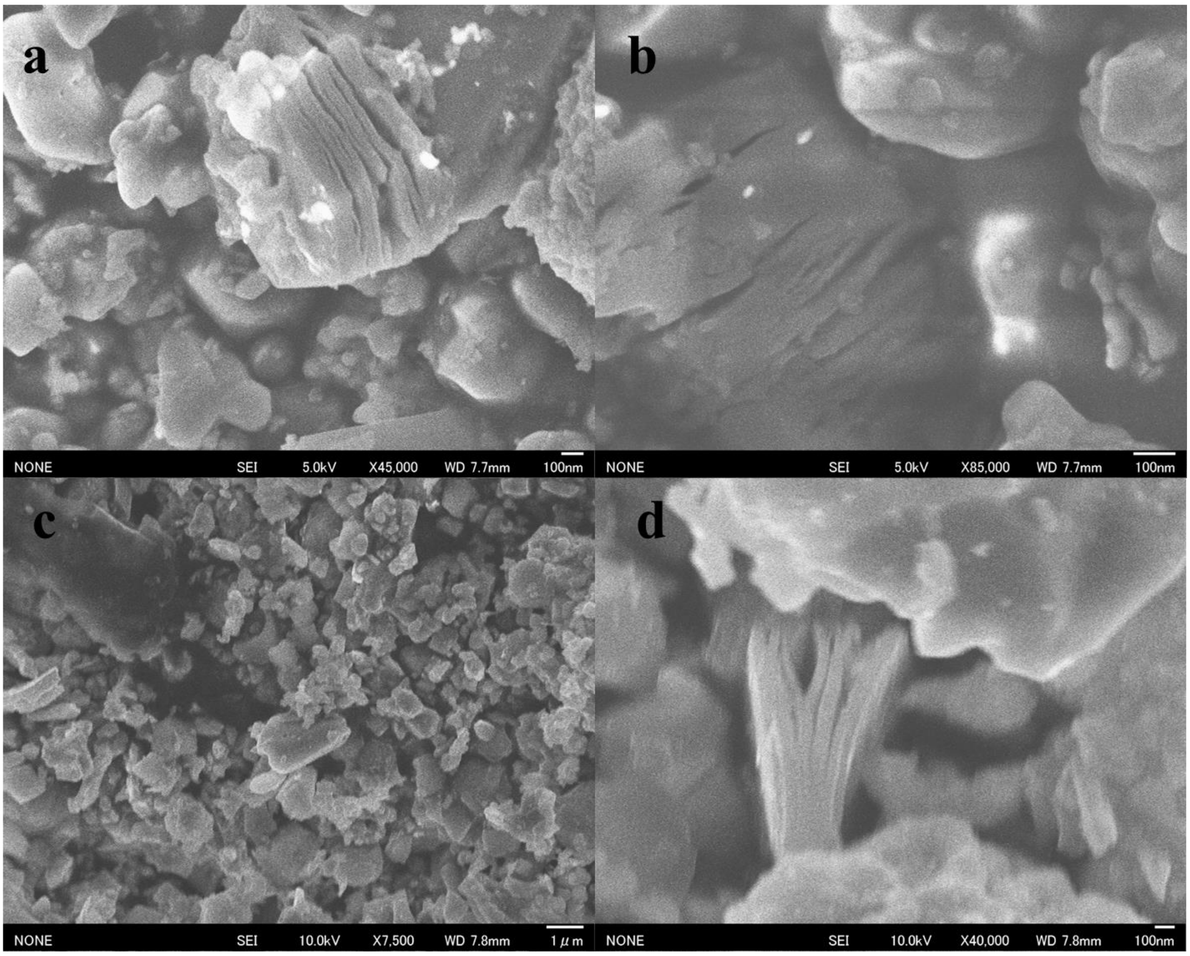

Figure 5.10 The SEM images of the sample NAC-121(a and b) and NAC-91 (c and d) at the different magnification.

5.3.2 EDS results

The types of element and their stoichiometric ratios were determined by energy dispersive X-ray spectrometry (EDS, Genesis XM2). Figure 5.11 is the full pattern of different elements, the analysis of the sample revealed that C, Al, and Nb are the significant elements, the ratio analysis shows that they are not stoichiometric ratio with Nb_2AlC, due to the acid washing and the impurities (inset of Figure 5. 11). As previously discussed, the NAC-91 shows the larger layer gap, acting as the sample to loading Pt nanoparticles. It is clear that the trace of Pt signal was detected, which is about 4 wt. % less than the starting materials. However, the EDS proved that the Pt-loading on NAC-91 sample is synthesized.

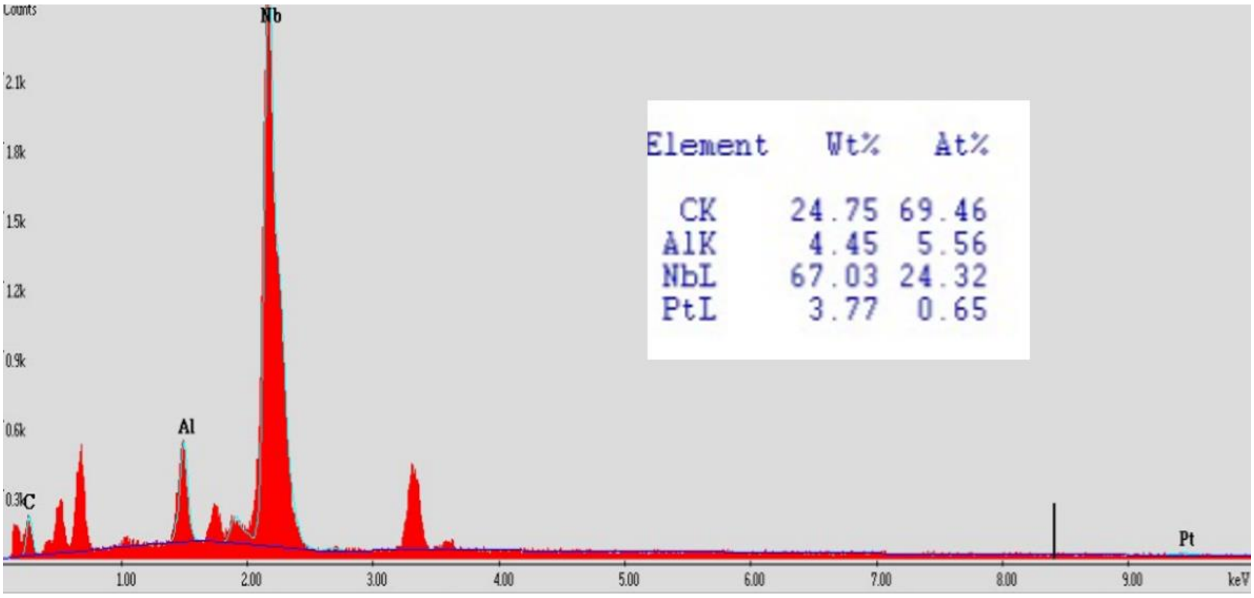

Element	Wt%	At%
CK	24.75	69.46
AlK	4.45	5.56
NbL	67.03	24.32
PtL	3.77	0.65

Figure 5.11 The EDS analysis of NAC-91 catalyst prepared after Pt-loading, and the detail ratio of the different elements is in the inset.

5.3.3 XPS results

The surface states of the NAC-91/Pt sample for different elements were detected by XPS. In the survey region, the signals from elements C, Nb, O, F, and Pt were obviously detected. Interestingly, Na signal was observed at around 1070 eV, maybe due to that partial Na ions inset into the layer at the high temperature. The Al signals mostly come from the intermediate products Nb_2Al or Al_3Nb. In the survey region, several unusual peaks come out, such as Nb 3p, Pt 4d, and Nb 4p. We choose the Pt 4f, Nb 3d, and C 1s as the represents for high-resolution due to accurate analysis. The high-resolution double C 1s peak can be further split into three synthetic peaks: 284.4 eV (C-C/C-H), 281.7 eV (C-Nb), and 282.2 eV (C-Nb-O), corresponding to the different source [29, 30]. It is known that C-C or C-H comes from the element carbon. The main compositions of C-Nb and C-Nb-O indicate the main NbC phase, and the different ratios of the two bonds proved the completely etching of Nb_2AlC. Tri-peaks are in the Nb high-resolution pattern, the lower bind energy around at 201 eV is the elemental Nb $3d_{5/2}$. The remaining two peaks can be split into four double peaks belonging to the different composites, which is a doublet with a 2.6 eV split into Nb $3d_{5/2}$ and Nb $3d_{3/2}$. There are no obvious split peaks of Nb_2O_5, indicating a few phases in the sample. The components centered at 204.6, 204.9, and 204.4 eV were assigned as the Nb $3d_{5/2}$ of NbC, C-Nb-O/F, and NbO_x, respectively [31, 32].

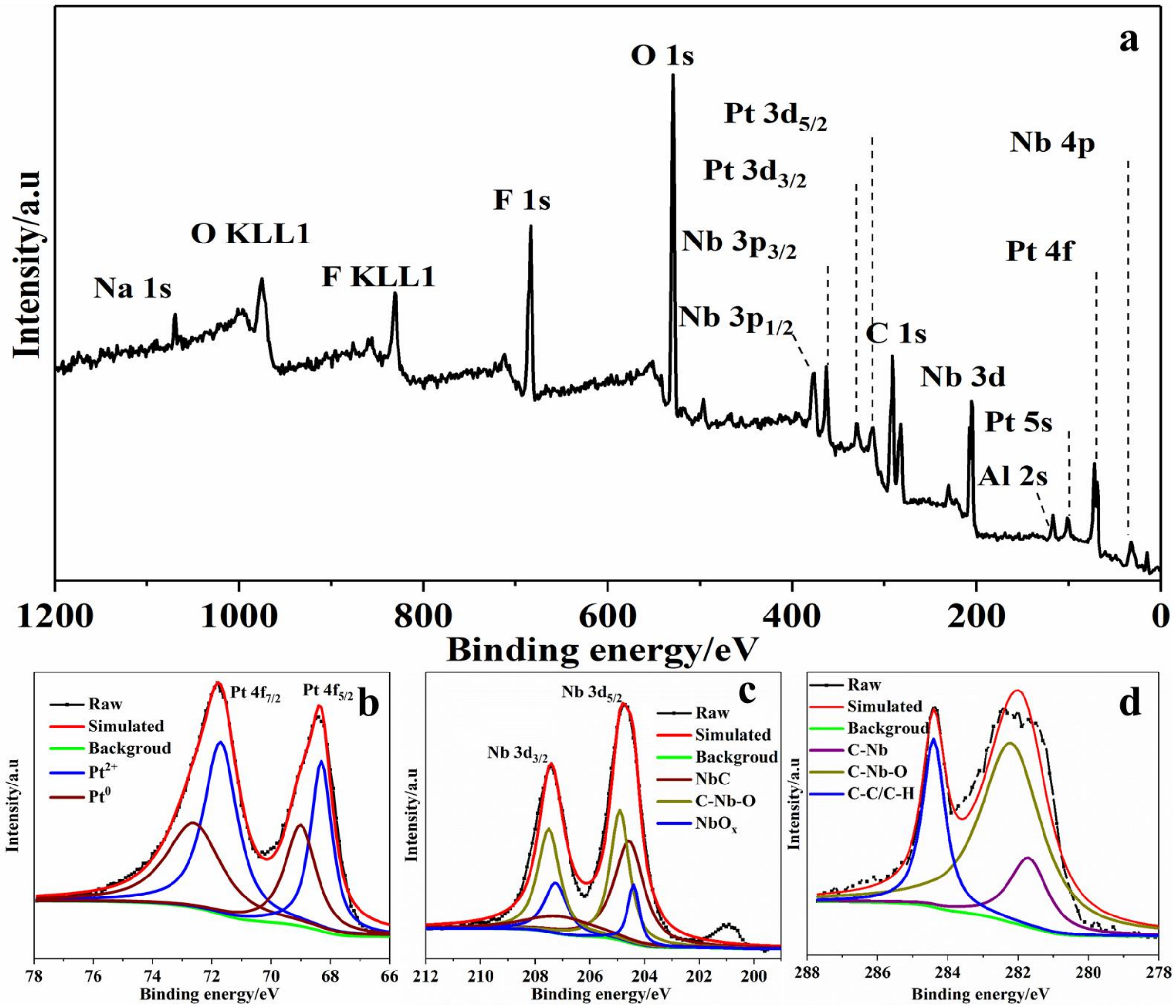

Figure 5.12 The full XPS survey of the sample of NAC-91/Pt (a). The different elements region: Pt 4f (b), Nb 3d (c), and C 1s (d).

At last, the high-resolution double Pt 4f peak showed in Figure 5.12b. The high-resolution Pt 4f has two peaks 4f7/2 and 4f5/2. The two peaks can be further split into four peaks 68.3, 71.7 and 69, 72.4 eV, corresponding to the different oxide states of platinum: Pt^0 and Pt^{2+} species. However, it should be noted that the binding energy of Pt 4f is lower than the normal due to the complicated conditions [33, 34]. As we know, Al atoms would be removed by the etching, and the Nb layer would adsorb the active groups, such as the O^{2-}, F^- or OH^-, due to lack of electrons. The Pt-loading changes the balanced conditions, and the reduced Pt atoms capture electrons and fix at the Nb layer to enhance the ORR catalytic activity.

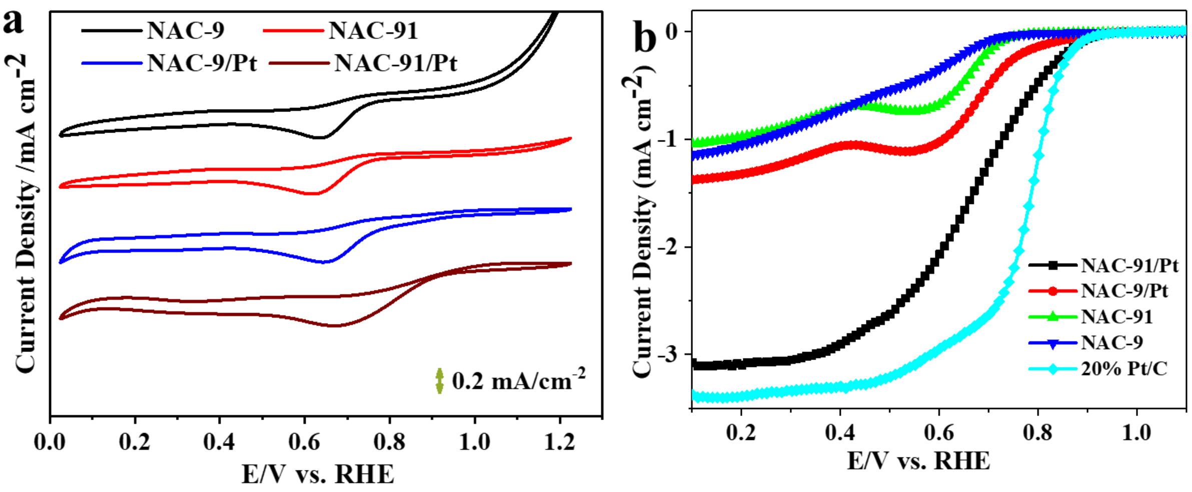

Figure 5.13 The CV curves of NAC samples in O_2 saturated 0.1 M KOH media with a scan rate of 50 mV s^{-1} (a). The LSV curves of NAC samples and 20% Pt/C at 1600 rpm in O_2 saturated electrolyte (b).

5.3.4 Electrochemistry results and discussion

The ORR catalytic activity of the catalysts NAC-9, NAC-91, NAC-9/Pt, and NAC-91/Pt in the alkaline medium is shown in Figure 5.13a. The cyclic voltammetry (CV) measurement is in the O_2-saturated 0.1 M KOH with the scan rate of 50 mV/s. It is clear that all the samples show the obviously reduced peak around at 0.7 V *vs*. RHE, indicating they are the potential ORR catalysts. NAC-9 shows a tilt up in the high onset-potential, due to the excellent adsorption and desorption ability. More importantly, the CV curves of all samples show a sink than usual in the low potential, resulting from too many oxides. NAC-91/Pt shows a higher positive but broader peak than the other two samples, indicating the potential catalytic activity. Linear sweep voltammetry (LSV) was used to illustrate the catalytic properties of NAC-9, NAC-91, NAC-9/Pt, and NAC-91/Pt catalysts with commercial Pt/C. The LSV curves show that etching is good for improving the ORR process, because of the increased surface area and active sites. However, they show lower activity than Pt-loading samples. In detail, Pt-loading samples show a significant improvement for ORR activity compared to the original samples. Figure 5.13b shows that NAC-91/Pt sample has the more positive inflection point in the low current density. The highest onset-potential of 0.84 V *vs*. RHE and the highest limited current density than other samples, indicating the excellent electrochemical performance. The onset-potential is only 10 mV negative shift than the commercial Pt/C, showing the promising catalytic activity.

The kinetics of the catalysts NAC-91/Pt was performed by the Koutecky–Levich (K–L) analysis, which comes from the LSV curves at different rotation speeds with the scan rate of 10 mV/s. From Figure 5.14a, the electron transfer number of NAC-91/Pt sample is from 3.56 to 3.87 at the potential range of 0.1-0.5 V, suggesting the ORR process of NAC-91/Pt is the four-electron pathway. The superior catalytic activity and stability are essential for one excellent catalyst. The chronoamperometry measurements for the sample of NAC-91/Pt is in 0.1 M KOH solution for 30,000 seconds with the rotation speed of 300 rpm to explore their stability, as shown in Figure 5.14b. After scanning, only 3% attenuation for NAC-91/Pt compared to 50% for the commercial Pt/C under the same condition, indicating the higher stability.

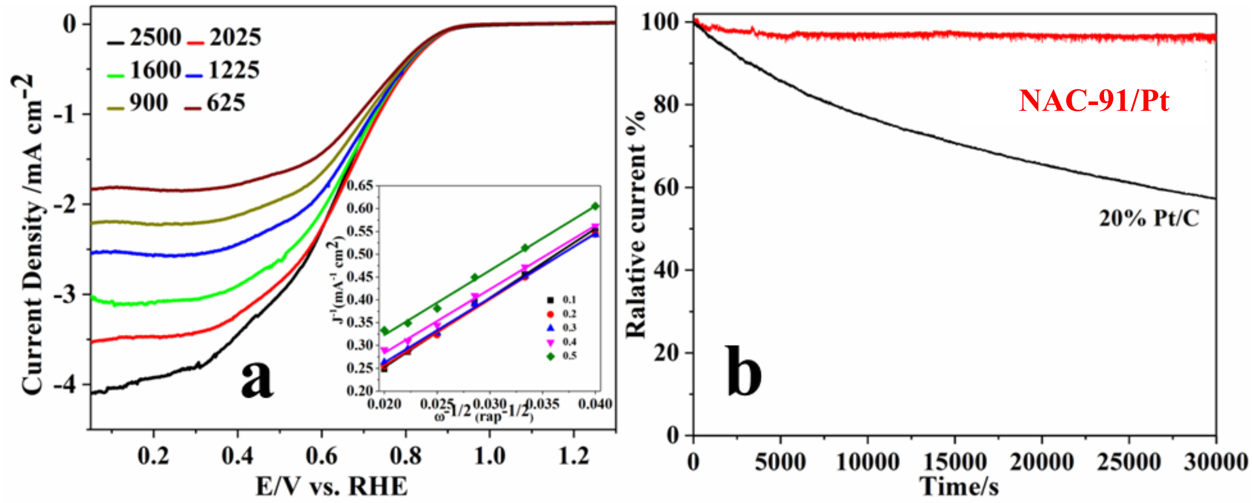

Figure 5.14 LSV curves of the NAC-91/Pt sample at different rotation speeds and the K-L plots for the NAC-91/Pt sample at different potentials (a). The electrochemical stability of the NAC-91/Pt sample accessed by chronoamperometric curves in O_2-saturated at a rotation speed of 300 rpm for 30000s (b).

Further exploring the kinetic process of the catalysts, the Tafel slope was introduced. As we know, the standard Tafel slope is close to 60 mV per decade for the effective reaction. In fact, the measurements of platinum are different from the theoretical value, due to the condition and measurement error. In this chapter, we find the Tafel slope of NAC-91/Pt is 78 mV per decade, close to the 70 mV per decade of Pt/C catalyst (Figure 15a).

As we know, the low resistance value has advantages to improve the reaction, suggesting the excellent electron transfer ability [35, 36]. The electronic impedance spectroscopy (EIS) was used to calculate the surface resistance in the electrochemical reaction. It is known that lower resistance is beneficial to electron transfer. Figure 5.15b is the EIS spectra of NAC-91/Pt, and the schematic illustration for the equivalent circuit is shown in the inset of Figure 5.15b. R_S is the Pt-loading support or electrolyte resistance ca. 22 ohms. R_1 represents the surface resistance in the electrochemical reaction ca. 65 ohms for NAC-91/Pt, suggesting the excellent conductivity.

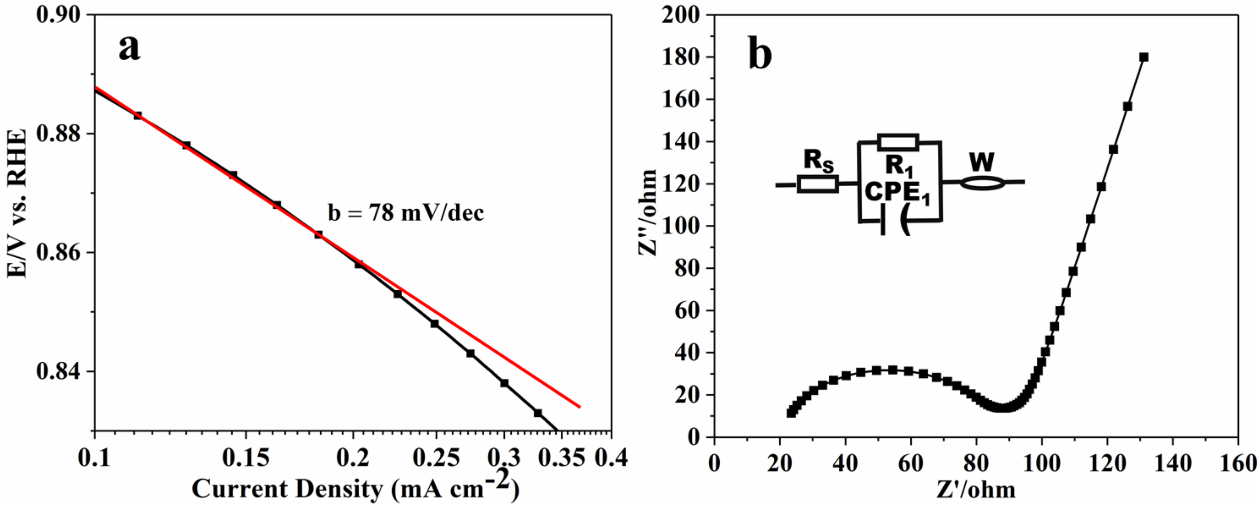

Figure 5.15 The corresponding Tafel plots from LSV curves at 1600 rpm of the NAC-91/Pt sample (a); The impedance spectra of three samples at open circles potential, and the line is the fitting results (b). The entire tests are in the 0.1 M KOH media.

All the electrochemical measurements show that NAC-91/Pt has the excellent catalytic activity. We believe that the layer structure, low resistance, and the effective ORR process are beneficial to promoting oxygen reduction reaction.

5.4 Conclusions

In this chapter, we successfully decreased the synthesized temperature of the MAX Nb_2AlC from 1600°C to 1000°C by the molten salt assisted solid-state reaction. We studied the effect of the flux type, the flux amount, the reaction temperature, and the heating time on the crystal phase and morphology of the obtained materials. Moreover, we put forward the reaction mechanism, showing that the flux has a great effect on the second reaction step - the process of $NbAl_2$. We also point out that much more flux may improve the reaction process, but leading to more impurities. Then, two samples as the representatives were etched by the HF solution to obtain the multilayer material 2D MXene Nb_2C. Finally, the ORR catalytic activity of the four samples of Pt-loading or not of before and after HF etching was compared. NAC-91/Pt shows the highest ORR catalytic activity, which is only 10 mV negative shift than the commercial Pt/C catalyst. The electrochemical performance indicates that 2D MXene Nb_2C is an excellent support to promote the ORR process, and shows the higher electrochemical stability than the traditional carbon materials.

5.5 References

[1] Lei, J.-C.; Zhang, X.; Zhou, Z. Recent advances in MXene: Preparation, properties, and applications. *Frontiers of Physics* **2015,** *10* (3), 276-286.

[2] Magne, D.; Mauchamp, V.; Celerier, S.; Chartier, P.; Cabioc'h, T. Site-projected electronic structure of two-dimensional Ti3C2 MXene: the role of the surface functionalization groups. *Physical chemistry chemical physics* **2016,** *18* (45), 30946-30953.

[3] Zhu, J.; Ha, E.; Zhao, G.; Zhou, Y.; Huang, D.; Yue, G.; Hu, L.; Sun, N.; Wang, Y.; Lee, L. Y. S.; Xu, C.; Wong, K.-Y.; Astruc, D.; Zhao, P. Recent advance in MXenes: A promising 2D material for catalysis, sensor and chemical adsorption. *Coordination Chemistry Reviews* **2017,** *352*, 306-327.

[4] Ng, V. M. H.; Huang, H.; Zhou, K.; Lee, P. S.; Que, W.; Xu, J. Z.; Kong, L. B. Recent progress in layered transition metal carbides and/or nitrides (MXenes) and their composites: synthesis and applications. *Journal of Materials Chemistry A* **2017,** *5* (7), 3039-3068.

[5] Anasori, B.; Lukatskaya, M. R.; Gogotsi, Y. 2D metal carbides and nitrides (MXenes) for energy storage. *Nature Reviews Materials* **2017,** *2* (2), 16098.

[6] Ghidiu, M.; Halim, J.; Kota, S.; Bish, D.; Gogotsi, Y.; Barsoum, M. W. Ion-exchange and cation solvation reactions in Ti_3C_2 MXene. *Chemistry of Materials* **2016,** *28* (10), 3507-3514.

[7] Soundiraraju, B.; George, B. K. Two-dimensional titanium nitride (Ti_2N) MXene: synthesis, characterization, and potential application as surface-enhanced Raman scattering substrate. *ACS Nano* **2017,** *11* (9), 8892-8900.

[8] Li, J.; Yuan, X.; Lin, C.; Yang, Y.; Xu, L.; Du, X.; Xie, J.; Lin, J.; Sun, J. Achieving high pseudocapacitance of 2D titanium carbide (MXene) by cation intercalation and surface modification. *Advanced Energy Materials* **2017,** *7* (15), 1602725.

[9] Feng, A.; Yu, Y.; Jiang, F.; Wang, Y.; Mi, L.; Yu, Y.; Song, L. Fabrication and thermal stability of NH_4HF_2-etched Ti_3C_2 MXene. *Ceramics International* **2017,** *43*(8), 6322-6328.

[10] Mashtalir, O.; Lukatskaya, M. R.; Zhao, M. Q.; Barsoum, M. W.; Gogotsi, Y. Amine-assisted delamination of Nb_2C MXene for Li-ion energy storage devices. *Advanced Materials* **2015,** *27* (23), 3501-3506.

[11] Shao, M.; Chang, Q.; Dodelet, J. P.; Chenitz, R. Recent advances in electrocatalysts for oxygen reduction reaction. *Chemical Reviews* **2016,** *116* (6), 3594-3657.

[12] Nie, Y.; Li, L.; Wei, Z. Recent advancements in Pt and Pt-free catalysts for oxygen reduction reaction. *Chemical Society Reviews* **2015,** *44* (8), 2168-2201.

[13] Zhang, W.; Lai, W.; Cao, R. Energy-related small molecule activation reactions: oxygen reduction and hydrogen and oxygen evolution reactions catalyzed by porphyrin- and corrole-based systems. *Chemical Reviews* **2017,** *117* (4), 3717-3797.

[14] Zhang, C.; Shen, X.; Pan, Y.; Peng, Z. A review of Pt-based electrocatalysts for oxygen reduction reaction. *Frontiers in Energy* **2017,** *11* (3), 268-285.

[15] Navalon, S.; Dhakshinamoorthy, A.; Alvaro, M.; Antonietti, M.; Garcia, H. Active sites on graphene-based materials as metal-free catalysts. *Chemical Society Reviews* **2017,** *46* (15), 4501-4529.

[16] Jana, P. P.; Lidin, S. Structural impact of platinum on the incommensurably modulated gamma-brass related composite structure $Pd_{15}Zn_{54}$. *Inorganic Chemistry* **2012,** *51* (18), 9893-9901.

[17] Kuroki, H.; Tamaki, T.; Matsumoto, M.; Arao, M.; Kubobuchi, K.; Imai, H.; Yamaguchi, T. Platinum–iron–nickel trimetallic catalyst with superlattice structure for enhanced oxygen reduction activity and durability. *Industrial & Engineering Chemistry Research* **2016,** *55* (44), 11458-11466.

[18] Sahin, N. E.; Napporn, T. W.; Dubau, L.; Kadirgan, F.; Léger, J.-M.; Kokoh, K. B. Temperature-dependence of oxygen reduction activity on Pt/C and PtCr/C electrocatalysts synthesized from microwave-heated diethylene glycol method. *Applied Catalysis B: Environmental* **2017**, *203*, 72-84.

[19] Zhang, Y.; Chen, T.; Alia, S.; Pivovar, B. S.; Xu, W. Single-molecule nanocatalysis shows in situ deactivation of Pt/C electrocatalysts during the hydrogen-oxidation reaction. *Angewandte Chemie* **2016,** *55* (9), 3086-3090.

[20] Xie, X.; Chen, S.; Ding, W.; Nie, Y.; Wei, Z. An extraordinarily stable catalyst: Pt NPs supported on two-dimensional Ti3C2X2 (X = OH, F) nanosheets for oxygen reduction reaction. *Chemical Communications* **2013,** *49* (86), 10112-10114.

[21] Fang, B.; Kim, J. H.; Kim, M.; Yu, J.-S. Ordered hierarchical nanostructured carbon as a highly efficient cathode catalyst support in proton exchange membrane fuel cell. *Chemistry of Materials* **2009,** *21* (5), 789-796.

[22] Xue, Q.; Pei, Z.; Huang, Y.; Zhu, M.; Tang, Z.; Li, H.; Huang, Y.; Li, N.; Zhang, H.; Zhi, C. Mn 3 O 4 nanoparticles on layer-structured Ti_3C_2 MXene towards the oxygen reduction reaction and zinc–air batteries. *Journal of Materials Chemistry A* **2017,** *5* (39), 20818-20823.

[23] Šljukić, B.; Martins, M.; Kayhan, E.; Balčiūnaitė, A.; Şener, T.; Sequeira, C. A. C.; Santos, D. M. F. SnO_2 -C supported PdNi nanoparticles for oxygen reduction and borohydride oxidation. *Journal of Electroanalytical Chemistry* **2017,** *797*, 23-30.

[24] Senevirathne, K.; Hui, R.; Campbell, S.; Ye, S.; Zhang, J. Electrocatalytic activity and durability of Pt/NbO2 and Pt/Ti_4O_7 nanofibers for PEM fuel cell oxygen reduction reaction. *Electrochimica Acta* **2012,** *59*, 538-547.

[25] Zhang, W.; Travitzky, N.; Hu, C.; Zhou, Y.; Greil, P. Reactive hot pressing and properties of Nb_2AlC. *Journal of the American Ceramic Society* **2009,** *92* (10), 2396-2399.

[26] Li, Y.; Qian, Y.; Zhao, G.; Xu, J.; Li, M. Preparation of Nb_2AlC coating by DC magnetron sputtering and subsequent annealing. *Ceramics International* **2017,** *43* (8), 6622-6625.

[27] Schawe, J. E.; Pötschke, P.; Alig, I. Nucleation efficiency of fillers in polymer crystallization studied by fast scanning calorimetry: Carbon nanotubes in polypropylene. *Polymer* **2017,** *116*, 160-172.

[28] Lin, H.; Gao, S.; Dai, C.; Chen, Y.; Shi, J. A two-dimensional biodegradable niobium carbide (MXene) for photothermal tumor eradication in NIR-I and NIR-II biowindows. *Journal of the American Chemical Society* **2017,** *139* (45), 16235-16247.

[29] Braic, M.; Braic, V.; Balaceanu, M.; Vladescu, A.; Zoita, C.; Titorencu, I.; Jinga, V.; Miculescu, F. Preparation and characterization of biocompatible Nb–C coatings. *Thin Solid Films* **2011,** *519* (12), 4064-4068.

[30] Zhu, X.; Liu, B.; Hou, H.; Huang, Z.; Zeinu, K. M.; Huang, L.; Yuan, X.; Guo, D.; Hu, J.; Yang, J. Alkaline intercalation of Ti_3C_2 MXene for simultaneous electrochemical detection of Cd (II), Pb (II), Cu (II) and Hg (II). *Electrochimica Acta* **2017,** *248*, 46-57.

[31] Marques, M.; Ferraria, A.; Correia, J.; Do Rego, A. B.; Vilar, R. XRD, XPS and SEM characterisation of Cu–NbC nanocomposite produced by mechanical alloying. *Materials Chemistry and Physics* **2008,** *109* (1), 174-180.

[32] Bendavid, A.; Martin, P.; Kinder, T.; Preston, E. The deposition of NbN and NbC thin films by filtered vacuum cathodic arc deposition. *Surface and Coatings Technology* **2003,** *163*, 347-352.

[33] Liu, C.; Xian, H.; Jiang, Z.; Wang, L.; Zhang, J.; Zheng, L.; Tan, Y.; Li, X. Insight into the improvement effect of the Ce doping into the SnO2 catalyst for the catalytic combustion of methane. *Applied Catalysis B: Environmental* **2015,** *176*, 542-552.

[34] Igarashi, H.; Fujino, T.; Zhu, Y.; Uchida, H.; Watanabe, M. CO tolerance of Pt alloy electrocatalysts for polymer electrolyte fuel cells and the detoxification mechanism. *Physical Chemistry Chemical Physics* **2001,** *3* (3), 306-314.

[35] Zhang, Y.; Wang, Q.; Li, J.; Wang, X.; Liu, K.; Feng, H.; Jiang, J.; Li, J.; Qian, D. Facile fabrication of sandwich-structured Co_3O_4/N-rGO/AB hybrid with enhanced ORR electrocatalytic

performances for metal–air batteries. *RSC Advances* **2015,** *5* (12), 9057-9063.

[36] L. Li, P. D., X. Gu, Y. Wang, L. Yan and X. Zhao. Metal–organic framework derived carbon combined with ishigh degree of graphitization. *Journal of Materials Chemistry A* **2017,** *5*, 789-795.

General conclusions

This thesis focused on the development of oxygen reduction reaction (ORR) catalysts for the proton exchange membrane fuel cells (PEMFCs).

In chapter 1, we introduced the recent progress in the field of research for the ultra-low Pt-loading amount catalyst of ORR. In addition, the Pt-free electrochemical catalysts of ORR were also introduced. Although the development of ORR catalyst is rapid, several issues still need to be overcome, such as the low conversion efficiency, the poor stability, and the corrosion of the support material. Facing these challenges, we developed 3 kinds of nanostructured materials as catalysts or supports to promote the ORR process.

In chapter 2, we briefly summarized the equipment and the reagents used in the experiments. In addition, the principles of the electrochemical tests were introduced relating to the cyclic voltammetry (CV), the linear sweep voltammetry (LSV), and the electronic impedance spectroscopy (EIS).

In chapter 3, we synthesized a serial of Pt-based alloys PtM (M: Fe, Co, Ni) used as the ORR catalyst by a simple method. The method significantly decreased the Pt-loading amount. The physical characterizations demonstrate that the PtFe alloy has well-defined, homogeneous, and ultra-small particle size morphology. Finally, the PtM (M: Fe, Co, Ni) alloys were used as the ORR catalysts. Among them, the PtFe alloy exhibits the best activity and superior electrochemical stability both in the acidic as well as the alkaline media. Therefore, the PtFe alloy catalyst shows a great potential to replace the commercial Pt/C catalyst for ORR.

In chapter 4, we designed and prepared 3 kinds of Fe, Co incorporated in P-doped porous carbon materials using a metal-organic framework (MOF) as the precursor. The Pt-free materials were synthesized by *in-situ* carbonization method at 800, 900 and 1000°C. In this chapter, we found that the suitable carbonization temperature is 900°C and the ratio of dual transition metals is 3:1. In the electrochemical measurements, FCPA-900 shows the best ORR catalytic activities because of the higher specific surface area, the synergistic effect, and the better-defined amorphous carbon structure.

In chapter 5, we synthesized a new 2-D MXene material Nb_2C as the catalyst support, using solid-state reaction by the molten salt as flux. Moreover, the synthesis temperature of

Nb_2AlC was successfully decreased from 1600 to 1000°C. We investigated the reaction parameters to obtain Nb_2AlC with the simplest synthesis conditions, such as the effect of the molten salt, the heating temperature, the reaction time, and the amount of flux. In addition, we found that more flux amount can improve the reaction process, but can introduce more impurities. Then, the multilayer 2-D MXene Nb_2C was obtained by etching the Nb_2AlC with the HF solution. Finally, we compared the ORR catalytic activities of the 4 samples with and without Pt-loading, and before and after HF etching. The multilayer 2-D MXene Nb_2C with Pt-loading shows a comparable catalytic activity with the commercial Pt/C catalyst. All the electrochemical measurements show that the 2-D MXene Nb_2C displays an excellent stability compared with the conventional carbon support.

Future Prospects

Developing highly efficient Pt or Pt-free catalysts for the oxygen reduction reaction (ORR) is key to the proton exchange membrane fuel cells (PEMFCs). Our work developed several kinds of ORR catalysts and support materials to promote the ORR process. However, the more effective catalysts and the more stable supports need to be prepared to improve the ORR catalytic activity.

The future prospects of ORR catalyst should focus on the following parts: the low Pt-loading amount, the new Pt-free catalyst, the high stability, and the high conversion efficiency. The current research showed that the catalytic activities of Pt-based catalysts are greatly affected by the alloying method, the exposed surface, the particle size, and the morphology. The alloying method and the exposed surface influence the aggregation of the active sites. The suitable size and morphology are beneficial to improve the corrosion resistance. Therefore, the optimizations of the Pt-based catalysts can improve their catalytic performance. However, the high price of Pt seriously hindered the application of the Pt-based catalysts. Several kinds of Pt-free catalysts were developed, showing the high electrocatalytic activities. However, they cannot meet the demand for commercialization, such as the stability and the activity. Consequently, it is vital to develop the new, cheap, stable, and efficient ORR catalysts to substitute the Pt-based catalysts. The stability of fuel cell relies on the stable ORR catalyst and the stable proton exchange membrane. Developing the stable catalyst and the proton exchange membrane is imperative to improve the stability of fuel cell. In addition, the investigation of developing the new and efficient ORR catalyst for PEMFCs will be a big challenge, especially for the Pt-free catalyst.

Finally, the ORR catalysts gained a great progress in the past decades, but they cannot meet the requirement of the application. Therefore, the exploration and improvement in the design and synthesis of the new ORR catalysts are still important for ORR and the catalytic reaction.

Achievements

Publications

1. **Nannan Wang**, Yanqiang Li, Zhanglin Guo, Huan Li, Shuzi Hayase, Tingli Ma, Minute quantities of hexagonal nanoplates PtFe alloy with facile operating conditions enhanced electrocatalytic activity and durability for oxygen reduction reaction, *Journal of Alloys and Compounds* **2018**, 752, 23–31.

2. **Nannan Wang**, Yanqiang Li, Zhanglin Guo, Huan Li, Shuzi Hayase, Tingli Ma, Synthesis of Fe, Co incorporated in P-doped porous carbon using a metal-organic framework (MOF) precursor as stable oxygen reduction reaction catalysts, *Journal of the Electrochemical Society*. **(Under review)**

3. **Nannan Wang**, Yanqiang Li, Zhanglin Guo, Huan Li, Shuzi Hayase, Tingli Ma, Synthesis of 2-D layer structured Nb2C by a novel molten salt assisted solid-state reaction method. (**In preparation**)

Conferences

Oral: Yanqiang Li, Haibing Xu, **Nannan Wang**, Tingli Ma, Facile Synthesis of N, S co-doped Porous Carbon from Dual-ligands Metal-Organic Frameworks for ORR, The spring meeting of Electrochemical Society in Japan, 2017.

Poster: **Nannan Wang**, Tingli Ma, Synergistic effect of Fe, Co, and phytic acid based metal-organic framework for oxygen reduction reaction, The Japan-China Joint Workshop on Nanomaterials and their Application in New Energy Devices, 2017

Acknowledgment

Firstly, I would like to express my deepest thanks to my supervisor Prof. Tingli Ma. She gave me an opportunity to pursue my Ph.D. degree in Japan. She always guides and encourages me in my life and my research. I believe I cannot have possible to solve the problems during the Ph.D. period without her devices and supports. I am impressed by her knowledgeable and creative characteristics. Prof. Ma provides the effective guidance in time no matter how busy she is when I face the difficulties in the experiment. Thanks again Prof. Ma for your kind guidance, encouragement, and support. In this chance, I would like my best wishes to Prof. Ma and Ma Lab.

Secondly, I would like to show my great thanks to Prof. Shuzi Hayase. I learned a lot from his class. More importantly, Thanks Prof. Hayase provides some instruments such as water purification, which facilitate my experiment. Thanks again Prof. Hayase for his help.

Thirdly, I would like to show my great thanks to Prof. Shyam S. Pandey. He is very kind and friendly. Thanks again Prof. Shyam S. Pandey for his help.

Fourthly, I would like to thank my tutor, Mrs. Zhihui Zhang, she gave me a lot of help and suggestions when I faced troubles. I would like to thank all the members of Ma Lab, they give me a lot encourages and helps. rateThanks them again for their help and encourages.

Finally, yet importantly, I would like to express my thanks to my family. Their support and encouragement always inspired me to fight for a better research work and a better life in the future. Finally, I also expressed my gratitude to the persons who once contributed to this thesis, I feel sorry but I could not show my thanks to them one by one.